Development and characterization of electron sources for diffraction applications

Dissertation

zur Erlangung des Doktorgrades
des Department Physik
der Universität Hamburg

vorgelegt von

ALBERT CĂSĂNDRUC

aus Coţuşca, Botoşani, Rumänien

Hamburg 2015

Gutachter/in der Dissertation:	Professor Dr. R.J. Dwayne Miller Professor Dr. Jochen Küpper
Gutachter/in der Disputation:	Professor Dr. Henry Chapman Professor Dr. Nils Huse
Datum der Disputation:	27th of November 2015
Vorsitzender des Prüfungsausschusses:	Professor Dr. Daniela Pfannkuche
Vorsitzender des Promotionsausschusses:	Professor Dr. Jan Louis

Abstract

The dream to control chemical reactions that are essential to life is now closer than ever to gratify. Recent scientific progress has made it possible to investigate phenomena and processes which deploy at the angstroms scale and at rates on the order femtoseconds. Techniques such as Ultrafast Electron Diffraction (UED) are currently able to reveal the spatial atomic configuration of systems with unit cell sizes on the order of a few nanometers with about 100 femtosecond temporal resolution. Still, major advances are needed for structural interrogation of biological systems like protein crystals, which have unit cell sizes of 10 nanometers or larger, and sample sizes of less than one micrometer. For such samples, the performance of these electron-based techniques is now limited by the quality, in particular the brightness, of the electron source.

The current Ph.D. work represents a contribution towards the development and the characterization of electron sources which are essential to static and time-resolved electron diffraction techniques. The focus was on electron source fabrication and electron beam characterization measurements, using the solenoid and the aperture scan techniques, but also on the development and maintenance of the relevant experimental setups. As a result, new experimental facilities are now available in the group and, at the same time, novel concepts for generating electron beams for electron diffraction applications have been developed. In terms of existing electron sources, the capability to trigger and detect field emission from single double-gated field emitter Mo tips was successfully proven. These sharp emitter tips promise high brightness electron beams, but for investigating individual such structures, new engineering was needed. Secondly, the influence of the surface electric field on electron beam properties has been systematically performed for flat Mo photocathodes. This study is very valuable especially for state-of-the-art electron guns where acceleration electric fields as high as $100\,\frac{MV}{m}$ are possible. Regarding the development of novel electron sources, the fabrication of patterned photocathode structures, consisting of micrometric emitters was analyzed. These could bring major advantages in terms of electron beam quality, due to the possibility of controlling the size and the shape of the emitting area. On the other hand, first beam characterization measurements of a new type of electron source, based on optical fibers, were performed. While these structures hold all the advantages of the patterned electron sources discussed above, they proved to be much easier to fabricate and their use require no alignment of optical elements inside vacuum, which is usually subject of setup constraints.

The experimental output of the current Ph.D. work is very promising and pave the way to a new generation of diffraction experiments with capabilities exceeding the limitations faced before.

Zusammenfassung

Der Traum, chemische Reaktionen in lebenden Systemen verstehen und sogar steuern zu können, scheint in greifbarer Nähe zu sein. Jüngste wissenschaftliche Fortschritte ermöglichen es, Phänomene und Prozesse, welche auf eine Längenskala von einem Angström und einer Zeitskala von Femtosekunden stattfinden, zu untersuchen. Diesbezüglich sind insbesondere Methoden wie ultraschnelle Elektronenbeugung (ultrafast electron diffraction, UED) zu nennen, welche Strukturdynamik an Kristallen mit einer Einheitszellengrösse von mehreren Nanometern mit etwa 100 Femtosekunden Zeitauflösung ermöglicht. Dennoch besteht ein grosser Bedarf an Weiterentwicklung dieser Methoden um sie für biologische Proben, insbesondere Proteinkristalle, anwendbar zu machen. Letztere weisen relativ große Einheitszellen im 10 Nanometer Bereich auf, jedoch nur relativ kleine Probengrössen von etwa einem Mikrometer, sodass die Helligkeit der Elektronenquelle umso mehr ausschlaggebend für die Anwendbarkeit von UED ist.

Die vorliegende Doktorarbeit stellt einen Beitrag zur Entwicklung und Charakterisierung von Elektronenquellen dar, welche für zeitaufgelöste als auch statische Elektronenbeugungsexperimente tauglich sind. Der Schwerpunkt der Arbeiten liegt in der Fertigung von Elektronenquellen und deren Charakterisierung mittels ”solenoid scan” und ”aperture scan” Methoden. Konstruktion und Instandhaltung der hierzu notwendigen Versuchsaufbauten bildete einen wesentlichen Teil der Tätigkeiten, und die entstandenen Einrichtungen stehen der Arbeitsgruppe nun zur Verfügung. Gelichzeitig wurden neuartige Konzepte zur Erzeugung von Elektronenstrahlen für Elektronenbeugungsversuche entwickelt, es wurde aber auch an der Weiterentwicklung bestehender Elektronenquellen gearbeitet. So wurde Feldemission von einzelnen Spindt-Typ Emittern, welche sich aus einer auf einem chip integrierten Molybdän Nanospitze und einer Extraktor- sowie Kollimatorelektrode zusammensetzen, erstmals gezeigt. Die hohe potentielle Helligkeit von großflächigen Arrays solcher emitter wurde somit auch für einzelne Emitter gezeigt. Des Weiteren wurden die Eigenschaften von fotoelektrisch erzeugten Elektronenstrahlen an planaren Molybdänoberflächen in Abhängigkeit des elektrischen Extraktionsfeldes an diesen Fotokathoden systematisch untersucht. Die Ergebnisse dieser Studie sind besonders relevant und Wertvoll bezäglich Anwendungen in Elektronenbeschleunigern welche Feldstärken bis zu 100 MV/m aufweisen. Die Herstellung und Untersuchung mikroskopisch strukturierte Fotokathoden als Elektronenquellen mit einer genau abstimmbaren Emissionsfläche und Form zur besseren Reglung der Strahlqualität zählt zu den neuartigen Entwicklungen der vorliegenden Arbeit. Besonders bequem herzustellen und einsetzbar ist die ebenfalls neuartig entwickelte Elektronenquelle bestehend aus Metallbeschichteten optischen Fasern als hochwertige Fotoelektronenquelle, welche die Vorteile von strukturierten Fotokathoden geschickt mit integriertem optischen Anschluss kombiniert, und somit die Notwendigkeit einer aufwändigen Ausrichtung optischer Elemente vermeidet.

Die Experimentellen Entwicklungen der vorliegenden Doktorarbeit sind sehr aussichtsreich und ebnen den Weg fär eine neue Generation von Elektronenbeugungsexperimenten welche heutige Möglichkeiten übertreffen.

Declaration

Declaration on oath

I hereby declare, on oath, that I have written the present dissertation by my own and have not used other than the acknowledged resources and aids.

Eidesstattliche Versicherung

Hiermit erkläre ich an Eides statt, dass ich die vorliegende Dissertationsschrift selbst verfasst und keine anderen als die angegebenen Quellen und Hilfsmittel benutzt habe.

Dedication

To my daughter, Sabina Căsăndruc:

Să ai o viaţă bună şi să fii fericită fetiţa !!!

Life is a simple process meant to help us understand what is and what it takes to be happy. After every major event, positive or negative, encountered on our way, we form new ideas about what we have to change to build a better future. Unfortunately, most of the times we only realize too late that all we need is exactly what we have . . .

Outline

List of Figures ix

List of Tables xv

1. Introduction 1

2. Electron emission and beam characterization: theoretical considerations 5

2.1. Electron emission mechanisms 7

2.1.1. Thermionic electron emission 7

2.1.2. The Schottky effect 8

2.1.3. Field electron emission: Fowler-Nordheim equations 9

2.1.4. Photoemission 11

2.2. Free electron beam properties 13

2.2.1. Correlated and uncorrelated angular spread 13

2.2.2. Emittance 14

2.2.3. Brightness 17

2.2.4. Coherence length 17

2.3. The three-step model for photoemission 18

2.4. Methods for emittance measurement 21

2.4.1. Solenoid scan technique 21

2.4.2. Aperture scan technique 23

3. Description of relevant experimental apparatuses 25

3.1. Test chamber 26

3.2. Interferometer 29

3.3. E-gun 300 30

3.4. REGAE 31

3.5. Electron beam deposition machine 34

3.6. Fiber polishing techniques: manual and automatic 35

4. Front illuminated sources **38**
4.1. Patterned metal photocathodes 39
4.2. Characterization of flat Mo photocathodes 43
4.2.1. QE and TE measurements 44
4.2.2. Theoretical follow-up 53
4.2.3. Electron photoemission as a function of the laser intensity 55
4.3. Double-gated nanoemiters 56

5. Fiber-based electron sources **61**
5.1. Optical fiber tips 62
5.1.1. Field emission measurements 64
5.1.2. Photo-field emission measurements 66
5.2. Flat fiber-based electron sources 74
5.3. High electric field applications 83
5.3.1. Test using the E-Gun 300 88
5.4. Two photon photoemission 92

6. Conclusions and outlook **95**

A. Forthcoming measurements: Single crystal Au photocathodes **99**

B. Maple code for calculating and plotting emittance using the three-step model for photoemission **101**

C. FEA sample holder drawings **104**

Bibliography **108**

List of Figures

2.1. Fermi-Dirac distribution at different absolute temperatures, for gold (Au) 8
2.2. Schottky work function $\phi_{Schottky}$ as a function of the electric field at the surface (flat surface is assumed) 10
2.3. (a) The concept of linearly correlated angular spread (beam divergence) and (b) the uncorrelated local angular spread σ_θ. 14
2.4. Trace space distribution of an ideal electron beam 15
2.5. Representation of the maximum angle of escape (θ_{max}) and the cone of escape. Electrons can only escape into vacuum if their trajectories (blue arrow) forms an angle with the normal to the surface equal or smaller than θ_{max} 20

3.1. CAD model of the vacuum chamber used to build the "Test chamber" . . 27
3.2. (a) CAD model of the "Test chamber" including all beam-line elements;(b) CAD model of the 2D translation system mounted directly on the vacuum flange;(c) CAD model of the beam-line (side view) 28
3.3. (a) "Interferometer" experimental setup;(b) Schottky emitter module;(c) Sketch of the beam-line (the picture was made by Robert Bücker) 30
3.4. (a) E-gun 300 experimental setup;(b) 300 kV power supply;(c) Sketch of the beamline and main component parts 32
3.5. REGAE beamline 33
3.6. (a) Electron beam deposition facility used for all metal thin layer coatings studied in the content of the current thesis; (b) Main panel of the user interface used to operate the deposition machine 34
3.7. (a) Official drawing from Thorlabs for the standard ceramic fiber connector, part no. 30128A3; (b) Official drawing from Thorlabs for the holder used for the manual polishing, part no. D50-FC/APC 36
3.8. (a) Overview of the bare fiber polishing machine; (b) Side view of the optical fiber mounted on a conical ferrule and, in the inset, a view from below with the polished surface 37

4.1. Photoemission results from a 15 nm and a 30 nm thick Pt sample, deposited on a bulk Mo substrate, a 6 nm adhesive Ti layer being added in between. (a) Emission current as a function of the incident laser power and (b) the log-log representation of the same data (red dots and black squares respectively) and linear fits (red and black lines) 41
4.2. QE results on two 4 mm in diameter, 50 nm thick Au layers, deposited on a 100 nm Pt layer (cathode number 810.1), and on a 50 nm Pt layer (cathode number 811.1) respectively. These measurements as well as the plot were made by Sven Lederer from DESY 42
4.3. (a) Sketch of a 50 μm in diameter and 50 nm thick Au dot, coated on a 100 nm thick Pt layer (view from above) and, on the right, a real image taken with an optical microscope; (b) Sketch of the same structure viewed from the side 43
4.4. Experimental configuration showing the main elements of the setup, the triggering laser beam path (blue) and the electron beam path from cathode to the detection screen (red) 45
4.5. The UV laser beam profile at the photocathode 46
4.6. Measured QE of the Mo photocathode as a function of the surface electric field 47
4.7. The second field integral F_2 as a function of the electric current through the solenoid (black squares) and a linear fit (red line) 50
4.8. (a) Experimental configuration; (b) The RMS beam size at the screen as a function of the electric current through the solenoid (blue dots) and the fit (red line) with the envelope equation, including only the solenoid and the drift to the screen, at 20kV, (c) 40 kV, (d) 60kV and (e) 80kV 51
4.9. Normalized emittance on the two directions (X and Y) as a function of the acceleration voltage at the solenoid position 52
4.10. (a) Normalized emittance prediction using the TSMP (equation 4.12), as a function of the acceleration electric field, and assuming a work function of $\phi = 4.6eV$. (b) Same as (a) but assuming a 2PPE process and therefore a photon energy of 9.32 eV instead of 4.66 eV as in case of single-photon photoemission 54
4.11. (a) Average emission current as a function of the laser power for each of the four acceleration voltages: 20, 40, 60 and 80 kV respectively; (b) Emission current as a function of the laser power for a surface electric field of 8 MV/m. Both axes are logarithmic and two linear fits have been performed trying to point out the two different regimes: single and two-photon photoemission 55

4.12. Sketch of the chip containing six double-gated nanoemitters. The sketch, and the chip, were provided by Patrick Helfestein and Soichiro Tsujino from the Paul Scherrer Institut (PSI) in Switzerland 57
4.13. (a) Picture with the top part of the special designed chip holder (with the chip mounted) and indications of the relevant details; (b) Picture with the bottom part of the chip holder mounted on a 2D translation system (on the vacuum flange) 58
4.14. Picture with the beam-line where the electron source (the chip with the 6 field-emitters) and the other relevant beam-line components are indicated 60
4.15. (a) Measured current-voltage characteristic on single double-gated Mo field emitter and (b) published data for a field emitter array (FEA) chip (Mustonen et. al., APL 99, 2011) 60

5.1. Sketch of a Cr/Au pre-coated pulled NSOM optical fiber tip 63
5.2. Description of the experimental setup and the electrical circuit 64
5.3. Experimental data: (a) current-voltage (I-V) emission curve for a 40 nm Cr coated tip and (b) for a 40 nm Pt coated tip 65
5.4. Current-voltage curve for a 10 nm W coated tip 65
5.5. Current-voltage curve (squares) and the corresponding Fowler-Nordheim fit (solid line) 66
5.6. Component parts of the optical fiber feedthrough purchased from Nanonics Inc. 68
5.7. Response of electron emission to application of laser for an unconditioned tip, and in the presence of no field-emission current (black squares); the applied 405 nm CW laser power (red solid line) 69
5.8. Response of electron emission to application of laser for the conditioned tip, and in the presence of a field-emission current of about 180 pA (black squares); the applied 405 nm CWlaser power (red solid line) 70
5.9. SEM image of a fiber tip (a) before the experiment and (b) after measurements and conditioning (b) 71
5.10. (a) Thermocouple sketch and the basic circuit and (b) the thermocouple voltage calibration 72
5.11. (a) Description of the setup used to measure the thermal transient triggered by the application of the 405 nm CW optical excitation; (b) In-air temperature switch-on curve after triggering the fiber tip with the 405 nm CW laser (black squares) and the fast optically enhanced electron emission switch-on curve from figure 5.8 72

5.12. (a) Optical transmission over time for two types of fibers: fiber cut from the NSOM fiber tip (red) and fiber cut from the solarisation rezistant fiber from Thorlabs (black); (b) Optical transmission as a function of time for the solarisation rezistant fiber from Thorlabs (longer time period and longer fiber extension (a)) 75
5.13. (a) Calibration of the laser power as a function of the position of the ND filter at two positions: at the end of the extension fiber cut (black) and at the photocathode position (red); (b) Spectrum of the used pulsed laser beam 76
5.14. (a) Thorlabs drawing of the two-sided fiber connector used between the extension and the cathode fiber cuts and (b) picture with the Cr/Au coated fiber plug and the electrical contact between the emitter layer and the plug metallic section 77
5.15. Electron emission current as a function of the laser power (black squares) and a linear fit (red line) 78
5.16. Picture with the experimental configuration where the relevant parts are indicated 79
5.17. Measurement results for a 50 μm core size NSOM optical fiber. (a) Center of the transmitted electron beam (through the aperture slit), at the screen position, as a function of the aperture position; (b) Electron beam profile at the aperture position; (c) Experimental configuration; (d) Size of the transmitted electron beam (through the aperture slit), at the screen position, derived from the 2D Gaussian fit (black squares) and from RMS calculation (red squares); (e) 2D Gaussian fit of the transmitted electron beam where the axes are in pixels and, in the inset, image with the actual transmitted electron beam on the screen 80
5.18. Measurement results for a 100 μm core size solarization resistant optical fiber.(a) Center of the transmitted electron beam (through the aperture slit), at the screen position, as a function of the aperture position; (b) Electron beam profile at the aperture position; (c) Experimental configuration; (d) Size of the transmitted electron beam (through the aperture slit), at the screen position, derived from the 2D Gaussian fit (black squares) and from RMS calculation (red squares); (e) 2D Gaussian fit of the transmitted electron beam where the axes are in pixels and, in the inset, image with the actual transmitted electron beam on the screen 82
5.19. (a) Measured emission electron current as a function of the laser power (black squares) and linear fit (red); (b) log-log representation of the same data (black squares) and linear fit (red) 83
5.20. (a) The standard REGAE plug with the optical fiber fed through its center; (b) The same assembly featuring a Cr/Au coating (after polishing) 84

5.21. Test holder for the optical fiber-based electron source for high electric field applications 85
5.22. Fiber holder for high electric field applications (a) view from above and (b) view from below; (c) Optical microscope pictures with each of the four bore sizes (0.2, 0.25, 0.3 and 0.4 mm) after the optical fiber was attached and the surface was polished and Cr/Au coated 86
5.23. (a) Thorlabs drawing of the metallic fiber optic connector; (b) Custom designed large area flat photocathode holder, on which the Thorlabs metallic fiber connector can be attached 87
5.24. (a) Sketch of the fiber-based photocathode assembly used for the high electric field photoemission test and (b) a picture with the actual assembly featuring a 25 nm Au layer on top of a 3 nm Cr coating 87
5.25. (a) Picture with the high voltage fiber-based photocathode mounted on the e-gun 300 standard cathode holder; (b) Picture with the gun section of the e-gun 300 setup 88
5.26. (a) Picture with the E-gun 300 gun section, after attaching the CF300 vacuum flange, but without the fiber feedhtough and (b) the same as before but with the fiber feedthrough attached. The optical fiber can be also seen coming out of the feedthrough 89
5.27. Laser beam path. The UV laser path is controled using two Al coated mirrors before it is coupled into the extension fiber. The connection between the extension and the cathode fiber is achieved using a double-sided fiber coupler 90
5.28. (a) First electron beam detected at e-gun 300 using a fiber-based photocathode biased to an electric field of 70 kV; (b) 2D Gaussian fit of the electron beam shown in (a) 90
5.29. (a) Experimental configuration; (b) Electron beam profile at the aperture position; (c) 2D Gaussian fit of the transmitted electron beam, in the inset, image with the actual transmitted electron beam on the screen 91
5.30. (a) Experimental configuration; (b) The RMS beam size at the screen as a function of the electric current through the solenoid (blue dots) and the fit (red line) with the envelope equation, including only the solenoid and the drift to the screen, at 70kV 92
5.31. Experimental setup used to test the possibility of two photon photoemission from Cr/Au coated, 3 μm core size single-mode optical fibers. The setup has attached two fiber feedthroughs: one was used for all the measurements presented above in this chapter and a new one which was attached for the use of the single-mode fibers with 532 nm laser wavelength 93

C.1. Drawings of the FEA sample holder (top part) 104
C.2. Drawings of the FEA sample holder (bottom part) 105

List of Tables

2.1. General notations used in this theory chapter 6

4.1. Relevant values and material properties of Mo used for the experiment . . 45

1. Introduction

The world as we know it today has been shaped by the scientific progress along history. The two most important technological achievements, from the authors point of view, are the use of thermal energy to generate mechanical work, first through the means of steam power [1], and the discovery of electricity and of the possibility to produce and store electrical energy [2, 3]. Without an additional source of energy, the capability of mankind to auto-sustain and evolve would have been limited by the human physical potential to work and exploit the land and the easily available natural resources. A turning point was then met when mechanical work started to be used at a large scale, in the 18th century. Subsequently, the discovery of electricity has introduced new standards in life and an immeasurable development potential. As a direct effect, a population increase of more than 7 times was encountered in the last 300 years, following a nearly exponential trend. Therewith, the general curiosity of humanity slowly commuted from basic to more fundamental aspects of life.

As there is proof of important knowledge in the fields of mathematics, medicine and astronomy, dating from the times of Egyptians, Arabs and ancient Greeks, the birth of science as an independent field of study took place more recently in Europe. About 400-500 years ago, around the 16th and 17th century, scholars like Nicolaus Copernicus, Johannes Kepler, Galileo Galilei and Isaac Newton have introduced to the world a new manner of describing natural phenomenas and facts from the surrounding world. This new concept of the scientific method was based on experimental verification and rational thinking derived from fundamental principles. This was therefore seen to be competing with the other ways of dealing with these aspects at that time, like religion. Despite the eventual discordances between science and religion, which constitute the subject of very interesting debates even in our days, the need of humanity for knowledge could not be abolished and has triumphed over the years. As a response, in the 19th century, modern science has been professionalized and institutionalized and, shortly after this, the scientific progress made possible a technological revolution which has literally changed the world.

Certainly, one of the most appealing subjects that science deals with in our days is

linked to the origins and functionality of living organisms. The main challenges in this respect are to resolve the structure, as well as the relation between the structure and the functionality of biological systems. Apart from the need to statically reveal the spatial atomic configuration of these systems of interest, a more deep insight is gained if information about the dynamics undergone during structural changes are available. This could eventually make it possible to control the chemical reactions that are essential to life. Unfortunately, at the roots of what it can be observed on the macroscopic scale, a challenging congestion of phenomenas and processes remain, which deploy at dimensions and rates hardly accessible for investigation. In this context, the scientific community has been trying to develop tools that can provide "snapshots" of systems with minute sizes, down to the size of an atom, in the angstroms range ($1\,\text{Å} = 10^{-10}$ meters), and with time resolutions in the femtosecond range ($1\,\text{fs} = 10^{-15}$ seconds), required for time resolved studies. Two distinct types of radiation have been used so far as probe for structure determination: X-rays, used initially in crystallography experiments [4,5], and electron beams which came into play more recently [6]. The later constitutes the subject of the current Ph.D. work and will be discussed in details further in the content of this thesis.

After electrons were first referred to as individual charged particles contained in atoms by Joseph John Thomson in 1897, it was Louis de Broglie who proposed their wave-particle duality in his Ph.D. thesis in 1924. Only three years later, in 1927, Davisson and Germer proved experimentally de Broglie's theory [7]. By firing an electron beam on a thin Au sheet and recording the transmitted beam, they observed that the pattern on the screen does not reveal randomly distributed scattered particles. Contrary, when the Bragg condition: $n \cdot \lambda = 2 \cdot d \cdot \sin\theta$ is satisfied, interferences fringes were observed, similar to those produced by electromagnetic radiation. In the Bragg equation, n is an integer number, λ is the wavelength associated to the electron beam, d is the lattice constant and θ is the angle between the incident electron beam trajectory and a direction perpendicular to the material surface. These considerations stay at the foundation of electron diffraction techniques, which consist of structure reconstruction based on information contained in diffraction patterns. As opposed to X-rays, electrons have a much larger scattering cross section, which provide good diffraction quality at relatively low electron densities. Therefore, electron beams are good candidates for time resolved structure determination studies of samples with thicknesses of up to $1\,\mu m$ [6, 8–10]. These properties lead in the last decades to a significant expansion of electron-based techniques among research groups around the globe. Currently their applications embrace ultrafast and dynamic transmission electron microscopy (UTEM and DTEM) [11–13], X-ray Free Electron Laser (XFELs) injectors [14, 15] and have recently been applied in Ultrafast Electron Diffraction (UED) methods where integrated in sub-picosecond photoelectron guns [6, 9, 10, 16, 17], with the scope of pushing the limits of time resolved studies to the capabilities of resolving key dynamics that undergo within biological systems.

As with any method, electron diffraction techniques bring not only advantages but also have drawbacks and limitations. Although the technique has shown great capabilities to statically resolve inorganic structures with unit cell sizes of a few nanometers (1 nm = 10^{-9} m) [10], advances are still needed to match the resolution requirements for studying more complex systems (biological) with larger unit cell sizes. More importantly, the goal is to reveal the atomic configuration of these systems from information contained in ultrafast single shot diffraction patterns, which gives then the possibility of recording snap-shots of the atomic spatial distribution at intermediate time points during chemical reactions. For these time resolved applications, pulsed radiation sources are implied and the spatial and temporal resolutions discussed above are required simultaneously, the new notion of space-time resolution being introduced here. At the same time, a high enough brightness to give sufficient contrast on the diffraction pattern is critical.

As the electron beam intensity, which is a limiting factor for time resolved applications, is proportional to the number of electrons per unit area, it could be therefore increased by a tighter focus of the electron beam, if the number of electrons per bunch is kept constant or, for a given beam size, by extracting more electrons. Both of these are limited by the properties of the electron source. Although strong enough magnets are available, there is a finite focusing limit dictated not only by the wavelength but also by the initial quality of the electron beam. This is because the electron optics (magnets) apply smooth forces changing the trajectories of individual electrons by the same amount, any initial deviation of the beam from parallelism being propagated all the way to the focal point, which is most of the time at the sample position. On the other hand, the number of electrons that can be extracted is also depending on the distribution of the electronic states inside the emitter material. The spatial resolution is limited by the presence of a randomly distributed orientation of the electron trajectories at the source (angular spread). This spread dictates the coherence length of the beam, defined as in the electromagnetic radiation case, which is in fact the main limitation when it comes to resolving large unit cell systems. On the other hand, the temporal resolution is also dictated by the electron source employed in the experiment. The initial electron bunch length is given by the nature of the trigger, which in case of laser pulses can be as short as femtoseconds (1 fs = $10^{-15}s$), and by the response time of the photocathode material. Due to the electrostatic nature of electrons, especially if the size and duration of the electron bunches overcomes a given threshold (the so called *space charge* regime is entered), temporal and spatial resolutions are interconnected, and one can only be improved in the detriment of the other for a constant number of electrons per bunch and for a given initial electron beam quality. As an example, an electron bunch with a duration of 200 fs where 10^5 electrons are focused down to a $50\,\mu m$ spot size could be considered. If it is one intended to reduce the spot size at the focus, this will automatically lead to a prolongation of the bunch due

to the electrostatic forces between electrons (space charge) which become significant in these extreme conditions. Similarly, if the bunch is compressed to reduce the pulse duration, which is now possible using re-bunching cavities [10, 18, 19], this will lead to a broadening on the transversal direction due to the same space charge effects, and each electron trajectory will be transfered a velocity component perpendicular to the direction of propagation. This will therefore be to the detriment of the spatial resolution of the beam. To conclude, the means to push ahead the limits of electron-based techniques are by advancing the electron source to yet unknown terrain, or by developing new measurement or detection tools that could extract more useful information while using the existent electron source technology. Here, the very problem of the electron source improvement is addressed.

• • •

The current Ph.D. work represents a contribution to the characterization and development of free electron sources needed for electron diffraction experiments with the ultimate goal, but not the sole, of solving the structure of large unit cell biological systems as well as the dynamics of these during key structural changes. The following chapters in this thesis can be split in three main categories: theory, setup description and electron source fabrication and characterization.

The second chapter is theoretical and introduces the concepts and methods implied in the experimental sections of the thesis. Firstly, relevant electron emission mechanisms are described, then the most general properties of electron beams are introduced. At the end of the chapter, two methods that have been used in the experimental section for beam characterization are presented from a theoretical point of view. Next, chapter three, is a technical section where all the experimental setups and facilities that have been developed, or used by the author during his Ph.D. work are presented. Here, the basic structures of four electron guns are discussed. Moreover, other existing facilities that were used for sample fabrication are also enumerated. Chapters four and five presents original measurements and results. In chapter four, electron beam characterization measurements performed by the author on electron sources that are to be used in front-illumination configuration are shown. This includes measurements on both, flat and sharp emitters. In chapter five, results on a novel electron sources that can be operated as sharp as well as flat emitters (and are also compatible with high electric filed environments) are shown. These are fiber-based electron sources which represents the main achievement of the current Ph.D. work. In the last chapter, number six, a final enumeration of the results is made and further plans are discussed. At the end of the thesis, relevant technical drawings, simulation codes or experimental plans are attached as appendixes. The thesis ends with bibliography and acknowledgments.

2. Electron emission and beam characterization: theoretical considerations

In this chapter, the general mechanisms for producing free electrons are introduced followed by a theoretical description of the main methods and properties used to characterize electron beams. The theoretical discussions are limited to concepts and methods relevant to the experimental work described in chapters 4 and 5.

Apart from the intrinsic properties of materials under study, like work function, shape and surface quality, electron emission is strongly affected by three external factors: temperature, electric field, and photoexcitation. Therefore three main emission processes can individually take place: thermal emission, field emission, and electron emission due to the photoelectric effect. In the first section of this chapter, each of these will be discussed as well as the relevant combination of these processes [20], with the main emphasis on field-assisted photoemission. Also, two theoretical models used to describe emission processes and/or analyze experimental data will also be briefly discussed. These are the Fowler-Nordheim approach, discussed together with the Schottky effect in sections 2.1.2 and 2.1.3, and the three-step model for photoemission presented in section 2.3.

In section 2.2, the most common notions used to describe the quality of an electron beam are presented. Along these lines, the concept of angular spread, emittance, brightness, and coherence length are discussed. At the end of the chapter (section 2.4), the two most used techniques for measuring beam emittance are presented form a theoretical point of view. These two, the *aperture scan technique* and the *solenoid scan technique*, have been used during the experiments that make the core of the current work and the results are included in the following chapters. To ease the course of explication withing this theoretical chapter, a definition of all notations used here is given in table 2.1.

Table I: General notations used in this theory chapter

Notation	Definition
B	Brightness
B_{FN}	Fowler-Nordheim constant
A_{FN}	Fowler-Nordheim constant
β	Normalized velocity (v/c)
β_F	Electric field enhancement factor
c	Speed of light
e	Electron charge
E	Energy
E_F	Fermi energy
E_{kin}	Kinetic energy
E_{ph}	Photon energy
ε_0	Electric permeability of vacuum
ε_n	Normalized emittance
f	Focal length
F	Electrostatic force
F_a	Enhanced electric field (in case of sharp tips)
F_c	Effective surface electric field (large electrodes assumption)
f_{FD}	Fermi-Dirac density of occupied electronic states
J	Current density
γ	Lorenz factor
h	Planck constant
k	Imaginary part of the refractive index
k_b	Boltzman constant
l	Distance
L_x	Transverse coherence length
λ	Laser wavelength
λ_{e-e}	Electron-electron scattering length
λ_{opt}	Optical penetration depth
m	Electron mass
ν	Light frequency
R	Optical reflectivity
σ_p	Momentum spread
σ_x	Beam size
σ_θ	Local angular spread
ϕ	Metal work function (for bulk)
ϕ_{eff}	Effective work function
$\phi_{Schottky}$	Work function reduction due to applied electric field
p_{z-rel}	Relativistic electron momentum
T	Absolute temperature
θ	Angle
v	Velocity
V	Voltage
ΔV	Potential difference
x	Distance (position)
x'	Angle

Table 2.1.: General notations used in this theory chapter

2.1. Electron emission mechanisms

As mentioned above, there are three typical processes that can trigger electron emission. A general description of each process will be given below and the compatibility of each of them with time resolved electron diffraction applications is discussed. First, thermionic emission will be briefed followed by the Schottky effect, cold field emission, and the Fowler-Nordheim model for field emission. The photoelectric effect, which is most relevant for time resolved applications, will be discussed last in this section.

2.1.1. Thermionic electron emission

Thermionic electron emission is historically one of the first studied mechanisms for emitting electrons. Experimentally it was observed that the temperature increase of a metallic sample, above a threshold value, leads to electron emission. Also, if the sample was already emitting electrons, a temperature change above a given threshold will have an effect on the emission rate. This is observed while all other properties are kept constant. Assuming an initial Fermi-Dirac distribution of electronic states inside the metal, the change of temperature will have an additional impact on the emission current due to the changes in the electron distribution over the available energetic states, as predicted by equation 2.1.

$$f_{FD}(E) = \frac{1}{e^{\frac{E-E_F}{k_b \cdot T}} + 1} \tag{2.1}$$

In figure 2.1 it can be seen that, for Gold (Au) which has the Fermi level $E_F = 5.4\,\mathrm{eV}$, at temperatures above $T = 0\,\mathrm{K}$, energetic states above the Fermi level E_F will be populated. If no extraction electric field is encountered at the metal surface, above a certain temperature, the kinetic energy of a temperature-dependent fraction of electrons will be large enough to trigger emission over the potential barrier, which is the material work function ϕ. If the source is already in the electron emission regime, due to one of the other mechanisms which will also be discussed below, the temperature change will have an impact on the emission current.

Electron emission over the barrier is called *thermionic emission* and it was observed to be exponentially dependent on the temperature of the emitter as reported by Richardson in 1901 [21]. A few years later, he published the mathematical description of the thermionic current density dependence on the temperature, as shown in equation 2.2:

$$J = A_G \cdot T^2 \cdot e^{-\frac{\phi}{k_b \cdot T}} \tag{2.2}$$

Here the term A_G is a constant that depends on the material under observation. Richardson's theory accounts for the pure *thermionic emission* which takes place at low

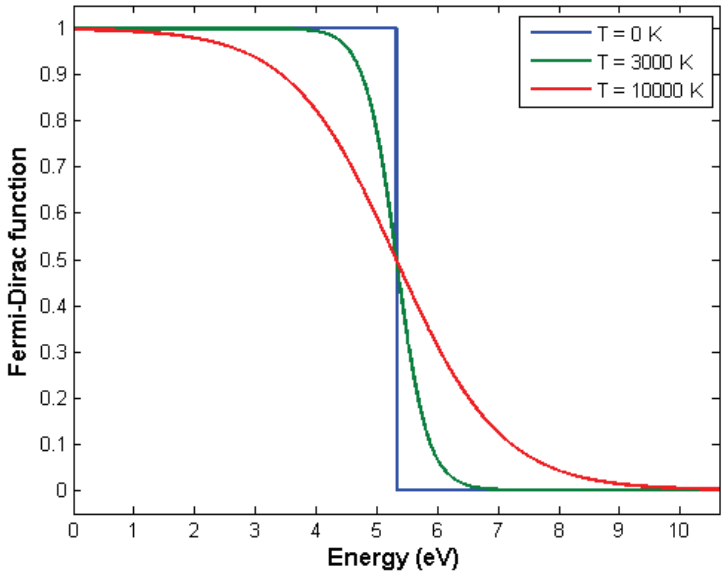

Figure 2.1.: Fermi-Dirac distribution at different absolute temperatures, for gold (Au)

electric field strength, below 1 MV/m, and if the emitter temperature overcomes a threshold and enters the so called Richardson regime.

Thermionic electron sources can provide large enough beam currents for electron diffraction applications and are easily available. Still, due to the high thermal agitation of the lattice, the electron probability to scatter before being emitted is high, which leads to a random distribution of emitted electron trajectories. This will of course give undesired beam properties as it will be discussed later in this chapter (sections 2.2.1 and 2.2.2). Also, the main drawback of pure thermionic sources is that they cannot provide pulsed emission with time resolution better than milliseconds, due to the slow nature of thermal effects.

2.1.2. The Schottky effect

Within many state-of-the-art electron-beam based setups, a large electric field is applied at the source surface. This is to preserve the initial beam properties and to increase the emission current by overcoming space charge effects or to match the sample requirements. Measurements have shown that stable electron emission (e.g. saturation thermionic emission) is enhanced by the application of such external electric fields. Compared to thermionic emission discussed above, which is based on the increase of electron kinetic energy and emission over the metal potential barrier, in case of electric field application, the potential barrier is reduced due to image charge forces. The amount of work function energy reduction has been derived by Walter Hans Schottky [22] in 1914 and

named after him the Schottky work function $\phi_{Schottky}$. For this derivation, Schottky assumed that the electric forces are oriented perpendicular to the surface of a metal. When an electron that leaves the lattice is situated at a distance x from the surface, a positive image charge will be created at the same distance from the interface, but on the opposite direction, inside the metal. This will act with a retarding force on the first particle. The magnitude of the electrostatic potential $V_{Schottky}$ corresponding to this force, given $a < x$ the inter-atomic distance, is proportional to the work function of the metal and is given by equation 2.3:

$$V_{Schottky} = \frac{e}{16 \cdot \pi \cdot \varepsilon_0 \cdot x^2} \tag{2.3}$$

Now, if an external electric field is applied, this will lead to a change of this electrostatic potential, reducing it in the case of an acceleration electric field. The amount of the corresponding work function reduction depends upon the strength of the electric field F_a, as predicted by the equation 2.4 [23].

$$\phi_{Schottky} = e \cdot \sqrt{\frac{e \cdot F_a}{4 \cdot \pi \cdot \varepsilon_0}} \tag{2.4}$$

The electric field notated here with F_a accounts also for field enhancements which are present in case of sharp emitters. Therefore, $F_a = \beta_F \cdot F_c$ with β_F the enhancement factor (which equals 1 in case of flat surfaces) and $F_c = \frac{\Delta V}{d}$ the constant uniform electric field, where d is the distance between the electron source (cathode) and the anode plate (large electrodes assumption), and ΔV the potential difference. Figure 2.2 shows that $\phi_{Schottky}$ can have values on the order of a few eV at electric fields on the order of $\frac{GV}{m}$, which is the same order of magnitude with the work function of common metals used as electron sources for diffraction applications.

These high fields are hardly achievable in case of flat photocathodes due to electric breakdown which, depending on the surface quality, becomes significant for fields above $10\,\frac{MV}{m}$. On the other hand, in case of sharp tips, the field is enhanced close to the apex and such values are realistic. Therefore, in this case, electrons tunnel through the reduced potential barrier (the reduced work function of the metal ϕ_{eff}) and the so called *cold electron emission* is possible. This, together with the Fowler-Nordheim approach, which is typically used to explain field emission results, are discussed next.

2.1.3. Field electron emission: Fowler-Nordheim equations

Just as electron emission is enhanced by a temperature increase, the electric field at the cathode surface changes the shape and magnitude of the potential barrier due to

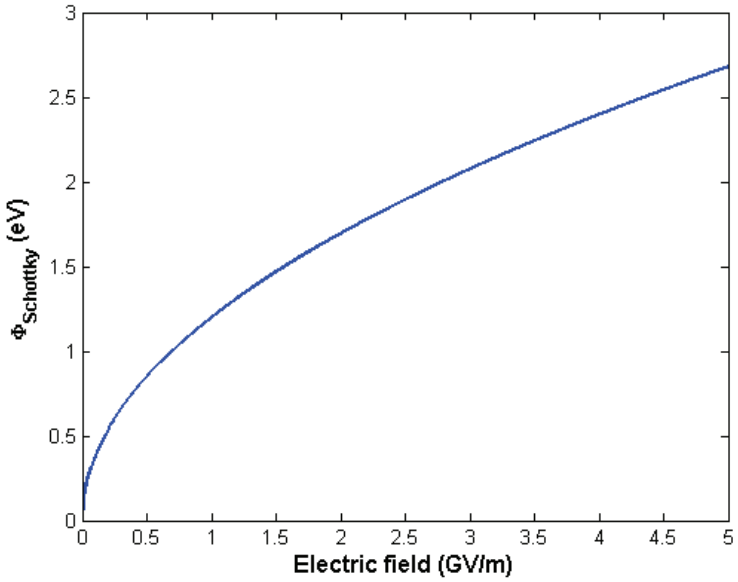

Figure 2.2.: Schottky work function $\phi_{Schottky}$ as a function of the electric field at the surface (flat surface is assumed)

image charge forces which will in turn induce a variation of the emission current. As discussed above in section 2.1.2, the magnitude of the applied electric field could reach values that are sufficient to extract free electrons from the material, leading to the process called *field electron emission* or simply *cold emission*. To avoid any confusion, it has to be clarified that, as compared to thermionic emission, in case of cold field emission electrons could escape by tunneling from states above but also below the Fermi level E_F. Generally, this process becomes predominant for field values on the order of $\frac{GV}{m}$. First released theoretical model of the mechanism of field emission, originally derived for bulk flat surfaces, has been released by Ralph H. Fowler and Lothar Woflgang Nordheim in 1928 [24]. Equivalent to the thermionic emission presented above in section 2.1.1, Fowler and Nordheim proposed a set of equations meant to predict the dependency of the emission current density on the strength of the applied electric field 2.5.

$$I = A_{FN} \cdot \left(\frac{V}{B_{FN}}\right)^2 \cdot e^{-\frac{B_{FN}}{V}} \tag{2.5}$$

After the release of this theory, an intense use and reformulation of these equations and treatment has been encountered. More recent work based on a publication by Murphy and Good in 1956 [25] has resulted in the release of an unified theory [26] that is combining field and thermionic emission. Experiments have also proven that a significant influence on the emission current is induced by relatively low field strengths [27]. The Fowler-Nordheim theory has been proven to be very valuable and can be used to infer the amount of work function reduction. This is normally highly dependent on cathode shape and surface quality, parameters that are not trivial to control experimentally. To

infer the effective work function $\phi_{eff} = \phi - \phi_{Schottky}$, experimental data on the variation of the electron emission current is as a function of applied surface electric field is needed. This so called current-voltage (I-V) curve can be fit using equation 2.5 with the constants A_{FN} and B_{FN} as fit parameters.

$$B_{FN} = \frac{b \cdot \phi^{\frac{3}{2}}}{F_a} \tag{2.6}$$

Assuming that the electric field at the source is proportional to the applied voltage V, the fit result A_{FN} will be proportional to the emission area and B_{FN} to the electric field F_a. The equality from equation 2.6 [28], where b is constant[1], is used to infer the electric field at the emission surface. This will then be used to calculate the work function reduction using equation 2.4 from section 2.1.2. Knowing that $F_a = \beta \cdot F_c$, as already mentioned in section 2.1.2, the filed enhancement factor β_F is also accessible. This fit method was used to analyze I-V data in section 5.1.1.

Despite the fact that the above described method gives fairly good results for the field enhancement factor β_F or for the work function of the metal ϕ, recent theoretical and experimental treatments [29–32] have introduced to the scientific community slightly different formulations of the initial equations derived by Fowler and Nordheim. The main claim is that the equation 2.5 must not be used to interpret data from sharp emitters and more general modified forms of the equation are proposed [33, 34]. This aspect is still not fully clarified and a more detailed discussion in this respect is beyond the subject of the current thesis.

Field emission based electron sources are more promising than thermionic sources for electron diffraction applications due to their faster response time and higher emission currents. Via electronic pulsing, electric fields can be switched on and off within ns, and therefore shorter electron bunches than in the thermionic emission case can be created.

2.1.4. Photoemission

As a matter of coincidence, the first official documentation of electron emission triggered by an electromagnetic radiation, which to a large extend constitutes the subject of the current work, finds its roots in the city of Hamburg. The physicist Heinrich Rudolf Hertz, born in Hamburg in 1857, showed for the first time that electric sparks from an electrode are facilitated by ultraviolet light irradiation. Through his manuscript entitled *"Über enen Einfluss des ultravioletten Lichtes auf die electrische Entladung"* [35], Hertz opened up the field of photoemission. Short time after this publication, the work of Thom-

[1] b= $6.83089 \frac{eV^{\frac{3}{2}} \cdot V}{nm}$ [28]

son [36] and Lenard [37] have verified experimentally these observations and the notion of *photoelectric effect* has been introduced.

According to Maxwell's electromagnetic theory of light [38, 39], which was well established at that time, the *photoelectric effect* takes place due to the energy transfer between the light and the electrons inside the metal lattice. If this assumption is correct, a variation of the incident light wavelength will lead to a variation of the emission rate. Also, following this logic, photoemission should be possible at any wavelength and, at very low powers, a lag between the light excitation and the emission time is expected. As opposed to these, experiments proved that electrons are only emitted if the photon energy of the incident electromagnetic radiation reaches or exceeds a given threshold, the work function ϕ of the material. Also, by increasing the light intensity, only the number of the emitted electrons increases, not their energy. Therefore, a better understanding of the process was needed and major efforts have been put into the theoretical treatment of photoemission by the leading scientists of that time.

The concept of the photon, implying that light can only be absorbed or emitted in wavelength dependent quanta, was the solution to these questions. After Max Plank explained the blackbody spectrum by introducing a relation between light frequency ν and a corresponding quantum energy with the proportionality constant h: $E_{ph} = h \cdot \nu$, it was Albert Einstein in "Annus Mirabilis" (Miracle year - 1905) who published the theory for photoemission [40] in the form that it is known in the present. This work awarded him the Nobel prize in 1921 [41]. Conforming to his theory, the kinetic energy of a photoemitted electron E_{kin} scales with the energy of the triggering photons as shown in equation 2.7.

$$E_{kin} = h \cdot \nu - \phi \tag{2.7}$$

If the photon energy is higher than the work function of the material, the process is called single photon photoemission (SPPE). This is because the energy of each individual photon is sufficiently large to excite and electron out of the lattice. In some cases, when sufficiently large laser intensities are used, electron emission is also possible at photon energies below the work function of the material. This is due to multiple excitation events encountered by the same electron. In these conditions, the process is called multi-photon photoemission (2PPE, 3PPE, etc.).

Electron emission due to the photoelectric effect is the most commonly used mechanism to produce electrons for fast/ultrafast time resolved applications. This is due to the very fast emission time (in the femtoseconds range) as well as the availability of ultrashort electromagnetic pulses (on the order of femtoseconds) from the state-of-the-art laser sources. Also, as compared to field and thermionic emission, a larger emission current is achievable via the photoelectric effect.

2.2. Free electron beam properties

In this section, the notions of electron beam angular spread, emittance, brightness and coherence will be defined. Two basic mathematical concepts, which are commonly used with electron beams, are first introduced: the weighted average and the root-mean-square RMS.

Particle beams (bunches) are described in a six dimensional position-momentum space, the phase space, in which in a classical picture each particle is uniquely defined by its position. In this case, when calculating the center of the distribution, or the center of mass, the amplitudes (or the weights) of the other physical properties, momenta in this case, at each position have to be considered. Therefore, the weighted average is introduced which, for a given bunch observable q, can be calculated using:

$$\langle q \rangle = \frac{\sum w_q \cdot q}{\sum w_q} \tag{2.8}$$

The other very useful mathematical tool is the root-mean-square *RMS*. While this can be applied to any distribution, it is mostly needed when dealing with nonuniform distributions (electron beam transversal distribution), which are difficult to define using standard geometrical shapes. In this case, measuring or calculating the spatial extent of the distribution is rather impossible in the classical way and the root-mean-square *RMS* value is commonly used instead. This is calculated using equation 2.9:

$$q_{rms} = \sqrt{\langle q^2 \rangle - \langle q \rangle^2} \tag{2.9}$$

2.2.1. Correlated and uncorrelated angular spread

In this section, the notions of correlated, uncorrelated and local angular spread, as well as the notion of beam divergence will be explained. A finite number of electron trajectories is considered (notated from A to E), indicated by blue arrows in Figure 2.3 (a), which are photoemitted from a flat surface of a metal-vacuum interface. In this given example, at each point on the photocathode surface (along the x coordinate) a single individual trajectory is possible. Also, as the distance from the photocathode center increases, the angle θ_i between the electrons trajectories and the z coordinate (the normal to the photocathode surface) increases too, i. e. $\theta_3 < \theta_2 < \theta_1$ and $\theta_4 < \theta_5 < \theta_6$. This is to say that there is a correlation between the position x and the angle θ_i and therefore a *correlated angular spread* is present. Moreover, if the correlation is linear then the notion of the *beam divergence* can be discussed based on the notations in figure 2.3 (a), and the divergence angle can be defined as $\Theta = \theta_1 + \theta_6$. The *linearly correlated angular spread* does not reveal the quality of an electron source material. The correlation between the electron emission angle and the position could be given by the photocathode shape or the distri-

bution of an electric field present at the surface, and its effect on the electron beam size can be undone by using a lens. If there is no correlation between the emission angle and position, an *uncorrelated angular spread* is present. In practice, the *uncorrelated angular spread* is strongly influenced by the quality of the photocathode surface which is not perfectly flat. Generally, the larger the surface roughness is, the larger the *uncorrelated angular spread* will be. This is a limiting property of the electron beam quality, as will be discussed below, and due to its randomness it cannot be controlled by the action of smooth forces (a lens).

In a realistic case, at each given position on the photocathode surface, a random angular spread of electron trajectories is present as shown in figure 2.3 (b) (for the trajectory notated with *B* in figure 2.3 (a)). This is called *local angular spread* σ_θ and it is also in the detriment of the electron beam quality being the main source of the *uncorrelated angular spread* discussed above.

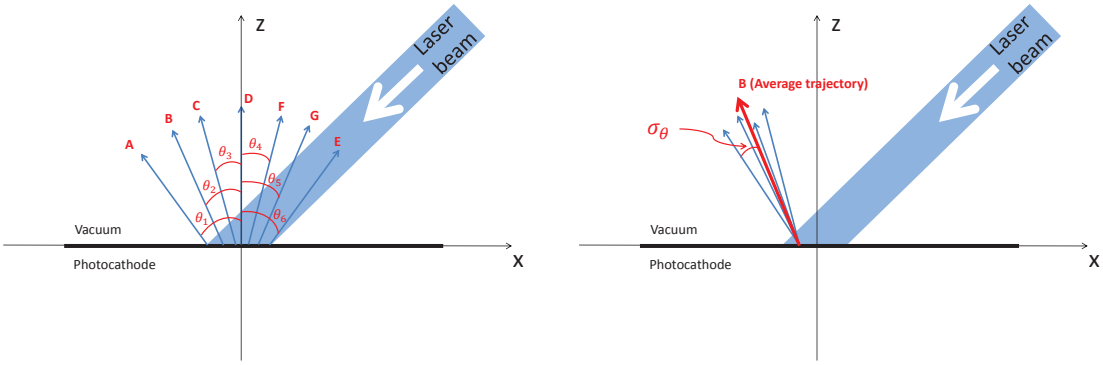

(a) (b)

Figure 2.3.: (a) The concept of linearly correlated angular spread (beam divergence) and (b) the uncorrelated local angular spread σ_θ.

2.2.2. Emittance

Despite the large amount of theoretical and experimental work done on defining and measuring the emittance of an electron beam [42–50], a curious confusion is still present regarding the correct definition of different emittance types: geometric, intrinsic, thermal or normalized emittance. In this section, a description of each of these is attempted. The emittance of an electron beam, usually used under the notation ε, is a measure of the beam quality concerning its parallelism and focusability. It is therefore a qualitative property dealing with the trajectories of individual electrons. The larger the *local angular spread* σ_θ discussed above in section 2.2.1 is, the larger the emittance of the beam will be, which is undesired. As the forces of a linear focusing system (a magnet) will not change

the relation between the direction of propagation of individual particles, the local angular spread of the electron beam at the source will be transfered all the way to the sample. This is therefore a limitation of the spatial resolution, discussed in the introduction, in a space-charge free system. While an ideal electron beam can be focused down to a spot with the radius $d = \frac{\lambda}{2 \cdot NA}$ (the Abbe limit), where λ is the wavelength associated to the electron beam and NA the numerical aperture of the focusing system, a realistic electron beam can only be focused down to a larger spot size, dictated by the local angular spread σ_θ, which is proportional to the transverse velocity spread of the electrons.

In case of a paraxial beam, the angle between the trajectory of an electron and the direction of propagation (which should be smaller than 1 radian for the paraxial approximation to hold) is given by the equation 2.10 where v_x and p_x are the transverse electron velocity and momenta respectively and v_z and p_z are the velocity and momenta along the propagation direction. The same applies for the y coordinate

$$x' = \frac{v_x}{v_z} = \frac{p_x}{p_z} \text{ and } y' = \frac{v_y}{v_z} = \frac{p_x}{p_z} \tag{2.10}$$

Instead of using the velocity, or momentum of electrons [43], which are nontrivial to directly measure, the emittance is more often defined in the *trace space* where the particles are represented as a function of position x and the angle $\theta = x'$, as described above in section 2.2.1, and defined in equation 2.10. If the trajectory of particles across an electron beam are represented in the trace space, typically an ellipsoidal distribution is obtained as shown in figure 2.4.

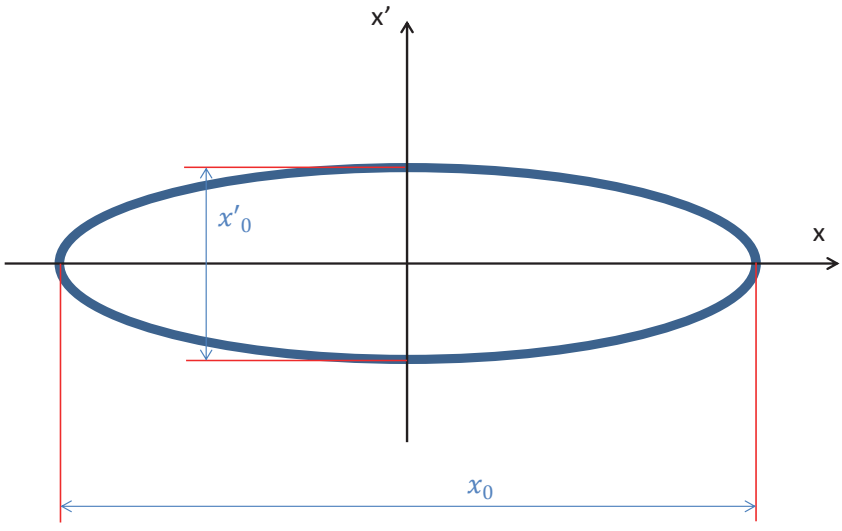

Figure 2.4.: Trace space distribution of an ideal electron beam

$$\iint dx \cdot dx' \tag{2.11}$$

The *geometrical emittance* of an electron beam is proportional to the area of its distribution in the trace space. The standard formulation used to calculate *geometrical emittance* is given by equation 2.11. The measure of unit for the geometrical emittance is $\pi \cdot m \cdot rad$. The intuitive name of *geometrical emittance* is given because it is based on the geometric shape of the distribution in the *trace space*. Sometimes, the geometrical emittance is defined as being equal to the area of the ellipse, in which case the value obtained using equation 2.11 has to be divided by π. In this case the emittance is equal to the ellipse area, the unit of measure changes to $m \cdot rad$ instead of $\pi \cdot m \cdot rad$. Still, most used way is the first one and the measure of unit is $\pi \cdot m \cdot rad$. In case of a realistic beam, the area occupied by the particles in the trace space is not a perfect ellipse. This is why the root-mean-square RMS of the distribution, discussed in section 2.2, is used. In this case, the RMS geometrical emittance becomes:

$$\varepsilon_{rms} = \sqrt{\langle x^2 \rangle \cdot \langle x'^2 \rangle - \langle x \cdot x' \rangle^2} \tag{2.12}$$

Acceleration voltages, which are indispensable in electron accelerators, reduce the geometric emittance. This is simply because the axial average momentum of the beam p_z is increasing while the transverse momentum p_x, which is an intrinsic property of the material for a given photon energy of the triggering laser, stays constant. In this case, the angle x' will decrease which leads to a lower value for ε_{rms}. Under these conditions, it is necessary to define a beam property that remains constant during the acceleration. This is the *rms normalized emittance*, which is a property of the source, being independent on the accelerator properties. The *intrinsic emittance*, or *thermal emittance*, is the emittance right at the source. In the absence of space charge effects and nonuniform forces, emittance is conserved and equal with the thermal emittance. The normalized emittance is calculated by multiplying ε_{rms} with the normalized energy of the beam $\frac{p_z}{m \cdot c}$. In case of nonrelativistic energies, the *rms normalized emittance* is given by equation 2.13 where $\beta = \frac{v_z}{c}$:

$$\varepsilon_{n,rms} = \frac{p_z}{m \cdot c} \cdot \varepsilon_{rms} = \beta \cdot \varepsilon_{rms} \tag{2.13}$$

In case of relativistic energies, the normalized emittance is given by equation 2.14 where γ is the relativistic Lorenz factor, and the average longitudinal momentum takes its relativistic form p_{z-rel} (equation 4.10):

$$\varepsilon_{n,rms} = \frac{p_{z-rel}}{m \cdot c} \cdot \varepsilon_{rms} = \gamma \cdot \beta \cdot \varepsilon_{rms} \tag{2.14}$$

$$p_{z-rel} = \sqrt{\frac{(e \cdot V + m \cdot c^2)^2 - m^2 \cdot c^4}{c^2}} \tag{2.15}$$

2.2.3. Brightness

The brightness of an electron beam could be considered the most important quantity that describes the quality of an electron source. This is because it is depending on both, beam quality, which is also given by the normalized emittance discussed above in section 2.2.2 and, at the same time, on electron beam current. By definition, it is given by the electron current density per unit of solid angle. Considering I the electric current of the beam, and $\varepsilon_{n_x,rms}$ and $\varepsilon_{n_y,rms}$ the normalized emittances on the two directions perpendicular to the direction of propagation, its brightness B is defined as:

$$B = \frac{I}{\pi^2 \cdot \varepsilon_{n_x,rms} \cdot \varepsilon_{n_y,rms}} \tag{2.16}$$

Hence, from equation 2.16, which links the beam brightness to its emittance, it can be seen that the larger the emittance of the beam, the lower the brightness will be at fixed current. Moreover, for a symmetric beam where $\varepsilon_x = \varepsilon_y$, the brightness scales with the square of the emittance.

2.2.4. Coherence length

In order for constructive electron interference to occur, beside the Bragg condition to be fulfilled, the electron beam has to be coherent at the sample position. More precisely, the transverse coherence length L_x has to be larger than the unit cell size of the sample (a). While for laser beams having high spatial coherence this condition can be easily fulfilled, electron beams typically have low coherence lengths. This is due to the finite thermal emittance of the beam. Analogously to optics, the transverse coherence length L_x is the transverse distance, at a given point along the propagation distance (typically at the sample position), after which two rays, which were initially in phase, lose this property. The direct reason for running out of phase is again the angular spread σ_θ discussed above in section 2.2.1. This leads to electrons propagating along different trajectories, traveling therefore different distances between two parallel planes. The transverse coherence length L_x of an electron beam is given by equation 2.18 [9]:

$$L_x = \frac{\lambda}{2 \cdot \pi \cdot \sigma_\theta} \tag{2.17}$$

Using the de Broglie relation $\lambda = \frac{2 \cdot \pi \cdot \hbar}{\sigma_{P_z}}$ and considering $\sigma_\theta = \frac{\sigma_{p_x}}{\sigma_{p_z}}$, where σ_p is the momentum spread, a more simplified relation is found for the beam coherence along the x coordinate [9]:

$$L_x = \frac{\hbar}{\sigma_{p_x}} \tag{2.18}$$

Similar to the Brightness calculation (described above in section 2.2.3), the co-

herence length can also be expressed as a function of the beam emittance, as shown in equation 2.19, where $\sigma_{x,rms}$ is the beam size, m is the electron mass, c is the speed of light and $\varepsilon_{n_x,rms}$ is the normalized emittance.

$$L_x = \frac{\hbar \cdot \sigma_{x,rms}}{m \cdot c \cdot \varepsilon_{n_x,rms}} \tag{2.19}$$

2.3. The three-step model for photoemission

After the work of Einstein at the beginning of the 20th century, a large number of aspects were still not fully understood regarding the process of photoemission. There is a complex mechanism that deploys from the moment when an electromagnetic radiation quantum with energy E_{ph} reaches the surface of a metal, until the excited electron leaves the lattice and escapes into the vacuum. Based on the initial work of C. N. Berglund, W. E. Spicer and W. F. Krolikowsky [51,52], who first proposed the three-step model for photoemission, more recent studies have successfully managed to bring important improvements to this, and convincing experimental verification has been also added [46, 48, 49, 53, 54]. The model has also been proven to be a very good theoretical tool for predicting the QE and TE for metal photocathodes. Moreover, this theoretical treatment takes also into account the surface electric field, describing therefore a combined emission process: field assisted photoemission, which in fact is the most relevant emission mechanism for the present Ph.D. work.

Here, electron emission is described by the probability of a succession of three different steps to occur: photon absorption, electron transport to the metal surface and escape into vacuum. Due to the application of a combination of electric field and laser excitation, the reduced work function of the material ϕ_{eff}, discussed above in section 2.1.2, is considered. Below, a brief description of each step and the relevant equations are presented.

Absorption

In the first step, the probability for the incident photons to be absorbed by the lattice is discussed. At a first instant, a fraction of the photons reaching the metal surface will be reflected. Therefore, the reflectivity of the metal surface R plays an important role here. The probability for a photon to not be reflected by the metal vacuum interface is $(1-R)$. Inside the metal lattice, the electrons obey a Fermi-Dirac distribution $f_{FD}(E)$ given by equation 2.1. In this case, the probability of an incident photon to excite an electron depends upon the availability of the electron in the initial state, at the energy E, as well as the existence of a free electronic state at the energy $E+E_{ph}$. The total number of existent energetic levels, at a given photon energy E_{ph}, is: $\int_{E_F+\phi_{eff}-E_{ph}}^{\infty} f_{FD}(E)dE$, and the number of available energetic states for the excited electrons is $[1-f_{FD}(E+E_{ph})]$. Therefore, with $f_{FD}(E)$ the distribution of the occupied states, the first step of the three-

step model for photoemission, which describes the probability A of an electron to be excited by an incident photon, is given by [46, 48]:

$$A = (1-R) \cdot \int_{E_F+\phi_{eff}-E_{ph}}^{\infty} [1 - f_{FD}(E+E_{ph})] \cdot f_{FD}(E) \cdot dE \tag{2.20}$$

Transport

In the second step, the excited electron will travel through the metal lattice towards the metal-vacuum interface. The probability of an excited electron to reach the surface with sufficient energy to overcome the effective work function of the metal Φ_{eff} depends upon the depth inside the metal where the excitation takes place (the photon penetration depth λ_{opt}) and the mean free path (mean distance that electrons travel before scattering with other electrons from the valence band) for electron-electron scattering λ_{e-e}. Any inelastic scattering event will cancel the escape probability of both involved electrons to escape into vacuum. This is the case when the photon energy is smaller than twice the metal wok function, which is mostly true for the triggering conditions employed in photoguns for electron diffraction experiments. On the other hand, an elastic scattering event will change the electron trajectory which could also stop electrons from being emitted. This is because, after the collision, the electron could be left with an energy normal to the interface which is lower than the effective work function. Therefore, the fraction F_{e-e} of the electrons that reach the surface without any collision, and the probability B for the second step to occur is [46, 48]:

$$B = F_{e-e} = \frac{1}{1+\frac{\lambda_{opt}}{\lambda_{e-e}}} \tag{2.21}$$

While for the optical penetration depth a simple formulation is available, as shown in equation 2.22 with λ the laser wavelength and k the imaginary part of the refractive index, the electron-electron scattering length λ_{e-e} is a more complicated measure to infer. This is because of the lack of information about the scattering cross section between electrons. Nevertheless, for *Cu* photocathodes, this has been derived by Dowell at. al [46, 48] based on previous measurements on *Au* [52]. Another way to infer this value is by having it as a fit parameter when experimental QE or TE data is available. This method will be described in more details later, at the end of the current section.

$$\lambda_{opt} = \frac{\lambda}{4 \cdot \pi \cdot k} \tag{2.22}$$

Escape

In the last step, those electrons that have reached the surface can escape into vacuum

if they are enclosed within the maximum cone of escape. The cone of escape, shown in Figure 2.5, is defined as a function of the maximum energy that the electrons could have (E_{kin}), and the height of the potential barrier (the effective work function of the metal ϕ_{eff}). Therefore, a maximum angle of escape θ_{max}, between the electron direction of propagation and the normal to the metal surface, can be defined as shown in figure 2.5.

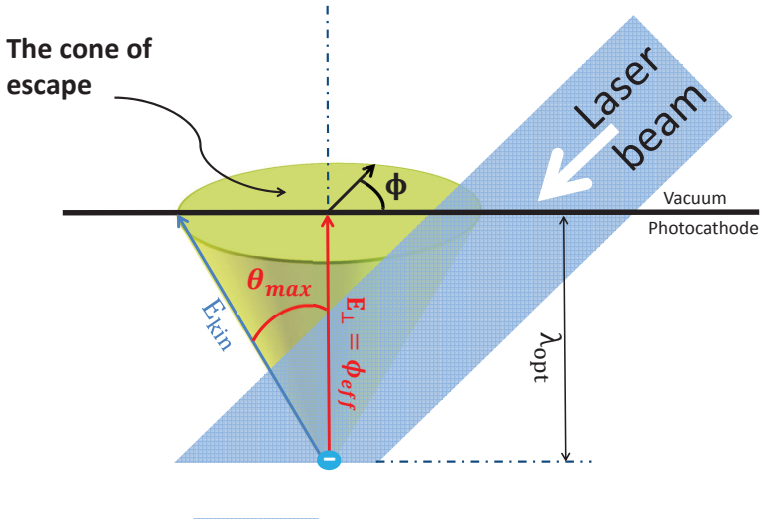

Figure 2.5.: Representation of the maximum angle of escape (θ_{max}) and the cone of escape. Electrons can only escape into vacuum if their trajectories (blue arrow) forms an angle with the normal to the surface equal or smaller than θ_{max}

Electrons that are incident under larger angles will have insufficient energy on the direction parallel to the metal-vacuum interface ($E_{\perp}$) to overcome the work function. The total sum of angles under which electrons can escape is given by: $\int_{\cos\theta_{max}(E)}^{1} d(\cos\theta)$ and the integral $\int_0^{2\pi} d\Phi$ over $2\cdot\pi$ defines the cone of escape. An important aspect to be mentioned here is that the *cone of escape*, and implicit the maximum angle of escape θ_{max}, will increase when the electric field at the cathode surface is increased. This is due to a reduction of the metal work function due to image potential forces as discussed in section 2.1.2. This leads directly to an increase of the QE, but unfortunately also to an increase of the TE. The probability C for the third step to occur is given by:

$$C = \int_{\cos\theta_{max}(E)}^{1} d(\cos\theta) \cdot \int_0^{2\pi} d\Phi \tag{2.23}$$

Now, having a mathematical expression for the probability of each individual step to occur, the total probability P for electron emission via the photoelectric effect will be given by the product of each of these individual probabilities:

$$P = A \cdot B \cdot C = \int_{E_F+\phi_{eff}-E_{ph}}^{\infty} dE \cdot [1 - f_{FD}(E+E_{ph})] \cdot f_{FD}(E) \cdot \int_{\cos\theta_{max}(E)}^{1} d(\cos\theta) \cdot F_{e-e}(E,w,\theta) \cdot \int_0^{2\pi} d\Phi$$

This result can be used to calculate the QE and TE for metal photocathodes. The QE is obtained through dividing the probability P by a new term which assumes that all photons that were not reflected will excite an electron and that the electron will reach the metal surface without scattering. Here, the cone of escape will be the same as above being only a function of the photon energy and the work function. Hence, the QE of metal photocathodes can be calculated using the equation 2.3:

$$QE = (1-R) \cdot \frac{\int_{E_F+\phi_{eff}-E_{ph}}^{\infty} [1 - f_{FD}(E+E_{ph})] \cdot f_{FD}(E) \cdot dE \cdot \int_{\cos\theta_{max}(E)}^{1} d(\cos\theta) \cdot F_{e-e}(E,w,\theta) \cdot \int_0^{2\pi} d\Phi}{\int_{E_F-E_{ph}}^{\infty} [1 - f_{FD}(E+E_{ph})] \cdot f_{FD}(E) \cdot dE \cdot \int_{-1}^{1} d(\cos\theta) \cdot \int_0^{2\pi} d\Phi}$$

If the Fermi-Dirac distribution is replaced by a Heaviside-step function, which is a good approximation at low temperatures, a simpler form of equation 2.3 is found in references [46, 48]:

$$QE \approx \frac{(1-R) \cdot (E_{ph} - \phi_{eff})^2}{8 \cdot \phi_{eff} \cdot \left(1 + \frac{\lambda_{opt}}{\lambda_{e-e}}\right) \cdot (E_F - \phi_{eff})} \tag{2.24}$$

Similar, a derivation for the normalized TE is achieved by the same authors [46,48]:

$$\varepsilon_n = \sigma_x \cdot \sigma_{p_x} = \sigma_x \cdot \sqrt{\frac{E_{ph} - \phi_{eff}}{3 \cdot m \cdot c^2}} \tag{2.25}$$

2.4. Methods for emittance measurement

In this section, two methods for directly measuring the emittance of an electron beam are presented: the solenoid scan and the aperture scan techniques. While the emittance can also be inferred from diffraction patterns, or using the so called pepper-pot method, which is related to the aperture scan technique, only the first two mentioned techniques have been available and experimentally performed as part of the current work.

2.4.1. Solenoid scan technique

The solenoid scan is an experimental technique used to measure the emittance of an electron beam. This is based on performing a waist scan, using a solenoid magnet. More precisely, the magnetic field of a solenoid is varied, so that the electron beam goes through its focus at the detection position. For each value of the magnetic field, the RMS size of the beam on the detector x_{rms} is inferred, and the dependency of this on the field

is obtained. As normally the magnetic field is varied by changing the current passing through the solenoid, a relation between the magnetic field and the solenoid current has to be found. This can be done if a magnetic field map at different electric currents is available. The inverse focal length of the solenoid can be calculated using equation 4.5.

$$\frac{1}{f} = \frac{e^2}{4 \cdot p_z^2} \cdot \int_{-\infty}^{\infty} B(z)^2 dz = \frac{e^2}{4 \cdot p_z^2} \cdot F_2 \tag{2.26}$$

In order to derive the electron beam emittance using the solenoid scan technique, the dependency of x_{rms}^2 on the solenoid current is fit by an equation that describes the motion of the particles through the beamline used for the experiment. Generally, it can be shown that the relation between the initial beam parameters (beam size ($x_{0,rms}$) and angular divergence ($x'_{0,rms}$)), before the beam enters any focusing element, and the final beam parameters at the screen (x_{rms} and x'_{rms}) can be expressed using the matrix formalism [55]:

$$\begin{pmatrix} x_{rms} \\ x'_{rms} \end{pmatrix} = M_{Tr} \cdot \begin{pmatrix} x_{0,rms} \\ x'_{0,rms} \end{pmatrix}$$

The transfer matrix M_{Tr} of the beamline, which is a product of the transfer matrices of all individual electron optics elements, is a 2 by 2 matrix with the form:

$$M_{Tr} = \begin{pmatrix} C_{11} & C_{12} \\ C_{21} & C_{22} \end{pmatrix}$$

The relation between beam size and momentum, before and after the beam propagates through all elements, can be found solving the equation of motion for a bunch of particles [55, 56]. This equation, called the envelope equation 4.3, is used to fit the experimental data discussed above with the coefficients a, b and c as fit parameters:

$$x_{rms}^2 = C_{11}^2 \cdot x_{0,rms}^2 + 2 \cdot C_{11} \cdot C_{12} \cdot x_{0,rms} \cdot x'_{0,rms} + C_{12}^2 \cdot \left(\frac{\varepsilon_{rms}^2}{x_{0,rms}^2} + x'^2_{0,rms} \right) \tag{2.27}$$

or in the matrix notation:

$$x_{rms}^2 = \begin{pmatrix} C_{11}^2 & 2 \cdot C_{11} \cdot C_{12} & C_{12}^2 \end{pmatrix} \begin{pmatrix} a \\ b \\ c \end{pmatrix}$$

with $a = x_{0,rms}^2$, $b = x_{0,rms} \cdot x'_{0,rms}$ and $c = \frac{\varepsilon_{rms}^2}{x_{0,rms}^2} + x'^2_{0,rms}$.

The forms that C_{11} and C_{12} take are dependent on the number of elements contained

in the beamline, but are in the end the product of only two types of transfer matrices: the transfer matrix of a focusing element with a focal length f ($M_{Tr_{sol}}$) and the transfer matrix of a drift region $M_{Tr_{drift}}$ where no magnetic or electric fields are present. In the thin lens approximation the two matrices are given by [55, 56]:

$$M_{Tr_{sol}} = \begin{pmatrix} 1 & 0 \\ -\frac{1}{f} & 1 \end{pmatrix}$$

and

$$M_{Tr_{drift}} = \begin{pmatrix} 1 & l_{drift} \\ 0 & 1 \end{pmatrix}$$

As an example, for the simple case where only a focusing element with the focal length f and a drift length l_{drift} are considered, the two relevant elements from the transfer matrix (C_{11} and C_{12}) are given by equation 4.6.

$$C_{11} == 1 - \frac{l_{drift}}{f} \text{ and } C_{12} = l_{drift} \tag{2.28}$$

2.4.2. Aperture scan technique

The aperture scan technique is the second method used in the current thesis to determine the emittance of an electron beam. This consists of translating a small slit aperture, much smaller than the electron beam size and the distance between the aperture and the detector screen, through an electron beam. The infinitely small size of the aperture slit makes possible to infer the angular spread of the electrons emitted from a point on the photocathode surface, which is the local angular spread discussed in section 2.2.1. Similar to the solenoid scan technique, at each position of the aperture, the size of the electron beam passing through the aperture is determined at the screen position. From the acquired data (images), two important properties of the electron beam can be inferred. One is the RMS size of the beam at the aperture position and the other is the local angular spread. The latter can be calculated if the distance aperture-screen is known while for the first, the intensity of the beam passing through the aperture at each step used during the scan is also needed. This will allow for plotting the beam profile and then calculate the RMS size of the electron beam at the aperture position. In contrast to the first method, the present one does not require any fitting. As shown above in equation 2.11, RMS emittance can be calculated only if the RMS beam size and the angular spread of the beam are known. Both of these are obtained from the aperture scan.

While both of the two methods give good results, both of them have sources of

errors. In the case of the solenoid scan, aberrations of the solenoid can be significant for large electron beam sizes. Also, space charge effects, when significant, will influence the result, leading to an inaccurate determination of the beam emittance. In case of the aperture scan technique, normally the beam is blocked and only a fraction of electrons pass through the slit, which is very small (in the μm range). This leads to a reduction of the space charge effects due to the mean electric field of the beam. It has to also be mentioned here that the aperture could act as an electric lens and change the electron beam size. The maximum angular divergence that can be induced by the aperture can be calculated using equation 2.29 [57,58]. Here, δ is half of the aperture diameter, or half the size of the electron beam for larger apertures, ΔE is the electric field difference between the two sides of the aperture and ΔV is the voltage difference between the anode and cathode (or the kinetic energy of the beam). Nevertheless, this effect is not a source of errors and is not influencing the measurement, the normalized emittance of the beam being constant under the influence of smooth forces (as applied by a linear focusing system, the slit aperture in this case).

$$\sigma_\theta = \frac{\delta \cdot \Delta E}{4 \cdot \Delta V} \tag{2.29}$$

3. Description of relevant experimental apparatuses

The experimental work covered in the current thesis was not only focused on electron source fabrication and characterization but also on the development and design of the setups used for these measurements. The author has been a key factor in the development of two of the total of four setups used during his Ph.D. work, while on the other two setups only some alterations have been made accordingly to each experimental requirements. More precisely, the author has been intimately involved in the design and assembly of two continuous current electron guns with the main, but not the sole purpose, of performing characterization measurements on both, novel and established electron sources. Also, the functionality of the developed setups, where applicable, was tested by using established electron sources which were either obtained through collaboration with other research groups or fabricated by the author. This chapter will give a general description of the four setups as well as a short enumeration of all other apparatuses and procedures that played a critical role in the course of the current Ph.D. work (experimental results are presented in chapters 4 and 5).

The first electron gun, called from now on the *test* chamber, is described in the first section of the current chapter. This project has been developed by the author together with Günther Kassier, as a postdoctoral researcher, the two being initially the only members of the subgroup. First experimental results on this apparatus will be discussed in section 4.3. The second setup, which we will refer to as the *interferometer*, is described and discussed second in this chapter. This project has also been initiated by the author and Günther Kassier, who have design the component parts and mounted together first variant of the setup, before the project was subsequently continued by another member of the group: Robert Bücker. Here, a general outline and description of the scope is given, experimental results not being achieved to date. Thereafter, two other setups on which measurements have been performed as part of the current Ph.D. work are discussed. The first one, *E-gun 300* [59] is a high voltage DC electron gun used to conduct measurements on flat electron sources using the *solenoid scan* or/and the *aperture scan* technique. Results on emittance measurements are included in chapters 4 and 5. Last, but not the least,

is discussed the Relativistic Electron Gun for Atomic Exploration (REGAE) [59, 60]. Although the author has invested a large amount of time performing beamline characterization and electron diffraction experiments on this setup, no electron source characterization measurements were systematically performed. This is because of the restricted access to the electron gun of REGAE, which made nearly impossible exploring new photocathode structures, which have not been properly characterized before. Nevertheless, a first proof-of-principle measurement of the capabilities of REGAE to solve the structure of thick samples, up to 1 μm has been recently published [10]. At the end of the chapter, the metal deposition machine used for all thin layer coatings as well as the fiber polishing methods required for experiments presented in chapter 5 are introduced.

3.1. Test chamber

The current setup was initially planned as a test chamber where the coherence length of an electron beam could be measured by means of interferometry. As the project evolved, space constraints were encountered due to the complexity of the setup and a new larger vacuum chamber was designed and constructed into which all the parts needed for the *interforementer* setup have been moved. The *interferomenter* will be discussed in details in the next section of this chapter. The current chamber has therefore been designed as a low voltage electron gun and its functionality was initially tested on individual double-gated field emitter tips as will be shown in the next chapter (section 4.3). Eventually, this was to become the main experimental setup for all low-field measurements performed on fiber-based photocathodes, which will be discussed later in chapter 5.

As a mater of coincidence, the original pioneering work of Brad Siwick et al. (2003) [8], on ultrafast melting of Al [8], was performed in a setup built around this same vacuum chamber. With the trend towards larger, higher energy UED setups, the chamber became available for other experiments and was subsequently shipped to Hamburg and used for the current project. Figure 3.1 depicts a CAD (computer-aided design) model of the vacuum chamber. This is a commercial vacuum product purchased from Kimball Physics Inc.[1]. As it can be seen, it has a circular shape and features four CF63 and four CF36 horizontal vacuum flanges. The top and the bottom flanges are circular CF160. The height of the chamber is about 120 mm. Regardless of which experiments were performed with this chamber, a few standard parts have always been part of the setup and will be enumerated here. The vacuum is achieved by using a system[2] with a pumping rate of 67 l/s, which is mounted on one of the CF63 flanges. Only using this turbo pump, a base vacuum level down to 3×10^{-9} mbar could be achieved depending on the

[1] MCF800-SphSq-G2E4C4
[2] Pfeiffer HIPace 80



Figure 3.1.: CAD model of the vacuum chamber used to build the "Test chamber"

parts placed inside the chamber. This pressure is at the detection limit of the cold cathode gauge[3] which is mounted on one of the small vacuum flanges. During normal operation, a base pressure in the low 10^{-8} mbar or high 10^{-9} mbar range was usually achieved after one night of pumping.

The electron beam imaging was done using a micro-channel plate (MCP) in front of a phosphor screen mounted on a standard CF100 flange purchased from MDC Vacuum. An increasing rotating extension tube was used to connect the MCP to one of the CF63 flanges on to the vacuum chamber. The MCP features four high voltage (HV) feedthroughs with SHV connectors, with three of which were needed to power the MCP and with the forth being occasionally used to bias different parts from the electron beam line. All power supplies used with this setup[4] have been purchased from SI (Scientific Instruments GmbH). To power the MCP the voltage on the phosphor screen did not exceed 5 KV while the gain between the MCP plate and the phosophor screen was kept below 2.5 KV and the MCP gain, between the two sides of the MCP plate, did not exceed 700 V. This leaves a maximum voltage on the front MCP of not more than 2 KV. The electron source was powered by a source-measure unit[5], which was used to simultaneously apply a bias voltage to the electron emitter and to precisely measure the current running through it. The connection between the SM unit and the electron source inside vacuum, is achieved via a multi-pin vacuum feedthrough and currents in the pA range could be

[3] Pfeiffer PKR 261 active pirani
[4] SRS 350 and SRS 365
[5] Agilent B2902A

measured while a maximum bias of +/-210 V was available.

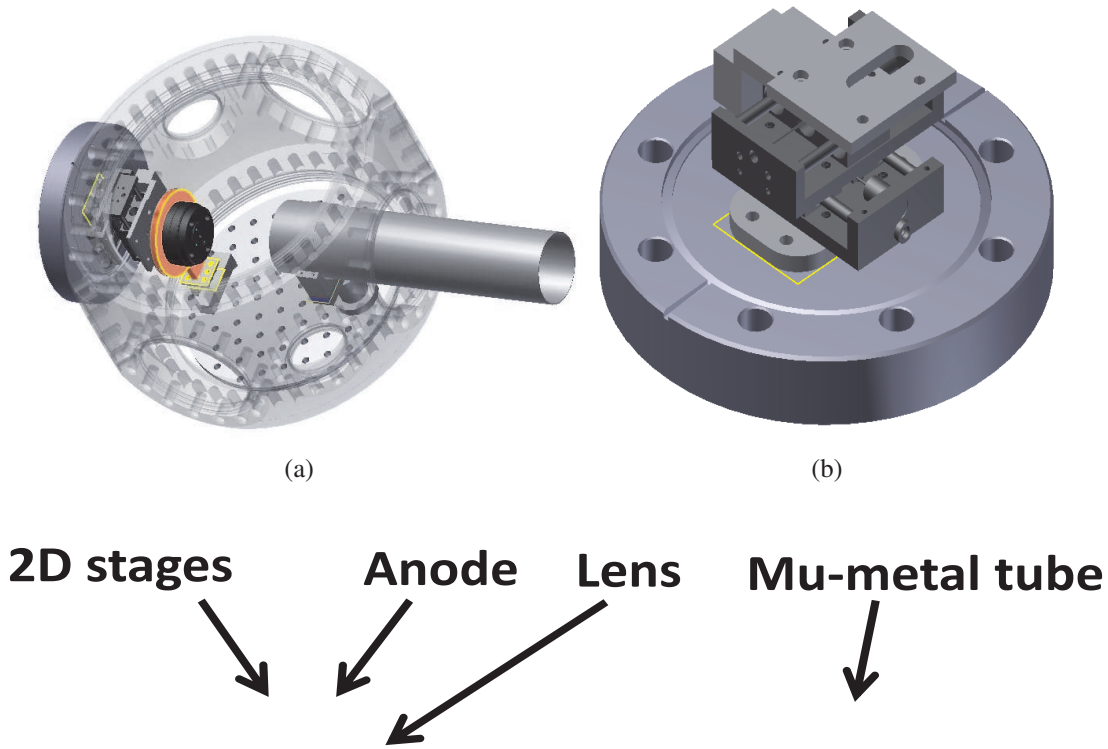

(a) (b)

(c)

Figure 3.2.: (a) CAD model of the ”Test chamber” including all beam-line elements;(b) CAD model of the 2D translation system mounted directly on the vacuum flange;(c) CAD model of the beam-line (side view)

The electron beamline was composed of the electron source, mounted on a two axes translation stage system, an anode plate featuring an electric lens and an aperture, and a mu-metal shielding tube as shown in figure 3.2 (a) and (c). All beam line elements are fixed, except the electron source which can be moved along the two directions perpendicular to the optical axis and can therefore be aligned with the anode aperture. Two ultra high vacuum stick-slip piezo stages with long travel range (20 mm) and 50 nm closed loop precision [6] have been used for this purpose. To gain space inside the vacuum chamber, the translation system was attached vertically directly on the vacuum flange as shown in figure 3.2 (b) and then an adapter plate is attached on top to fit with the electron source holder. The anode plate was 4 mm thick, made of copper and was featuring a 3 mm aperture in the center. Attached to the anode plate a *Einzel* lens was present, consisting of three consecutive electrodes spaced by 5 mm each, which was used to focus the electron

[6] Micos PP-30

beam on to the MCP detector. This lens was mounted on the back side of the anode plate, with respect to the electron source, to allow a cathode-anode distance as short as possible. To power the lens, one of the high voltage feedthroughs on the MCP flange was used and kapton insulated wires were used for the electrical connections. For biasing the source and the anode plate, different configurations could be used depending on the measurement scheme as will be shown later in the current thesis. Finally, a mu-metal tube was used to magnetically shield the beam path all the way to the MCP. Any magnetic fields present in the electron beam propagation region could influence the beam trajectory given its relatively low energy.

3.2. Interferometer

In this section, the second experimental setup, on which development the author was intimately involved, especially during its early design and assembly phase, is described. The aim of this project is to allow for direct measurement of electron beams coherence length by means of electron interferometry [61–63]. The experimental setup and concept are presented in figure 3.3 (a) to (c). The vacuum chamber has a diameter of 300 mm, a height of 200 mm and features four CF100 and four CF63 flanges. The pumping is done using a turbo pump[7] and an ionization getter pump[8] (IGP) pump. A vacuum below 1×10^{-9} mbar was achieved after baking the chamber at 110 degrees for several days.

The electron beam-line is composed of an electron source, anode plate, an Einzel lens, two gratings and a detector as shown in figure 3.3 (c). The electron source (3.3 (b)) is mounted on a translation stage so that the distance between the cathode and anode can be varied over a range of a few cm, and is constructed so that it can be exchanged without requiring any change to the rest of the beam-line or vacuum system. The gun section can be biased to up to -12 KV while the other parts of the beam-line are grounded. After the anode, which has attached the same Einzel lens as discussed in the previous section 3.1, the two gratings are situated, enabling grating interferometry schemes. The gratings have been manufactured through an in-house collaboration with Mrs. Miriam Barthelmes from Professor Henry Chapman's group. Slits of 100 nm pitch and about 50 nm width are milled using a focused ion beam into an Au-coated silicon nitride membrane, spanning an area up to $100\,\mu m^2$. The first grating is placed directly after the anode and the Einzel lens. It is attached to a long-travel, vertically-translating piezo stage (same as used for the previous setup 3.1), and can be exchanged for apertures of different sizes without opening the vacuum chamber. The second grating is mounted to long-travel piezo stages allowing for movement along the beam axis and horizontally. Also, it can be precisely rotated around the optical axis which is required for precise relative alignment and Lau

[7] Pfeiffer 60 l/s
[8] Agilent VacIon 75 SEM

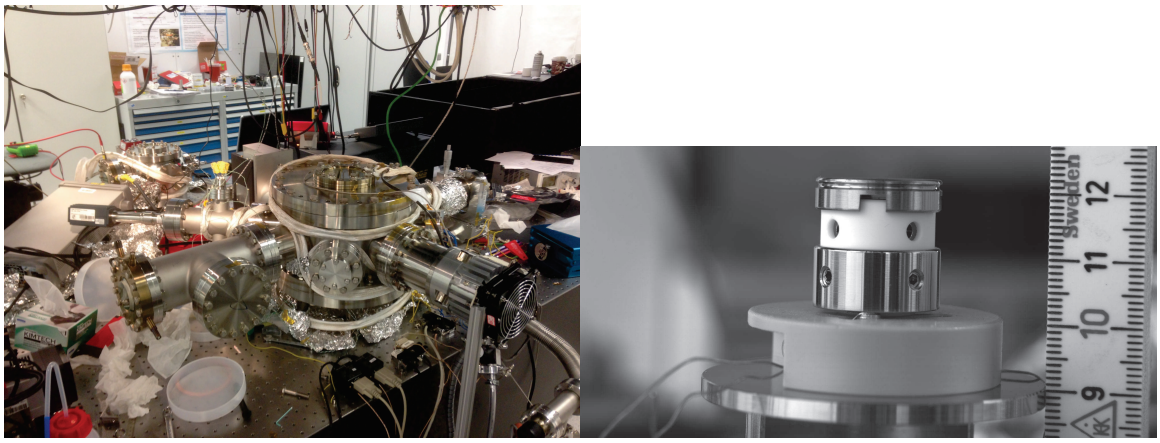

(a) (b)

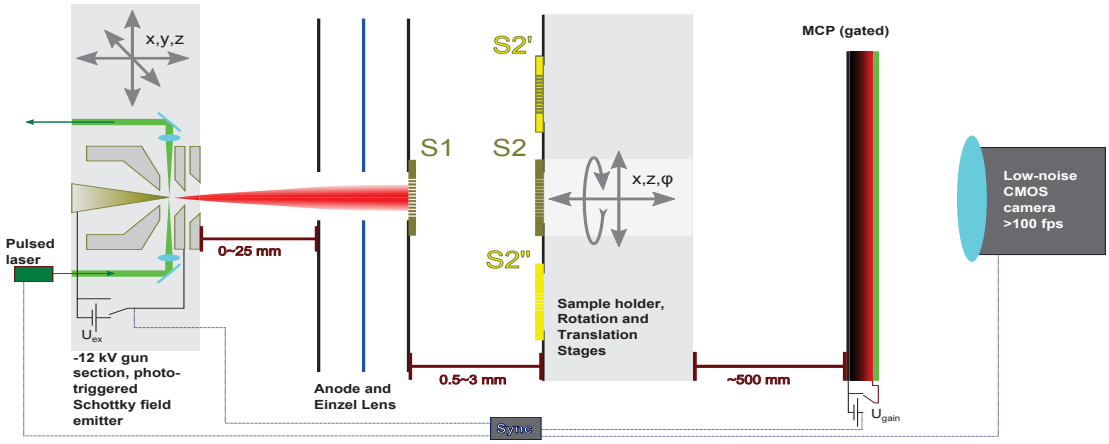

(c)

Figure 3.3.: (a) ”Interferometer” experimental setup;(b) Schottky emitter module;(c) Sketch of the beam-line (the picture was made by Robert Bücker)

interferometry [63]. The bars of both gratings are aligned along the vertical axis. After these, a mu-metal tube is used to shield for magnetic fields and the detection is done using a Photonis MCP.

3.3. E-gun 300

The *E-gun 300* setup [59] is a linear DC electron accelerator where high electron energies (up to 100 keV) can be achieved. While the setup was designed to operate at voltages of up to 300 kV using a commercial high voltage (HV) feedthrough, scaling the feedthrough to 300 kV turned out to be an extremely difficult challenge. Although voltages of up to 300 kV are permitted using the available *Heinzinger* power supply (figure 3.4 (b)), during normal operation the gun could be only biased to a maximum of 120 kV. This was limited by the commercial HV feedthrough. To overcome this problem, new engineering was needed and this made the subject of Julian Hirscht‘s Ph.D. thesis, pub-

lished in 2014.

Figures 3.4 (a) and (c) depict the *E-gun 300* setup and gives a description of the main parts. The electron gun is composed of a photocathode, which is connected to the commercial HV feedthrough, and an anode plate. To trigger photoemission, 266 nm wavelength, 100 fs long laser pulses coming from a frequency-tripled Ti:Sa laser are used. The photocathode holder is made either of macor or stainless steel and allows for variation of cathode-anode distance within a few cm range. The anode plate is a stainless steel disc featuring a 1 cm aperture in the center which can be replaced by smaller apertures, on the order of micrometers, depending on the experiment performed. Normally, the gun is operated in the back-illuminated configuration, and the electron source consists of a common Cr/Au sandwich structure deposited on a fused silica transparent substrate. In this case, an additional smaller aperture, of $100\,\mu m$ in diameter or less, is attached on the anode to shape the electron beam. However, for the two experiments performed by the author on this setup, which will be presented in chapters 4 and 5, the 1 cm anode aperture was used. This is because the electron source was front-illuminated and therefore the large aperture was necessary for the triggering laser to pass trough.

The sample section consists of a manipulator used to move the specimen under study, a magnetic lens after the sample, used to focus the beam on to the detector, a Faraday cup and a phosphor-coupled CCD camera [9]. The sample can be moved along three directions and the magnetic lens can also be aligned with the electron beam being mounted on a two axis translation system. A Faraday cup can be moved in and out of the beam path and the emission current can be measured using an electrometer[10]. As this can only be moved along one direction, the beam is typically focused on the Faraday cup using the magnetic lens. The vacuum is achieved using a scroll pump which backs-up the two turbo pumps[11], mounted on CF100 flanges on the gun and the detection section respectively.

3.4. Relativistic Electron Gun for Atomic Exploration: REGAE

There are two main reasons why a description of the REGAE setup [59, 60] is included in the content of this thesis. On the one hand, the author has invested more than two years as an operator of the REGAE setup, performing beam characterization and electron diffraction experiments. On the other hand, the topic of the current thesis is to increase the performance of present electron sources and REGAE is one of the best candidates for using these sources as it will be explained henceforth in the body of this section.

[9] Princeton Instruments Quad-RO 4320, 24 by $24\,\mu m^2$ pixel size [64]
[10] Keithley 6514
[11] Pfeiffer HiPace 300, 260l/s

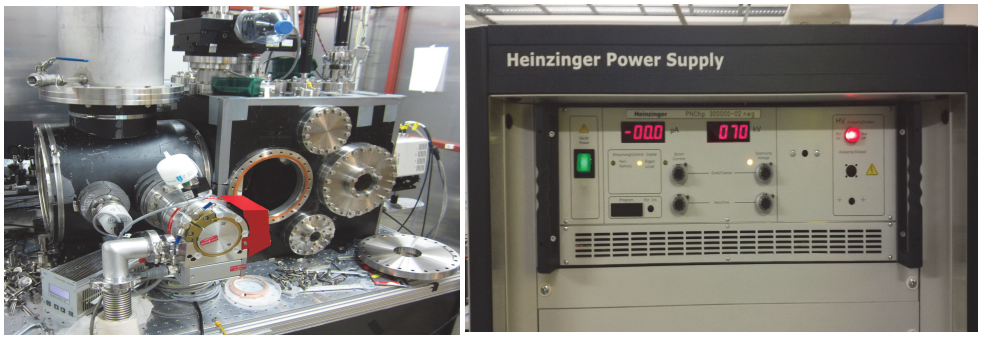

(a) (b)

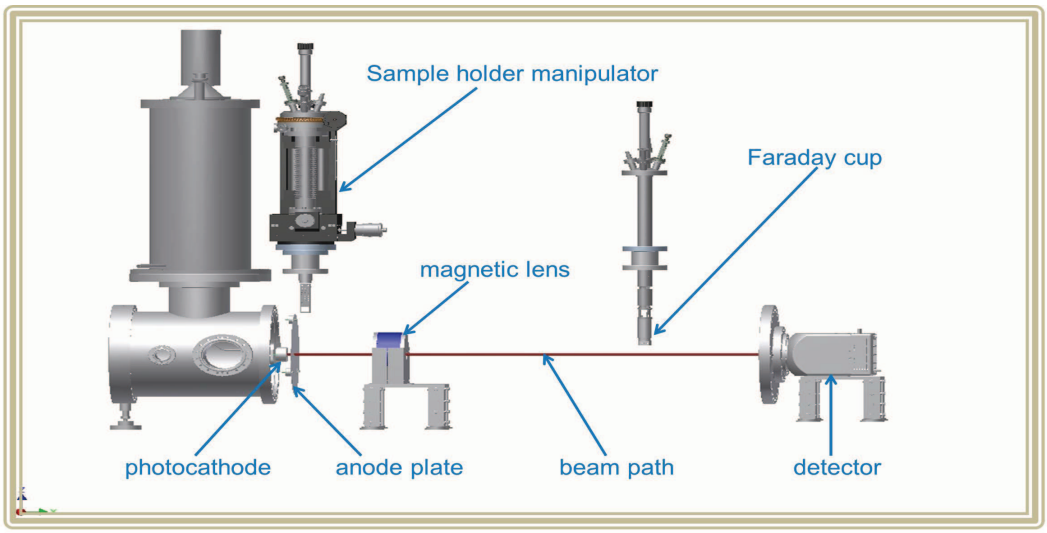

(c)

Figure 3.4.: (a) E-gun 300 experimental setup;(b) 300 kV power supply;(c) Sketch of the beamline and main component parts

REGAE is a radio frequency (RF) electron linear accelerator which can provide short electron bunches with energies of up to 5 MV/m as a result of acceleration electric fields of up to 100 MV/m. The main advantage that the high energy setups bring, as opposed to low energy guns, is that beam properties are better conserved down to the sample position, due to the shorter propagation time, and higher bunch charge densities can be extracted from the cathode, overcoming conventional space charge limitations. At the same time, electron penetration depth into sample is larger, making possible the study of thicker samples, which are more easily accessible from the fabrication point of view. With the central goal to studying structural dynamics in solid, liquid and gas phases of organic and inorganic samples, REGAE provides short pulses and high brightness at the same time. This is possible due to the high energy discussed above but at the same time, due to the electron bunching capabilities of the accelerator. A re-bunching cavity is used to compress the electron pulse at the sample (situated about 5.5 m away) which gives the highest possible temporal resolution. The same klystron amplifier with an RF

splitter is used to drive both, the electron gun and the buncher cavity. For detection, a scintillator in front of a fiber optics plate is used to convert electrons to photons, which are then detected by a Electron Multiplying Charge Coupled Device (EMCCD) chip outside of vacuum, allowing for single electron detection. The electron source is triggered by 266 nm wavelength, 500 fs long laser pulses coming from a frequency-tripled Ti:Sa laser, same as the one used for the *E-gun 300* setup which was presented above in section 3.3. The electron gun is based on front illumination of flat photocathodes and a base pressure on the order of 10×10^{-10} mbar is normally achieved in the gun cavity. Common materials used as electron sources are cesium telluride (Cs_2Te), gold (Au), molybdenum (Mo) and platinum (Pt) and bunch charges in the range from hundreds of fC for metal photocathodes to tens of pC for Cs_2Te can be achieved.

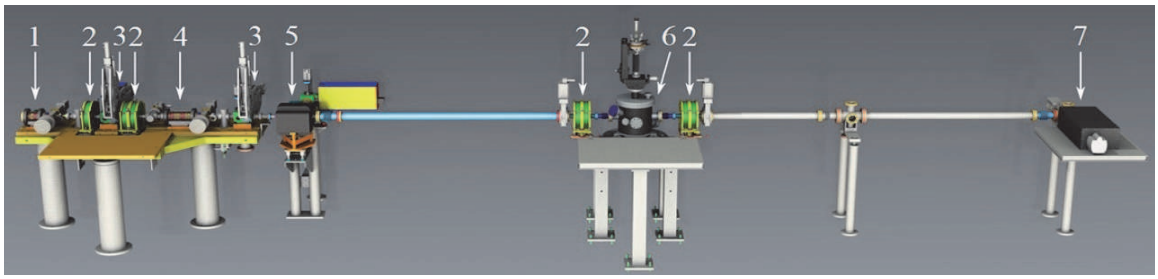

Figure 3.5.: REGAE beamline

Figure 3.5 depicts the setup and enumerates the principal component parts. The numbers in the picture refer to the following parts: (1) gun cavity, (2) solenoids, (3) collimators, (4) re-bunching cavity, (5) dipole for electron energy measurements, (6) target chamber, and (7) detector. After the gun, the beam trajectory and shape is controlled using solenoid magnets, collimators and steerer magnets. The solenoid magnets are placed such that the beam could be focused on any of the three diagnostic screens, one situated right after the gun and the other two after the bunching cavity, but also on the sample or/and the scintillator. Two diagnostic points are used to check the beam shape and current at intermediate points before the sample and a third one, situated after the buncher, allows also for energy measurements using a dipole. A very important part of the beamline are the collimators which feature apertures with different diameters which can be translated in and out of the beam path and are used to shape the electron bunches. Best static diffraction quality was detected while using collimators and having a relatively large beam at the sample position but a tight focus on the detector. In terms of the setup capabilities, first proof of principle experiments have already been published [10]. This manuscript reports on time zero measurements for pump probe experiments and the REGAE capability of solving the structures of thick samples of up to $1\,\mu m$. The author has been a key member who contributed significantly to the experimental part of the last results which were obtained using Al samples with different thicknesses. Still, in the remainder of this thesis no details will be given on these results the focus being rather on the development and

characterization of electron sources for diffraction applications.

3.5. Electron beam deposition machine

All thin layer metal depositions required for fabricating the photocathodes studied as a part of the current Ph.D. work have been conducted by the author using an electron beam deposition machine (figure 3.6 (a)). Here the author would like to acknowledge the help of Professor Henry Chapman and Miriam Barthelmes for granting the access to the clean room facility where the deposition machine was situated and for providing initial user training.

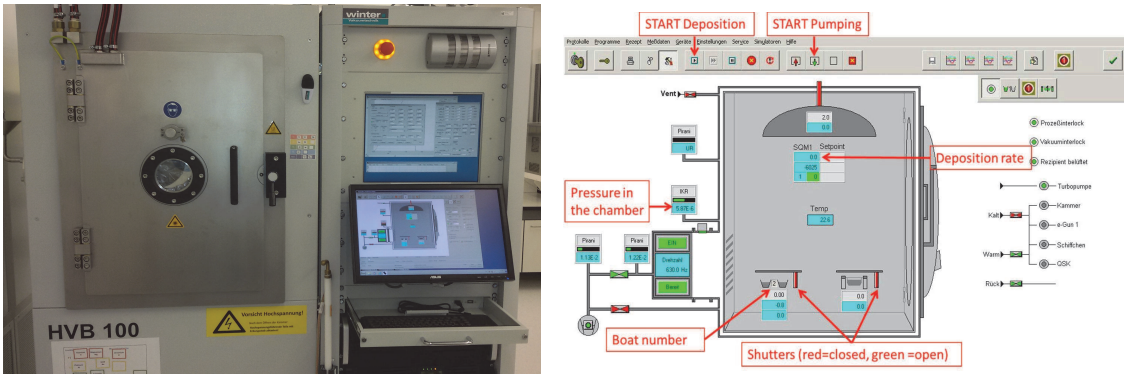

(a) (b)

Figure 3.6.: (a) Electron beam deposition facility used for all metal thin layer coatings studied in the content of the current thesis; (b) Main panel of the user interface used to operate the deposition machine

Overall, the following materials were used for deposition: Chromium (Cr), gold (Au), tungsten (W), aluminum (Al),titanium (Ti) and platinum (Pt). Altogether, layers with thicknesses ranging from 2 to 100 nm were fabricated. The deposition substrate will be mounted above the metal source, facing downwards, and can either be fixed or rotating during the deposition process. While rotating the sample does not give major advantages for flat substrates, it was necessary for obtaining an uniform layer all-around the fiber tips which will be presented later in chapter 5. The principle of operation is relatively simple. First, the sample is attached to a metallic plate holder which is then placed on a rotary stage (rotation is optional) situated above the deposition source. Next, the vacuum chamber is closed and evacuated and the entire process from now can only be controlled by a computer. Figure 3.6 (b) displays the main menu of the facility and the relevant indicators. First, a recipe is loaded where the material, deposition rate in Å/s and the desired thickness in $\mathring{A}$ are specified. Then, the rotation option is checked or not and the deposition process is started. During the entire process, the deposited thickness as well as the temperature around the sample position can be monitored. The maximum

temperature achieved depends on the material to be melted and on the deposition time. For the depositions discussed in the current thesis, a maximum temperature of almost 200 degrees Celsius was detected while using Pt or W as evaporation material.

3.6. Fiber polishing techniques: manual and automatic

A major part of the current work implied the use of optical fibers. As the quality of the photocathode surface (the optical fiber in this case) is limiting factor on the performances of the photocathode, a low surfaces roughness being required to avoid premature electric breakdown, the surfaces need to be prepared before the deposition process described above in section 3.5. In this context, the polishing methods and supplies used for this purpose are explained in the content of this short section. Two polishing methods have been used overall: manual polishing and automatic polishing.

Manual polishing

For coupling the laser beam from free space into the fiber, the optical fiber has to be polished and mounted on a high precision positioner used for alignment. For this purpose, manual polishing is the most convenient and reliable way. This has been done here by using special fiber connectors[12], epoxy[13] and aluminum oxide lapping sheets[14] available from ThorLabs. The usual connectors used for the current work are ceramic FC/APC connectors featuring 8 degrees pre-angled ferrules to reduce back reflections, as shown in figure 3.7 (a). First, the epoxy is injected into the connector using a syringe until in can be seen erupting at the sharp end. Then, the optical fiber is fed through the plug until it comes out at the sharp end of the connector and it is therefore in contact with the epoxy inside the connector. If the diameter of the fiber with the jacked is larger than $125\,\mu m$, which is the bore size of the connectors (figure 3.7 (a)), the fiber has to be stripped before this step. After a few hours of waiting, the glue will be set and the polishing procedure can start. For this step, a standard holder has been used, featuring the same 8 degrees inclination angle on the polishing face as shown in figure 3.7 (b). Three aluminum oxide lapping sheets are used subsequently, with grit sizes of $3\,\mu m$, $1\,\mu m$ and $0.3\,\mu m$, on a flat surface (glass table). After each step, the polishing quality is investigated using a special front illuminated optical hand-microscope, and the process is repeated until the desired surface quality is obtained.

[12] part no. 30128A3
[13] part no. F120
[14] part no. LFG03P: $0.3\,\mu m$ grit size, LFG1P: $1\,\mu m$ grit size and LFG3P: $3\,\mu m$ grit size

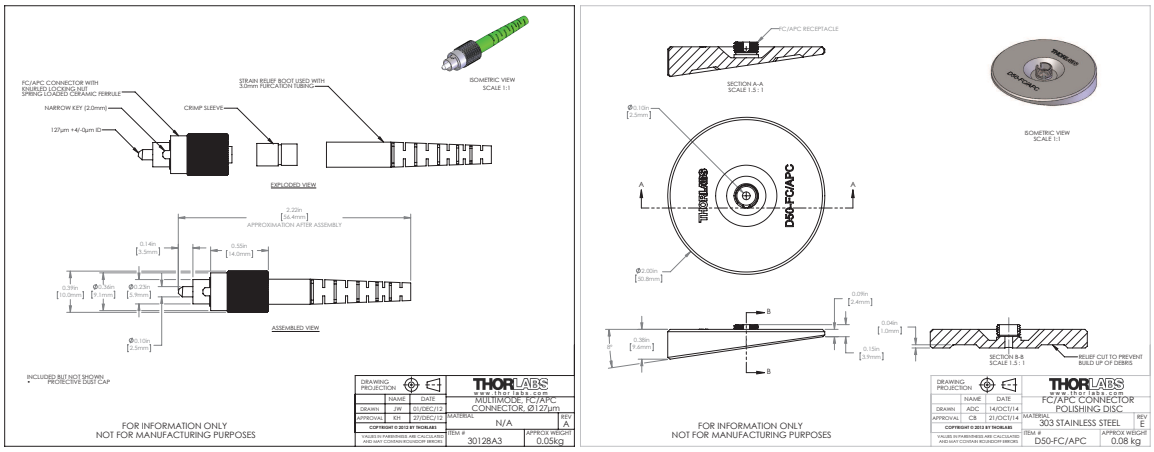

(a) (b)

Figure 3.7.: (a) Official drawing from Thorlabs for the standard ceramic fiber connector, part no. 30128A3; (b) Official drawing from Thorlabs for the holder used for the manual polishing, part no. D50-FC/APC

Automatic polishing

An automatic fiber polishing procedure has been also used in the attempt of creating optical fiber tips with a given tip size, as it will be described in the fifth chapter of the current thesis. A special bare fiber polishing machine (Trig) shown in figure 3.8 (a), purchased from Krelltech [65] was used for this purpose. This facility belongs to the research group headed by Professor Franz Kaertner to whom the author is grateful. This tool makes possible high quality fiber polishing and video cameras are integrated for controlling the process and monitoring the surface quality. First, the fiber is fed through a conical ferrule and fixed to a holder. Then it is moved down until it is in physical contact with the lapping sheet which will be rotating after the process is started. The final diameter of the fiber core at the tip, after the polishing step, is dictated by the size of the conical metallic ferrules used to hold the fiber. An example of how the fiber looks like mounted on a $125\,\mu m$ fiber ferule holder is shown in figure 3.8 (b). For these pictures, two built in cameras were used. One camera is used when bringing the fiber tip in contact with the polishing sheets while the other camera allows for the inspection of the polished surface from below (inset of figure 3.8 (b)). Therefore the process could be investigated and repeated over and over again until the desired surface quality is achieved.



(a) (b)

Figure 3.8.: (a) Overview of the bare fiber polishing machine; (b) Side view of the optical fiber mounted on a conical ferrule and, in the inset, a view from below with the polished surface

4. Development and characterization of front illuminated electron sources

Despite the relatively low QE of metal photocathodes, with respect to their semiconductor analogues [43, 66], their robustness, ultrafast temporal response, and compatibility with high electric fields and relatively large photo-excitation thresholds make them the most commonly used electron sources in state-of-the-art scientific research facilities. Their applications embrace ultrafast and dynamic transmission electron microscopy (UTEM and DTEM) [11–13], X-ray Free Electron Laser (XFELs) injectors [14, 15] and have recently been applied in ultrafast electron diffraction methods where integrated in sub-picosecond photoelectron guns [6, 9, 10, 16, 17]. Given the relatively low number of electrons per bunch (between 10^4 and 10^6) that is required for electron diffraction experiments, metal photocathodes are promising electron sources for time resolved applications tracking ultrafast structural changes within biological systems, due to their fast emission time and sufficient quantum efficiency. As electron optics and laser sources have been developed up to a satisfactory level to meet the temporal resolution and energy requirements, these methods are now limited by the intrinsic properties of the source. For a successful experiment, it is required that the sample unit cell size is smaller or matched by the beam transverse coherence length while each bunch is bright enough to reveal the structure of the sample, in a single shot. There is unfortunately a trade-off between the achievable number of electrons per bunch, and the transverse thermal emittance of the electron beam, which was discussed in the section 2.2.2. The beam coherence is directly related to the thermal emittance which is proportional to the emitting area. Flat metal photocathodes have proven coherence lengths of only a few nanometeres [67] at high electron density bunches while a few tens of nanometers have been measured for single-electron pulses emitted from a sub $100\,\mu$m area [68]. Major efforts have been concentrated towards finding an intermediate solution between the beam emittance and and the beam current and for this scope, the material as well as the influence of the experimental conditions have to be better understood.

Electron sources could be classified in two large categories, flat and sharp emitters. The latter benefit from field enhancements, as discussed in section 2.1.2, and good emittance due to the small emitting area (2.2.2), while large area flat photocathodes can provide a better peak current together with a good time resolution, and have been most used so far in electron beam applications. Following another classification criteria, the laser triggering mode, photocathodes can be split into other two classes: front-illuminated and back-illuminated. The main difference between these two classes is the thickness of the emitter metal. While thin layers can be front or back-illuminated, as it will be discussed in more details in the next chapter, bulk photocathodes can only be front-illuminated.

This chapter brings experimental and theoretical contributions to the characterization of both types of electron sources, flat and sharp-emitters, but which are part of the front-illuminated category. In section 4.1, an original concept of a small-area electron source is presented: the patterned photocathode. The following, section (4.2), presents a systematic investigation of the influence of the surface electric fields on the QE and TE of flat Mo photocathodes. Moreover, the dependence of the electron emission current on the triggering laser intensity is measured. In the last section (4.3), results on field emission measurements performed on single double-gated Mo nanoemitters are shown. These emitters have been fabricated and have been provided for investigation by collaborators Patrick Helfenstein and Soichiro Tsujino from the Paul Scherrer Institute (PSI) in Switzerland.

4.1. Patterned metal photocathodes

The control of the laser beam spot size and profile at the photocathode surface is subject to setup constraints in electron guns. The long laser beam path from the focusing lens, situated usually outside the vacuum, to the photocathode is one of these constraints present at REGAE (section 3.4). More generally, this is the case in electron guns that include an acceleration RF cavity, and a front illuminated photocathode, which is normally implied in high field environments. This is why fabricating a minute photocathode, a few tens of micrometers in diameter, is one solution for achieving low emittance electron beams, where the spot size of the triggering laser could be kept much larger than the emission area, which eases the optical alignment process. Along these lines, the fabrication of a so called ”dot photocathode” was attempted in the current Ph.D. work. This consists of a minute photoemitter dot in the center, which is surrounded by a higher work function metal. The idea behind this concept is that the substrate metal will not emit electrons at the used laser wavelength, and only the patterned structure deposited in the center will do. In this context, the spot size of the triggering laser can be kept large and it does not have to be perfectly centered on the photocathode. The two main challenges that have to

be overcome in order to fabricate such a device are the difficulty of evaporating a small metallic dot, smaller than 100 μm in diameter, and finding the right metals that give a high enough contrast between the emitter and the surrounding substrate, in therms of effective work function, and of course quantum efficiency (QE).

Based on the work function values found in literature for bulk metals, and also due to their robustness, for the current study Au was used as the emitter material and Pt as substrate. The work function of bulk Pt is reported to be above 5.7 eV [69], and the work function of bulk Au around 5.1 eV [69]. While none of these energies is below the photon energy of a 266 nm laser beam, which is the lowest laser wavelength (highest photon energy) available for this experiment, multiple measurements [8, 59, 67] proved that 20-30 nm thick Au layers emit electrons via photoemission at this wavelength. This is to conclude that the work function of such thin metallic layers is significantly lower than the values reported for bulk. If this argument is true, there should be a configuration, some given thicknesses for the Au and the Pt layers, at which the work function of Au is below 4.66 eV, which corresponds to the photon energy of the 266 nm laser wavelength, and the work function of Pt is above this value. Such a configuration will make possible the fabrication of a working electron source featuring the proposed patterned structure.

It is still not fully understood how the work function changes with the thickness of the metallic layer, or if the work function variation is really due to the layer thickness or due to other factors like surface contamination. The work function of the substrate on which the metal is evaporated could also play a role, given the thin layers implied here (between 20 and 100 nm). In these conditions, the electron emission in the presence of the laser excitation could, to some extent, be originated in both, the thin metal layer as well as the substrate. Therefore, the effective work function ϕ_{eff} of the structure could appear to be a combination of the work functions of the two materials. Along these lines, an investigation of the emission current as a function of the thickness of the emission material was attempted.

Photoemission measurements were performed on the *E-gun 300* setup, presented in section 3.3, on flat Pt photocathodes with different thicknesses. Thin Pt layers of 15, 30, 60 and 100 nm respectively were evaporated on top of 99.999% pure bulk Mo discs. The discs were 25 mm in diameter and 3 mm thick and a 6 nm Ti layer was used as adhesive between the Mo and the Pt. All depositions were performed at the same deposition rate of $1 \AA/s$. To trigger photoemission, a 100 fs pulsed UV (266 nm) laser source was used, at a repetition rate of 1 kHz. Figure 4.1 (a) and (b) plots the results obtained for the 15 and the 30 nm thick samples. The measurements were performed at an acceleration voltage of 80 kV, and the triggering average laser power on the photocathode was varied form 0 to 700 μW. The results show a maximum average emission current of 1.3 nA for the 15 nm thick layer and an average current of 2.2 nA for the 30 nm thick layer (4.1 (a)). These values correspond to a QE of $1.37 \cdot 10^{-5}$ for the 15 nm case and $2.35 \cdot 10^{-5}$ for the 30 nm

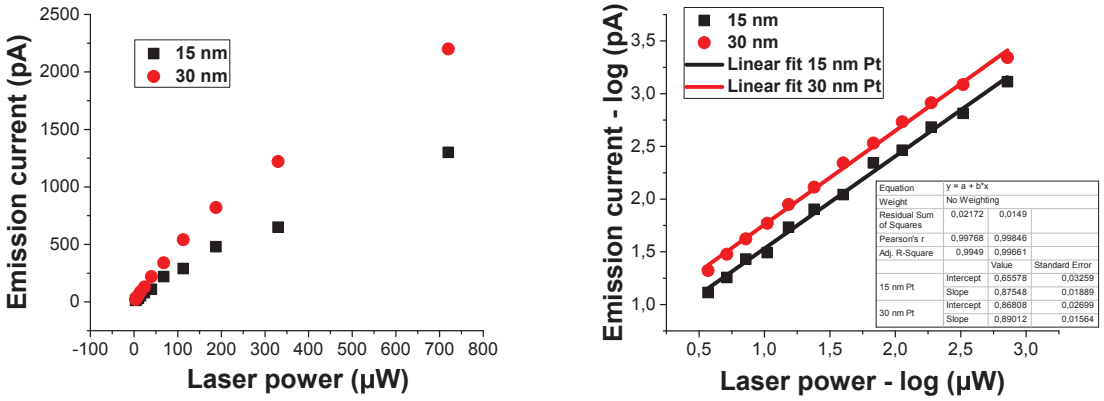

(a) (b)

Figure 4.1.: Photoemission results from a 15 nm and a 30 nm thick Pt sample, deposited on a bulk Mo substrate, a 6 nm adhesive Ti layer being added in between. (a) Emission current as a function of the incident laser power and (b) the log-log representation of the same data (red dots and black squares respectively) and linear fits (red and black lines)

one. Also, in figure 4.1 (b) a linear fit of the log-log dependency is shown, which reveals a slope very close to 1, suggesting single-photon photoemission as the predominant emission mechanism.

Figure 4.1 suggests a larger QE for the thicker layer which seems to contradict the assumption that the work function decreases with the layer thickness, which should in turn lead to a larger QE for the thinner layer. This result could be intuitively explained by considering the fraction of the incident light that is absorbed within each of the two layers. Assuming the same surface quality, at the given 266 nm laser wavelength, only 73% of the incident light will be absorbed within the 15 nm thick layer as opposed to 93% within the 30 nm thick Pt layer. This is to say that more electrons are expected to be excited from the 30 nm thick Pt layer. Unfortunately, results on thicker Pt layers, above 30 nm, could not be obtained. This was because the thicker photocathodes could not sustain the 80 kV acceleration voltage, a severe stripping off and damage of the Pt layer being observed. Thus, further measurements to confirm this hypothesis could not be performed in the same conditions.

Alternatively, some additional measurements on Mo/Pt/Au sandwich structures were performed by our colleague Sven Lederer from Deutsche Elecktronen Synchrotron (DESY), in a low acceleration field environment. Here no sample damage was encountered. The QE of two 50 nm thick Au layers, one deposited on a 50 nm and one on a 100 nm thick Pt layer (coated on similar bulk Mo substrates) was investigated. For these samples, the diameter of the Au coating was 4 mm and the Pt layer was coated over the whole surface of the Mo substrate which was this time around 16 mm. The results from the figure 4.2,

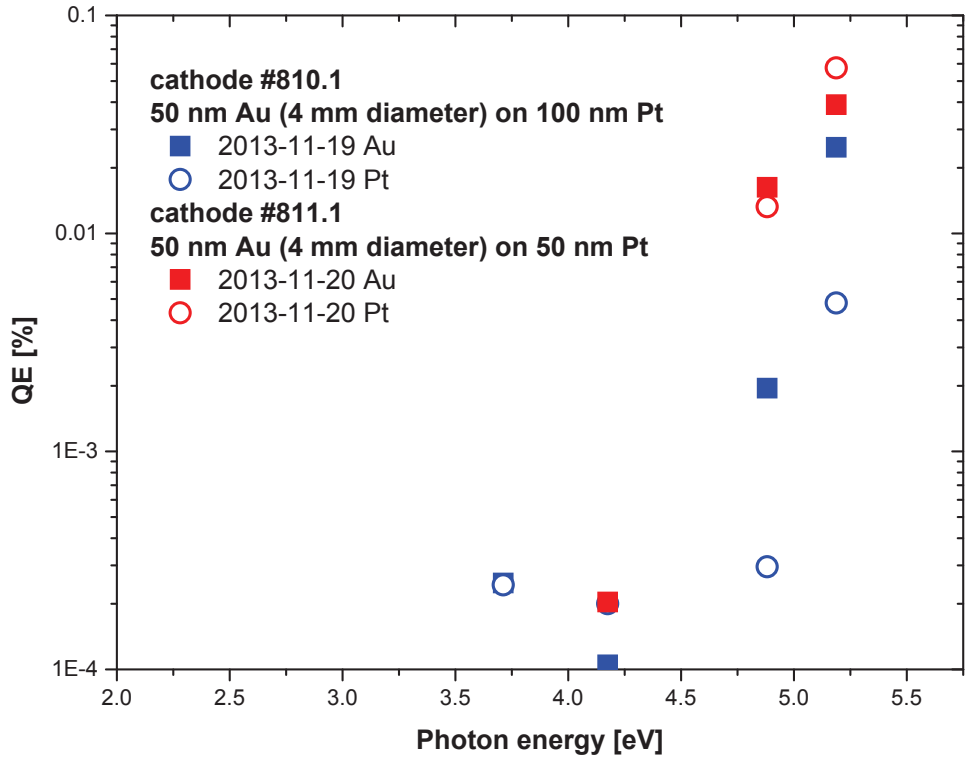

Figure 4.2.: QE results on two 4 mm in diameter, 50 nm thick Au layers, deposited on a 100 nm Pt layer (cathode number 810.1), and on a 50 nm Pt layer (cathode number 811.1) respectively. These measurements as well as the plot were made by Sven Lederer from DESY

show a QE of the Au layer which is 6.6 times larger than the QE of the Pt substrate.

Even if the results so far proved a rather good contrast, further investigations in this direction are needed. Nevertheless, a first conclusion is that the electron emission of thin metallic films (less than 100 nm) is first of all influenced by the fraction of the incident light that is absorbed within the material. This is of course depending on the thickness and, at the given 266 nm laser wavelength, will be more than 90% for thicknesses above 30 nm [70]. On the other hand, the reason for the lower work function of thin layers, as compared to bulk, still remains unclear. Intuitively, the author considers that this is originated in surface contaminations due to air exposure, which are more significant in the case of thin metallic layers.

As further measurements could not be performed, some more time was invested in the fabrication of small area Au structures on top of Pt substrates. Eventually, after experimenting with different apertures used as a mask in the deposition process, a 50 μm in diameter, 50 nm thick Au dot was coated on a 100 nm thick Pt substrate. A sketch as well as a microscope image of the structure are shown in figure 4.3 (a) and (b). Unfortunately, up-to-date no measurements could be performed on this sample either, this being part of the future plans.

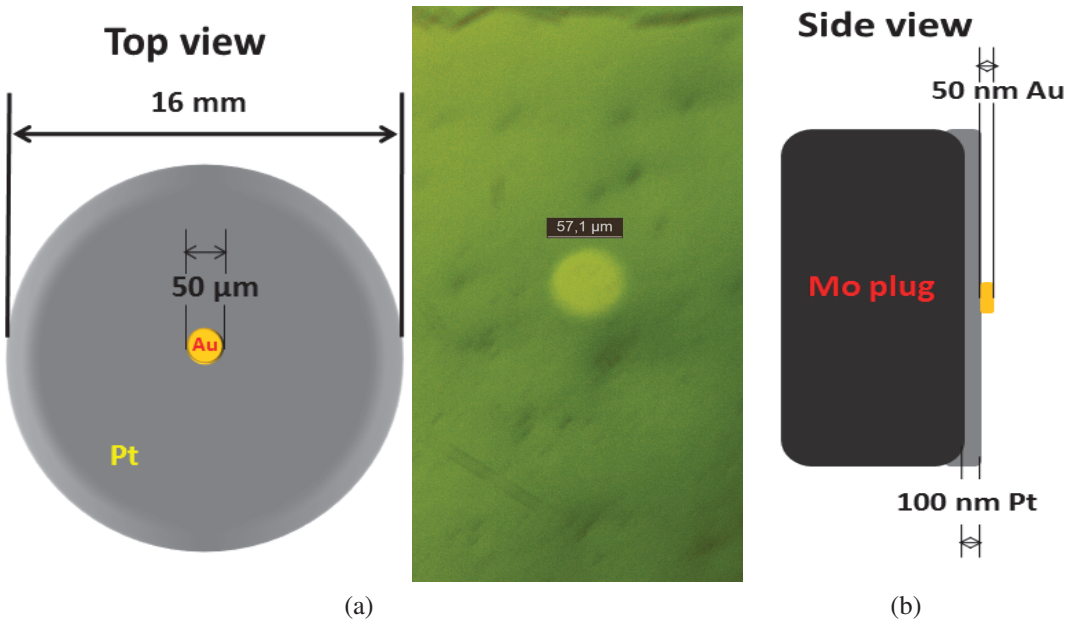

(a) (b)

Figure 4.3.: (a) Sketch of a 50 μm in diameter and 50 nm thick Au dot, coated on a 100 nm thick Pt layer (view from above) and, on the right, a real image taken with an optical microscope; (b) Sketch of the same structure viewed from the side

4.2. Characterization of flat Mo photocathodes

As it was reminded in the introduction of this thesis, and in the theory chapter (chapter 2), two of the most relevant properties used to describe the performances of an electron source are the intrinsic, or the thermal emittance (TE) and the quantum efficiency (QE). Important efforts have been dedicated to the theoretical and experimental study of the dependence of these two properties on various factors but especially on the wavelength of the triggering laser [46, 48, 49, 51–54, 66, 71, 72]. The main outcome of these is that QE and TE are interconnected and directly related to the excess energy of the photoexcited electrons with respect to the material work function ϕ. By tuning the laser wavelength to match the metal work function, the excess energy is reduced as well as the maximum possible transverse momentum of electrons, after their escape into vacuum (section 2.3). This leads to a decrease of both, TE and QE. While the first is a desired effect, the last will narrow the possible applications on irreversible dynamics studies due to the reduced bunch charges. Therefore, a middle solution is generally searched for, and a better understanding of what are the experimental conditions that have an effect on these two electron source properties is required.

While the effect of the laser wavelength on the QE and TE for metal electron sources is well understood, little reference was made so far to the excess energy changes due to the work function variation induced by high electric fields present at the cathode surface [73]. In most experimental configurations, the wavelength of the triggering laser is constant,

while the extraction electric field could be easily varied over a wide range. The development of RF electron guns made possible the application of more than 100 $\frac{MV}{m}$ [10, 74, 75] electric fields at the photocathode surface, before electric breakdown, which pushes the use of metallic photocathodes to yet unknown terrain. This is why the author considers that a study of the QE and TE variation as a function of the surface electric field is valuable. On the other hand, the TE for a given cathode material can be decreased by reducing the laser spot size on the cathode. This will of course be accompanied by a growth of the laser fluence required for producing the same emission current. Along these lines, it has to one be better understood where the transition from single-photon to multi-photon photoemission occurs, especially for metals with low QE like Mo, and in the case of short laser pulses (on the order of femtoseconds). Above the transition point, the electron emission will be characterized by multiple photon excitations of the same electron, which will result in a critical increase of the excess energy of the excited electrons, as well as of the TE.

In this section, the above mentioned aspects are experimentally investigated for a flat bulk Molybdenum (Mo) photocathode. Also, the compatibility between the experimental results and the theoretical predictions given by the three-step-model for photoemission (TSMP), described in section 2.3, is discussed.

4.2.1. QE and TE measurements

QE and TE measurements were performed as a function of the acceleration electric field within a range from 2 MV/m to 8 MV/m. The experiment is based on direct charge measurements using a Faraday cup, for QE determination, and TE measurements using the solenoid scan technique (section 2.4.1). For these measurements, the *E-gun 300* setup described in section 3.3 was used, with the exact configuration shown in figure 4.4. The base pressure in the gun section was on the order of 10^{-8} mbar and around 10^{-7} mbar in the detection section. The photocathodes consist of a 99.999 % pure bulk Mo disc which is 25 mm in diameter and 3 mm thick, similar to those used before in section 4.1. The disks were hand polished using 3 μm grit polishing sheets and were placed 10 mm away from the anode plate, inside the vacuum chamber. A voltage difference of up to 90 kV could be applied between anode and cathode and the electron beam passes through a 1 cm aperture situated on the center of the anode plate, before entering into the detection section. About 10 cm downstream from the anode, a magnetic lens is used to focus the electron beam either on the Faraday cup, where the average beam current could be measured, or on the detector screen situated 48 cm away from the solenoid. All other relevant material properties and notations used for this experiment are given in table 4.1.

Photoemission was triggered here using a 266 nm laser beam with 100 fs FWHM

Table II: Relevant values and material properties of Mo used for the experiment

Notation	Definition	Value
E_{ph}	Photon energy	4.66 eV
F_c	Effective surface electric field	$2 \div 8$ MV/m
ϕ	Work function of bulk Mo	4.6 eV
k	Imaginary part of the refractive index	3.82
l_{s-s}	Distance from the solenoid to the screen	0.484 m
l_{a-s}	Distance from the anode to the screen	0.112 m
l_{c-a}	Distance from the photocathode to the anode	0.1 m
λ	Laser wavelength	266 nm
λ_{opt}	Optical penetration depth	5.54 nm
R	Optical reflectivity at 266 nm	0.4

Table 4.1.: Relevant values and material properties of Mo used for the experiment

long pulses, at a repetition rate of 1 KHz. The triggering laser beam enters the vacuum chamber through a 90% transmitting view port and is passing through the anode aperture before reaching the photocathode surface.

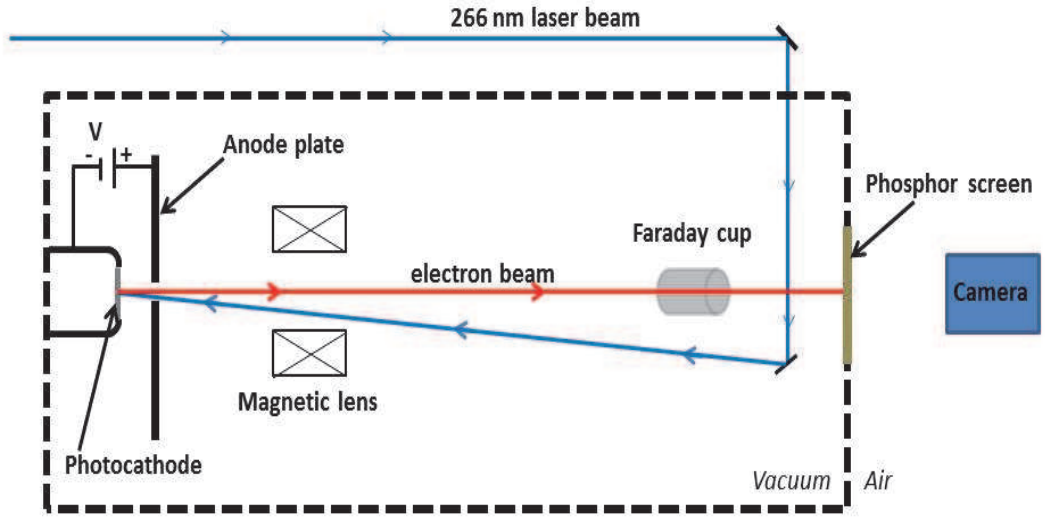

Figure 4.4.: Experimental configuration showing the main elements of the setup, the triggering laser beam path (blue) and the electron beam path from cathode to the detection screen (red)

An Al coated mirror placed near the detection screen is used to re-direct the laser beam onto the emitter, as depicted in Figure 4.4. The laser beam profile on the photocathode, shown in Figure 4.5, suggests a spot size at the photocathode position of about 39.2 μm RMS. This was measured after the experiment, by placing a small CCD camera at the cathode position and recording beam images. For imaging the electron beam,

a phosphor screen and a camera[1] was used. The phosphor screen was attached to the chamber flange without using a special vacuum flange. Only a O-ring was used and the pressure difference created while pumping down was enough to fix the phosphor screen on to the vacuum flange, a base pressure on the order of 10^{-8} mbar being achieved.

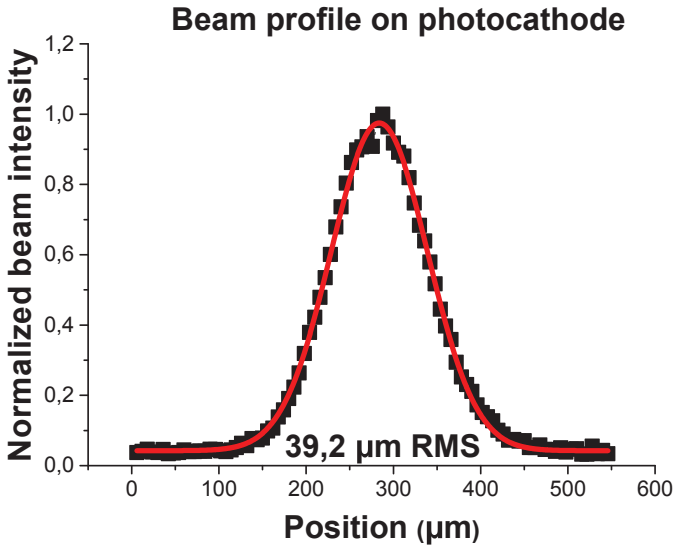

Figure 4.5.: The UV laser beam profile at the photocathode

A first result to be pointed out here is the conditioning of the photocathode by the UV laser. This is in agreement with previously reported measurements [66] and seems to be present especially in DC guns as opposed to RF configurations where an alteration of the emission current is usually encountered over time. Initially, a QE as low as $5 \cdot 10^{-7}$ was measured, which is untypical in the given conditions, but a clear increase was observed when applying the UV laser trigger for a few hours. This could be explained by a cleaning of the cathode surface by the laser beam, which removes impurities or oxidation that might have contaminated the cathode (due to the air exposure), before it was inserted inside the vacuum chamber. At an electric field of 8 MV/m, the QE increased up to $2 \cdot 10^{-6}$ at a laser power of $23\,\mu W$ applied on the photocathode surface for 4-5 hours. After this period of time, the emission current stabilized and was also reproducible when switching the laser excitation on and off. A quantum efficiency on this order is typical for *Mo* photocatodes and is in very good agreement with previously reported values [54, 66, 72]. This corresponds to a number of $6 \cdot 10^4$ emitted electrons per bunch, at an average laser intensity of $2.14\,\frac{GW}{cm^2}$ and a repetition rate of 1 kHz. After the cathode was kept inside the vacuum chamber for a few days, and conditioned, the influence of the surface electric field on the QE was investigated.

From the theoretical point of view, using equation 4.1 a work function reduction of only 54 meV is expected in the given field range. The reason for this reduction is

[1] optically coupled Andor camera, 27 by $27\,\mu m^2$ pixel size

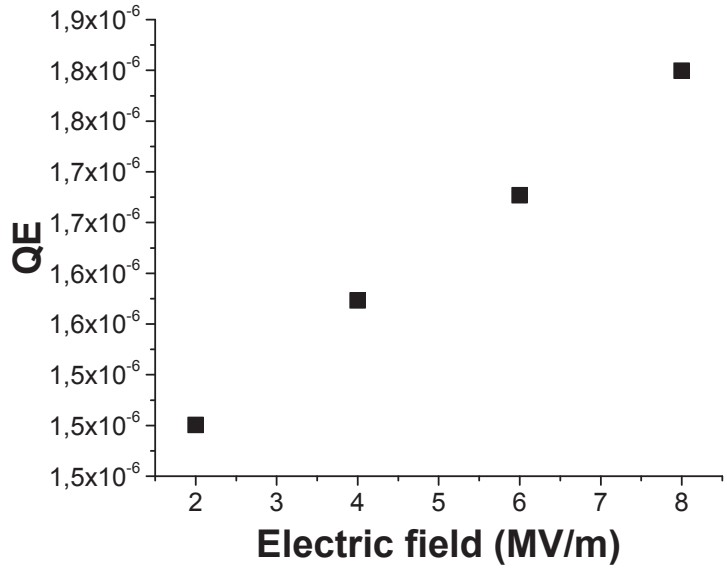

Figure 4.6.: Measured QE of the Mo photocathode as a function of the surface electric field

the change of the metal work function under the influence of the electric field. This was discussed in section 2.1.2 and the work function reduction is given by equation 4.1. While this reduction is rather insignificant, the results suggested a QE increase of 19%, from $1.5 \cdot 10^{-6}$ at 2 MV/m to $1.85 \cdot 10^{-6}$ at 8 MV/m, as shown in figure 4.6. This large effect is mainly due to the minute difference between the used photon energy, which is 4.66 eV, and the work function of bulk Mo, which is reported to be about 4.6 eV [69, 72, 76].

$$\phi_{Schottky} = e \cdot \sqrt{\frac{e \cdot F_a}{4 \cdot \pi \cdot \varepsilon}} \tag{4.1}$$

TE dependency on the surface electric field was also measured by the means of the solenoid scan technique [55, 56, 72]. The RMS electron beam size on the screen, as a function of the electric current through the solenoid was recorded for four different acceleration voltages applied between the cathode and the anode. The solenoid magnetic field was varied so that the electron beam goes through the focus at the screen position, and for each current value 2 to 4 images were recorded. The scan was repeated voltages of 20, 40, 60 and 80 KV respectively, and for each case background images were recorded. All images were saved in the *.tif format, with a size of 2047 by 2047 pixels, where every pixel contains information about the number of electrons at its position (counts) and the image analysis was done subsequently using Matlab. First, an average was made out of all pictures taken at the same solenoid current, and then from each of these, the averaged background was subtracted. Next, the pixels for each resultant image, which are basically distributed in a m by n matrix, were alternately summed on each of the two coordinates (column and row wise) and a linear Gaussian fit was performed in each case. The fit

result gave information about the center of the beam on the two directions and, at the same time, the standard deviation σ of the distribution. While this could already be used as a final result, in order to be more accurate, a second fit using a 2D Gaussian equation (4.2) was performed. In equation 4.2, the results of the one dimensional fits performed previously were used as initial parameters. Thus, X_0 and Y_0 are the beam centers on the X and the Y direction respectively, A is the amplitude of the distribution, S is the signal (pixel intensity) and σ_x and σ_y are the standard deviations of the distribution along each of the two coordinates.

$$S = A \cdot e^{\frac{-(X-X_0)^2}{2\cdot\sigma_x^2}} \cdot e^{\frac{-(Y-Y_0)^2}{2\cdot\sigma_y^2}} \tag{4.2}$$

In case of a Gaussian distribution, the standard deviations σ_x and σ_y resultant from the two dimensional fit could already be used instead of the RMS size of the electron beam. Still, in order to make the Matlab code more general and applicable also for other distributions, apart from Gaussian, the RMS value was calculated as well for each aperture position using the equation discussed before in section 2.2. Moreover, because the RMS calculation is normally very sensitive to noise, a very well defined region of interest is recommended. Here, this was defined using the beam center and standard deviation results from the two dimensional fit. Thus, for the RMS calculation, the region of interest was set to $+/-4\cdot\sigma$ with respect to the center of the distribution. This method was used to analyze all experimental data (images) implied in the content of this thesis.

In order to derive the electron beam emittance using the solenoid scan technique, the dependency of the electron squared RMS beam size at the screen x_{rms}^2, on the solenoid current, was fit by an equation that describes the beam line used for the experiment: the envelope equation. As it was presented in section 2.4.1, the fit equation without space charge has the form:

$$x_{rms}^2 = a\cdot C_{11}^2 + 2\cdot b\cdot C_{11}\cdot C_{12} + c\cdot C_{12}^2 \tag{4.3}$$

or in the matrix notation:

$$x_{rms}^2 = \begin{pmatrix} C_{11}^2 & 2\cdot C_{11}\cdot C_{112} & C_{12}^2 \end{pmatrix} \begin{pmatrix} a \\ b \\ c \end{pmatrix}$$

with $a = x_{0,rms}^2$, $b = x_{0,rms}\cdot x'_{0,rms}$ and $c = \frac{\varepsilon_{rms}^2}{x_{0,rms}^2} + x'^2_{0,rms}$

As explained in section 2.4.1, the forms that C_{11} and C_{12} take are dependent on the number of the elements composing the beam line. In the current study, the solenoid scan fit (section 2.4.1) was perform for two different forms of C_{11} and C_{12}. This was done

to verify if the method was applied correctly, and the transfer matrices were calculated accurately. If this was the case, both cases should give the same result, being based on the same set of experimental data (the RMS beam size on the screen). In the first case, only the transfer matrix of the solenoid and the drift length from the solenoid to the screen were considered. In the second case, the transfer matrix of the anode aperture was also added, which could be seen as a magnetic lens, and the drift region between the anode plate and the solenoid was also considered. It has to be again stressed here that no extra information are gained by also including the transfer matrix of the anode plate. The results cannot be used to verify if the beam emittance at the anode is different than at the solenoid because the same set of experimental data is used, and the calculation is based on the thin lens approximation (which implies that the lenses do not change the emittance of the beam). Thus, this was only done to verify if the fit method was applied correctly and, as mentioned above, the same result was expected for the two different cases. In the first case, the transfer matrix from the solenoid to the screen $M_{Tr_{S-S}}$ was calculated taking into account only the solenoid matrix $M_{Tr_{Sol}}$ and the drift over the distance l_{s-s}=0.484 m from the solenoid to the screen. In this case, C_{11} and C_{12} are:

$$C_{11} = C_{11_{S-S}} = 1 - \frac{l_{s-s}}{f} \text{ and } C_{12} = C_{12_{S-S}} = l_{s-s} \tag{4.4}$$

In the thin lens approximation, the inverse focal length of the solenoid, $1/f$ is calculated using:

$$\frac{1}{f} = \frac{e^2}{4 \cdot p_z^2} \cdot \int_{-\infty}^{\infty} B(z)^2 dz = \frac{e^2}{4 \cdot p_z^2} \cdot F_2 \tag{4.5}$$

As expected, the focal length of the solenoid depends upon the magnetic field B. During the experiment, this was controlled by changing the electric current flowing through the solenoid thus, a relation between the electric current I and the magnetic field B was used. This relation can only be found if a calibration of the solenoid is available. In this case, the solenoid was calibrated by Hossein Delsim-Hashemi and therefore this data was available. This calibration consists of magnetic field measurements along the axis that passes through the center of the solenoid (from z=−50 mm to z=50 mm) with respect to the solenoid plane), performed at different values of the electric current through the solenoid: 200, 250, 300, 350 and 400 mA. To find the desired dependency, the second field integral $F_2 = \int_{-\infty}^{\infty} B(z)^2 dz$ was calculated, and the result is plotted against the electric current through the solenoid as shown in figure 4.7. The intercept and the slope of a linear fit to this data give the relation between I and B, as shown in equation 4.6.

$$B^2 = 1.85 \cdot 10^{-7} + 2.13 \cdot 10^{-4} \cdot I^2 \tag{4.6}$$

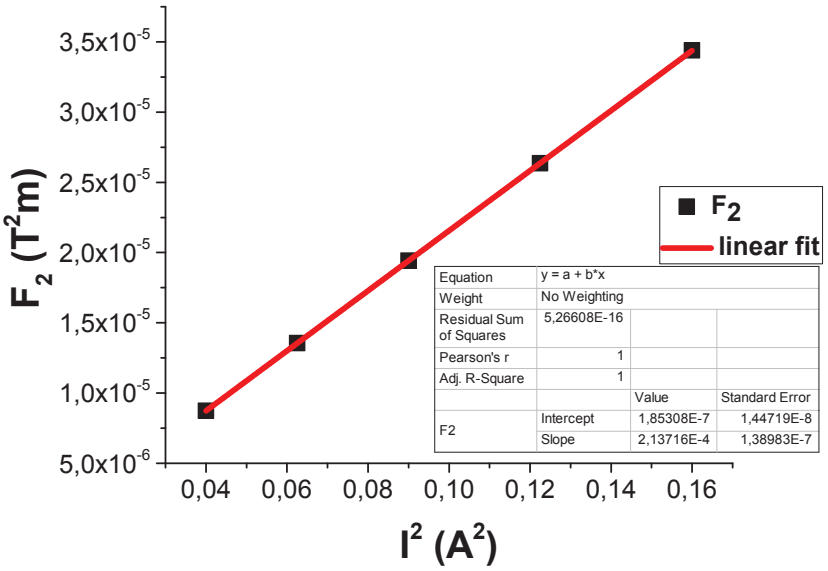

Figure 4.7.: The second field integral F_2 as a function of the electric current through the solenoid (black squares) and a linear fit (red line)

In the second case, besides the magnetic lens, the anode plate which acts as an electric lens was also taken into consideration. Its focal length f_a, is given by equation 4.7 as shown in references [57] and [58] and was also described in section 2.4.2. Here, V is the potential difference between the anode and cathode (or the electron beam energy) and E_1 and E_2 are the electric fields before and after the anode plate respectively. Here, $E_2 = 0$ and to calculate E_1, the distance between the anode and the cathode $l_{c-a} = 10\,\text{mm}$ was used.

$$f_a = \frac{4 \cdot V}{E_2 - E_1} \tag{4.7}$$

Also, for calculating the new transfer matrix $M_{Tr_{A-S-S}}$, one more drift region between the anode plate and solenoid has to be taken into account. This is l_{a-s}=0.112 m. The coefficients C_{11} and C_{12} will now become:

$$C_{11} = C_{11_{A-S-S}} = 1 - \frac{l_{s-s}}{f} - \frac{1}{f_a} \cdot \left[l_{a-s} \cdot \left(1 - \frac{l_{s-s}}{f} \right) + l_{s-s} \right] \tag{4.8}$$

and

$$C_{12} = C_{12_{A-S-S}} = l_{s-s} + l_{a-s} \cdot \left(1 - \frac{l_{s-s}}{f} \right) \tag{4.9}$$

Figure 4.8 (b), (c), (d) and (e) shows the solenoid scan fits for the first case (at the solenoid position) at each of the four different voltages. This figure is meant to show that the fit works very well. Figure 4.8 (a) depicts again the experimental configuration including the distances between the beam-line elements.

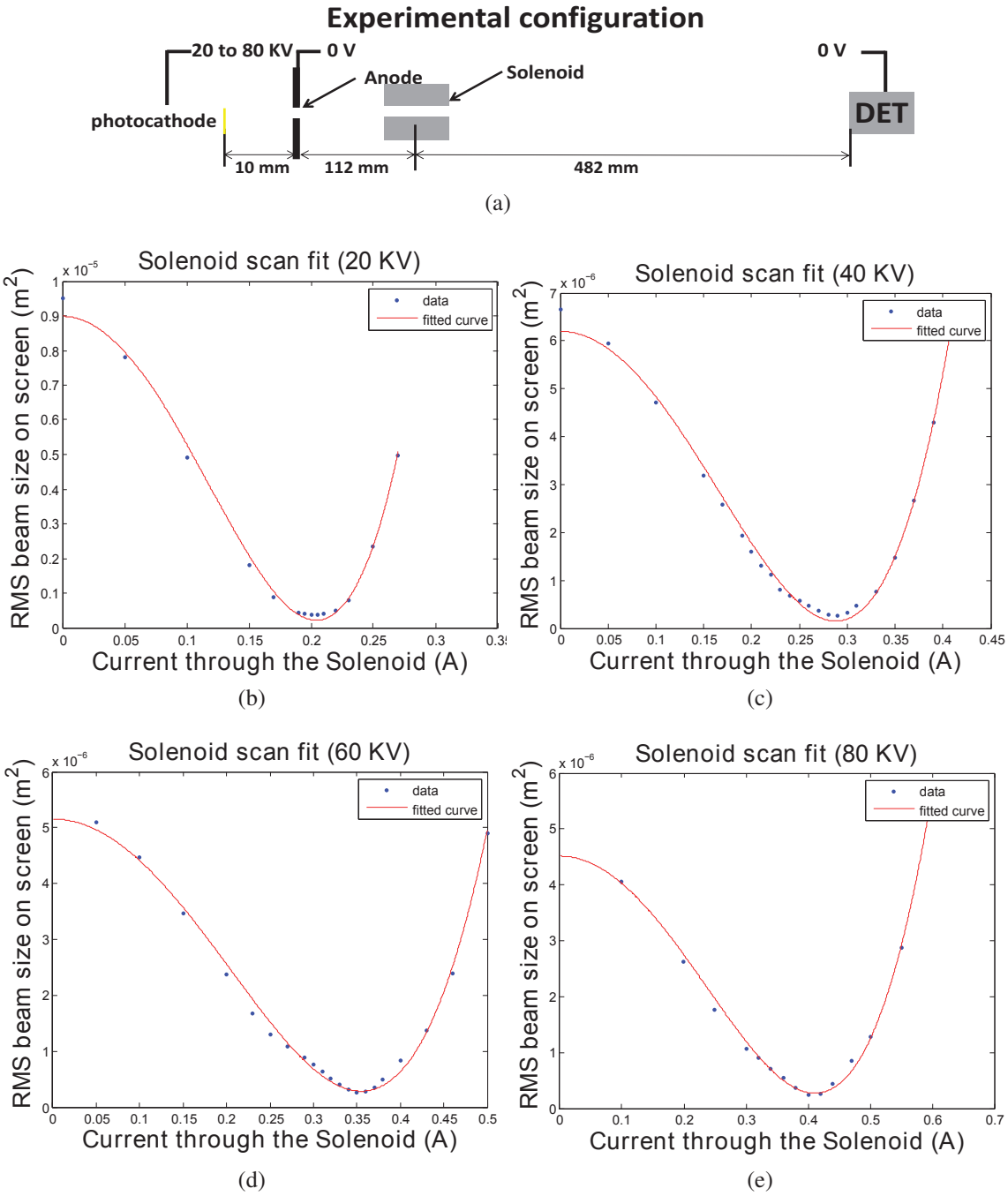

Figure 4.8.: (a) Experimental configuration; (b) The RMS beam size at the screen as a function of the electric current through the solenoid (blue dots) and the fit (red line) with the envelope equation, including only the solenoid and the drift to the screen, at 20kV, (c) 40 kV, (d) 60kV and (e) 80kV

The emittance results are shown in figure 4.9, where the normalized emittance $\varepsilon_{n,rms}$ was obtained by multiplying the geometric emittance ε_{rms} with $\frac{p_{rel}}{m \cdot c}$. Here the momentum p_{rel} takes the relativistic form given by the equation 4.10, as discussed in section 2.2.2.

$$p_{rel} = \sqrt{\frac{(e \cdot V + m \cdot c^2)^2 - m^2 \cdot c^4}{c^2}} \tag{4.10}$$

As it was expected, the normalized emittance is increasing with the electric field. This is because of the excess energy increase of the electrons as a result of the Schottky work function reduction. Figure 4.9 depicts the variation of the normalized beam emittance $\varepsilon_{n,rms}$, along the two coordinates perpendicular to the direction of propagation at the solenoid position. No noticeable difference between the inferred emittance at the two positions was found (at the anode and at the solenoid), which is proof that the fit method was correctly applied and the transfer matrices were accurately obtained in both cases.

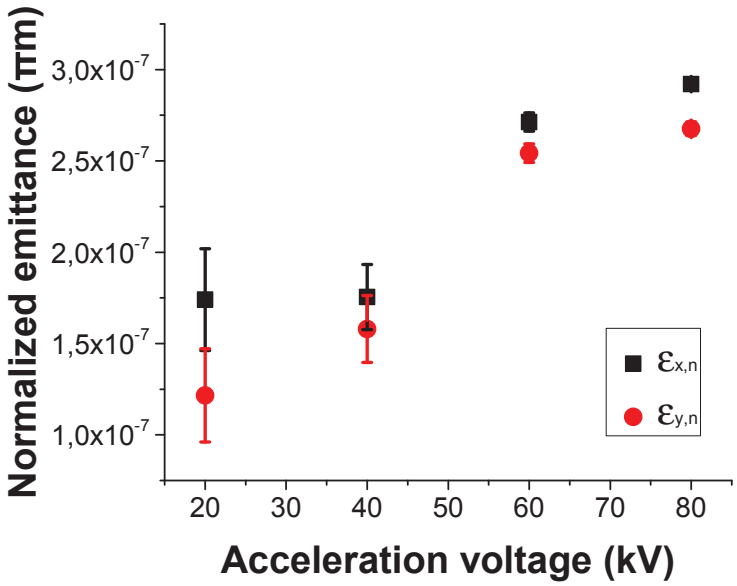

Figure 4.9.: Normalized emittance on the two directions (X and Y) as a function of the acceleration voltage at the solenoid position

An emittance increase of 40% percent along the X coordinate and 55% along the Y coordinate was found. This is a significant variation given the minute expected reduction of the Mo work function, of only 54 meV. Another unexpected result was the relative large value of the normalized emittance, found to be between 100 and 300 πnm. These values are similar to previously reported experimental results [48, 72, 77, 78] but these were obtained for significantly larger emission areas (on the order of millimeters) than in the current case. Global Particle Tracking (GPT) simulations showed that space-charge effects are not significant in these experimental conditions, therefore they cannot be used as a justification for this experimental outcome. In order to explain this mismatch, a theoretical debate and more experimental investigations were made as it will be discussed in

the following section.

4.2.2. Theoretical follow-up

From a theoretical point of view, the QE and the TE of metal electron sources can be calculated using the three-step-model for photoemission (TSMP) described in section 2.3. Two relatively simple formulas were obtained for calculating QE, equation 4.11, and TE, equation 4.12 [46, 48].

$$QE \approx \frac{(1-R)\cdot(E_{ph}-\phi_{eff})^2}{8\cdot\phi_{eff}\cdot\left(1+\frac{\lambda_{opt}}{\lambda_{e-e}}\right)\cdot(E_F+\phi_{eff})} \tag{4.11}$$

$$\varepsilon_n = \sigma_x\cdot\sigma_{p_x} = \sigma_x\cdot\sqrt{\frac{E_{ph}-\phi_{eff}}{3\cdot m\cdot c^2}} \tag{4.12}$$

As it can be observed, the two equations are based on material properties, laser photon energy and experimental conditions (electric field). While the experimental conditions and the triggering laser wavelength are usually very well known, regarding the material properties sometimes there is a lack of information, or reported values in literature are not consistent. The relevant properties for QE and TE calculation are the material work function ϕ, the electron-electron scattering length λ_{e-e}, the Fermi energy E_F and the imaginary part of the refractive index k, which is needed to calculate the optical penetration depth $\lambda_{opt} = \frac{\lambda}{4\cdot\pi\cdot k}$. All of these are depending on the material purity, structure and lattice quality, as well as on the surface roughness which make them nearly impossible to calculate precisely.

For the QE calculation, the electron-electron scattering length λ_{e-e}, fermi level and the imaginary part of the refractive index k are needed, as shown in equation 4.11. This makes QE prediction a bit challenging, especially because of the lack of information about the electron-electron scattering length λ_{e-e}. While this could in principle be calculated [46, 48, 52], it is not trivial and the calculation is based on a number of simplifying assumptions about the surface and lattice quality of the metal. Therefore, using the TSMP to predict the QE of the Mo photocathode in the present situation is not contingent. Alternatively, a deduction of ϕ and λ_{e-e} is possible by fitting the experimental data, the QE measurements in our case, using equation 4.11. Of course, for this to give accurate results a large number of experimental point is desired. Here, only four values were available (one at each acceleration voltage).

On the other hand, for TE calculation the only material property required is the effective work function ϕ_{eff}. The TSMP equation 4.12 was therefore used here to predict the influence of the surface electric field on the TE. A work function of 4.6 eV was

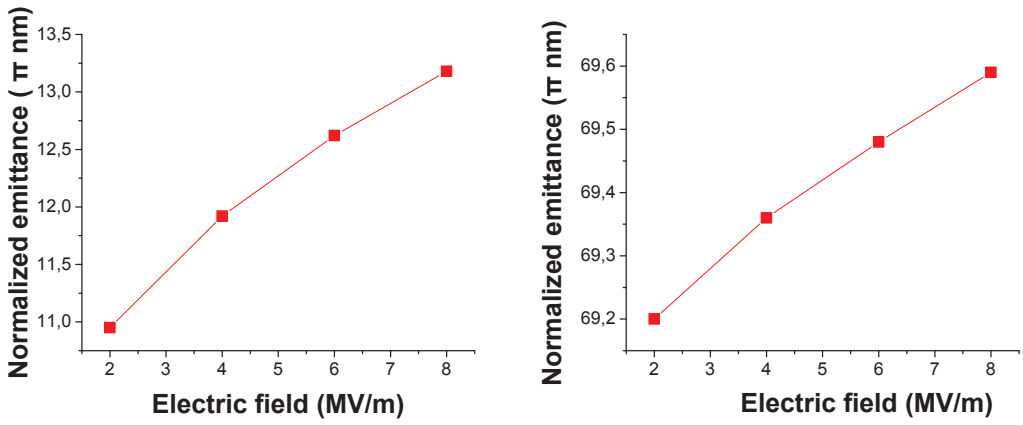

Figure 4.10.: (a) Normalized emittance prediction using the TSMP (equation 4.12), as a function of the acceleration electric field, and assuming a work function of $\phi = 4.6eV$. (b) Same as (a) but assuming a 2PPE process and therefore a photon energy of 9.32 eV instead of 4.66 eV as in case of single-photon photoemission

assumed for the bulk Mo photocathode [69, 76] and the electron beam size at the photocathode was taken to be equal to the measured RMS laser spot size of $39.2\,\mu m$. As it is shown in figure 4.10 (a), an emittance increase of only 17% is theoretically expected in the given electric field range. Also, the absolute value of the theoretically predicted normalized emittance, at an acceleration voltage of 2 MV/m, is eleven times smaller then what was experimentally observed here.

A mismatch between the TE experimental results and the theoretical prediction using the TSMP was, to some extent, expected due to the fact that the theory does not include any effects of the work function variation due to the energetic band structure of the metal [54], or due to the surface roughness [79]. Previous measurements have shown that the TSMP gives an optimistic estimate and measurements typically give a normalized emittance value two times larger [77, 78]. Nevertheless, this alone could not explain the one order of magnitude larger normalized emittance measured here and plotted in figure 4.9. Instead, the author acknowledges that this could in fact be an effect of the surface roughness [79] or of electron emission due to multiple-photon absorption events, which are possible at these short pulse durations [71, 80, 81]. Figure 4.10 (b) shows the theoretical emittance prediction using equation 4.12, but assuming a two-photon photoemission process. This was accounted for by using a double photon energy $E_{ph} = 9.32eV$. In this case, the theoretically predicted emittance will be more than six times larger than in the one-photon photoemission case. This new value is now in much better agreement with previously reported observations [48, 72, 77, 78], being in this case two times lower than the measured values reported in the current experiment. In order to experimentally verify this hypothesis (the presence of two photon photoemission (2PPE) processes), the

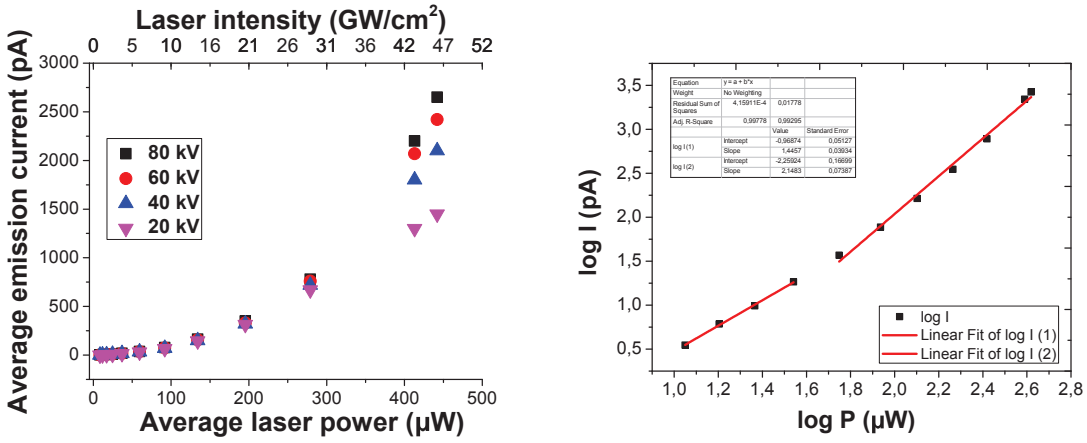

Figure 4.11.: (a) Average emission current as a function of the laser power for each of the four acceleration voltages: 20, 40, 60 and 80 kV respectively; (b) Emission current as a function of the laser power for a surface electric field of 8 MV/m. Both axes are logarithmic and two linear fits have been performed trying to point out the two different regimes: single and two-photon photoemission

electron emission current was measured as a function of the incident laser power on the photocathode surface, and the results will be presented in the next section.

4.2.3. Electron photoemission as a function of the laser intensity

For these measurements, the same experimental configuration as used for the QE measurements was kept. The electron beam was focused on the Faraday cup with the same solenoid magnet used for the TE measurements, and the average current was measured by an electrometer[2] connected to the cup. The laser power was changed outside of the vacuum using a ND filter wheel, and the spot size on the photocathode was kept the same as for the QE measurements (39.2 μm).

Figure 4.11 (a) shows the average emission current as a function of the laser power, for each of the four acceleration voltages: 20, 40, 60 and 80 kV respectively. As it can be observed, the dependency at all of the four acceleration voltages does not reassemble a straight line, suggesting that the electron emission mechanism is not exclusively due to single-photon excitation processes. It seems that a transition towards multi-photon photoemission is present, corroborating the prediction made above and supporting the large values of the TE, which were obtained experimentally. Figure 4.11 (b) depicts the emission current as a function of the laser power at 80 kV, on a log-log representation. Here, two linear fits were performed on different parts of the data set, trying to find the transition point between single, and multi-photon photoemission. As it can be seen in the inset table

[2] Keithley 6514

of figure 4.11 (b), none of the two slopes has an integer value, and therefore a clear laser power threshold is difficult to find. This could be and indication that one and two photon photoemission precesses are concomitantly present. At a laser power of $23\,\mu W$ (a laser intensity of $2.14\,\frac{GW}{cm^2}$), where the solenoid scan measurements (TE measurements) were performed, both emission processes seem to be concomitantly present. Considering that the normalized emittance is directly proportional to the maximum angle of escape that electrons have at the metal surface, as discussed in the theory chapter in section 2.3, the TE result in this case would be nearly similar to the case where two-photon processes are predominant. This is because the maximum possible transverse momentum of the emitted electrons in the current situation is still given by electrons that suffered two-photon excitations. These electrons would have a maximum excess energy of $2 \cdot E_{ph} - \phi_{eff}$. Of course, this effect could be better observed if emittance measurements at the two extremes (lowest and highest laser intensities) would be shown, but these experimental data are unfortunately not available. Moreover, the current experimental work was performed with the scope to show how does the surface electric field influence the TE and QE of flat Mo photocathodes, an exact explanation of the large emittance source being beyond the scope.

This aspect of multi-photon excitation events is very important, especially for state-of-the-art linear accelerators, like REGAE (section 3.4), where electron currents similar to those obtained in the above discussed experiment are implied. Likely, two-photon photoemission processes are unlikely present at REGAE because of the lower laser intensities, below $1\,GW/cm^2$, which is due to the longer pulse duration of the triggering laser (about 1 picosecond). Nevertheless, a similar value for the normalized emittance, about $160\,\pi nm$, was measured here on a similar flat Mo photocathode. This measurement, performed by Max Hachmann from DESY, was done at an acceleration field of 50 MV/m. As compared to the current experiment, the acceleration field at REGAE was much higher therefore a large value for the normalized emittance (in the absence of multi-photon excitation processes) was expected due to the more significant Schottky effects.

4.3. Double-gated nanoemiters

Field Emitter Arrays (FEA) promise good performances in applications like field emission displays [82] and multiple beam lithography [83, 84]. Recent fabrication ascents have made possible production of such structures featuring one or more so called "gates" which can be used to extract or to focus the electron beam [85]. By using a combination of techniques like molding, self-aligned resist etch-back method and focused ion beam milling, very good alignment between the tip and the gates can be achieved and tip radii of curvature down to 5 nm are possible [28, 86]. Due to their small emitting area, these devices promise to exhibit low electron beam emittance and high transverse coherence

lengths, which make them good candidates for next generation of free electron sources. The short distance between the emitter tip and the extraction gate, which is typically in the micrometers range, gives rise to electric fields of a few GW/m at the tip apex for extraction voltages of only 100 V. These fields significantly reduce the work function of the emitter metal due to image potential charges discussed in section 2.1.2, therefore giving the possibility to also optically trigger photo-field emission at more easily accessible laser wavelengths [87]. While a considerable amount of research has been carried out on emission properties of FEA's [28, 88–92], in which few tens of thousands of tips are enclosed on a single chip, the study of individual such emitters has been left open for investigation.

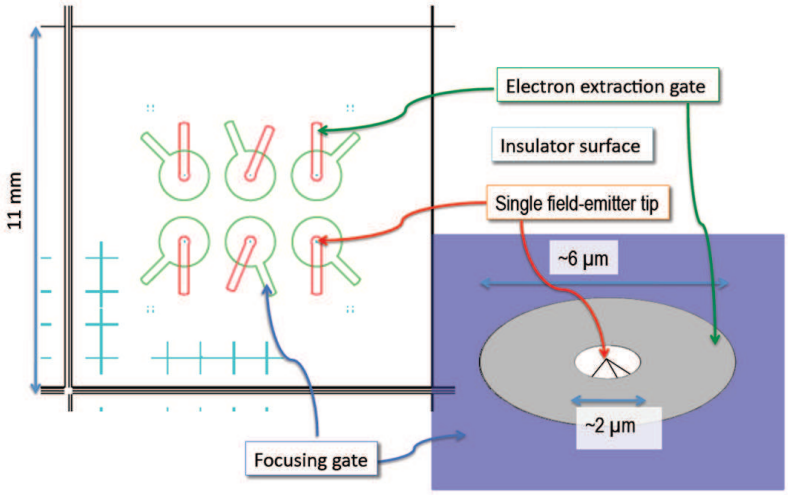

Figure 4.12.: Sketch of the chip containing six double-gated nanoemitters. The sketch, and the chip, were provided by Patrick Helfestein and Soichiro Tsujino from the Paul Scherrer Institut (PSI) in Switzerland

In the current section, a description of the setup and of the methodology used to characterize single double-gated field emitter tips is described, and some first results are presented. For these measurements, the *Test chamber* described in section 3.1 was used. The chip under observation, depicted in figure 4.12, were 10 by 10 mm^2 large and contained six double-gated Molybdenum (Mo) emitters. The chip was fabricated [86] and provided for investigation by Patrick Helfestein and Soichiro Tsujino from the Paul Scherrer Institut (PSI) in Switzerland. The tips, which were grown on a Mo substrate material, are separated by insulating layers from the two gates, also made of Mo. A SiO_2 layer is found between the tip and the extraction gate and a *SiON* layer between the two gates. For the current tips, the thickness of each of the two insulating layers was about $1.2\,\mu m$ and the gates diameters were $2\,\mu m$ for the extraction gate and $6\,\mu m$ for the collimation gate respectively. A sketch of the whole chip is presented in Figure 4.12 as provided by our collaborators.

One of the most important challenges, when it comes to the investigation of single tips is the development of an experimental setup that allows to individually bias the tips

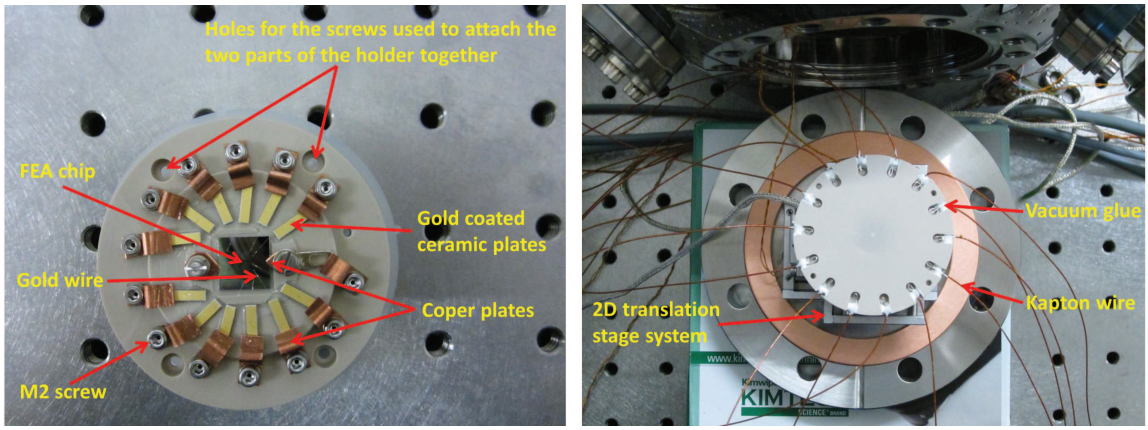

(a) (b)

Figure 4.13.: (a) Picture with the top part of the special designed chip holder (with the chip mounted) and indications of the relevant details; (b) Picture with the bottom part of the chip holder mounted on a 2D translation system (on the vacuum flange)

and corresponding gates, while at the same time allowing the selection of any particular tip for observation, without breaking vacuum. For this purpose, a custom sample holder that consists of two detachable parts was designed by the author as shown in figure 4.13 and in the appendix C. The top part is holding the chip which is pressed against the holder from the top using two $M2$ screws and copper plates. The individual gates and tips were electrically connected by our collaborators using wire bonding techniques, to some gold coated ceramic parts which were previously glued on the holder, around the chip as shown in Figure 4.13 (a). From here, the electrical conductivity is assured further through some additional ”L” shaped copper plates which are pressed against the ceramic plates using $M2$ vented screws. The tips substrate was connected by a wire placed under the chip which was then attached to one of the $M2$ screws. This way, all the gates and tips were in electrical contact with one of the $M2$ screws situated around the chip at the side of the top holder part (figure 4.13 (a)). This top part could then be easily mounted on the second part of the holder, the bottom part (Figure 4.13 (b)). Kapton insulated wires, connected to an air-vacuum multi-pin electrical feedthrough, were glued to this bottom part using a special vacuum glue. By mounting the two parts together, the $M2$ screws come in electrical contact with the Kapton wires and then each tip and gate on the chip can be accessed from outside the vacuum chamber via the multi-pin feedthrough. Therefore, the tip under observation could be changed from outside the vacuum using a commercial board where all the wires were plugged in.

The above described holder together with the chip were mounted on a two dimensional translation stage system. The 6 tips were situate about 2 mm apart, therefore they needed to be centered with the 3 mm in diameter aperture, present in the center of the anode plate, to allow the emitted electron beam to travel all the way to the MCP detec-

tor. Due to space constrains inside the vacuum chamber, the stages had to be vertically attached directly to the vacuum flange as shown in figure 4.14 and in the section C. Magnetic shielding was assured after the anode plate by a custom made mu-metal tube. Although the distance from the anode to the MCP was only about 15 cm, the mu-metal tube proved to be necessary specially because the vacuum system included a magnetic gauge. The measurements were performed as follows: the extraction gate of the tip under observation was kept grounded and the tips substrate was biased at a negative voltage. While this way all six tips were biased at the same time, emission was only possible from the tip that was aligned with the anode aperture and of which extraction gate was grounded. The collimation gates were floating during these measurements and the mu-metal tube as well as the anode plate were kept at the same voltage as the front MCP plate (up to 2 KV). The current flowing through the tip was measured using the same source measure unit[3] that was used to bias the tips. Before emission could be triggered, a standard conditioning procedure was applied for a few days as suggested by our collaborators from PSI. This procedure comprises that the extraction field at the tip is gradually increased while trying to reach a steady emission regime. More precisely, an emission current limit and a maximum voltage was set before the conditioning program is started. The voltage on the substrate was then increased slowly and the emission current was monitored. If the current limit was reached before the maximum voltage, the voltage was reduced down to an initial value (of a few tens of V) and the cycle was repeated. When a stable current-voltage curve was achieved, the maximum emission current could then be set to a larger value .

Electron emission was initially detected for a voltage on the Mo substrate of about -130 V. Only two of the six tips were functional, the others being defective (no electron emission was detected). After conditioning the working tips for more than one day, a stable emission state was reached as well as a maximum current at voltages below -100 V. Figure 4.15 (a) shows the current-voltage characteristics for the maximum achieved current of 125 nA. Unfortunately, the tip appeared to be damaged (stopped emitting electrons) after this maximum current was reached. The damage occurred due to the short conditioning process, otherwise the lifetime of the tips could extend to about two weeks.

In conclusion, the capability of the *test chamber* setup to trigger and detect field emission from single double-gated field emitter Mo tips was successfully proven, and a maximum emission current of 125 nA was measured. A more detailed analysis is needed to fully characterize these emitters but this is beyond the scope of the current Ph.D. work. The project is being continued by a new Ph.D. student of the group: Chiwon Lee.

[3] Agilent B2902A

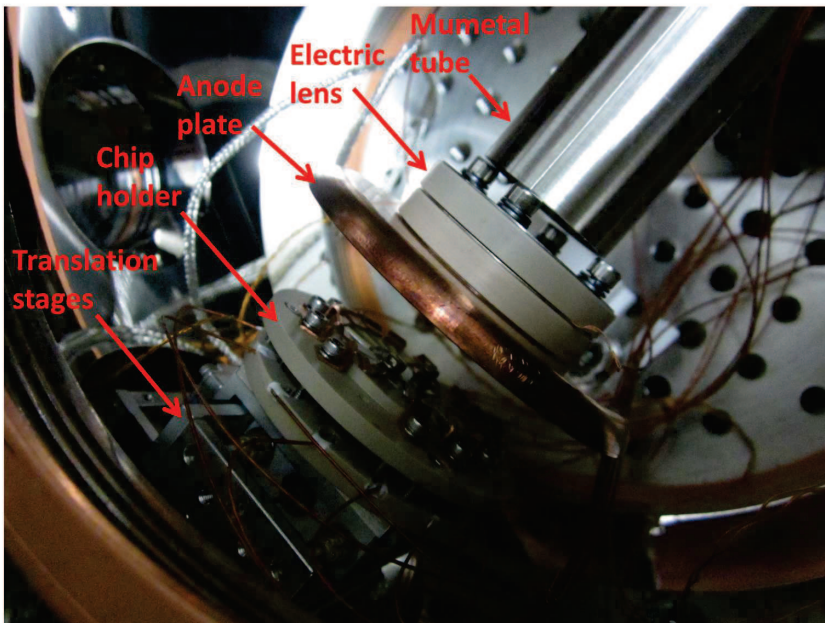

Figure 4.14.: Picture with the beam-line where the electron source (the chip with the 6 field-emitters) and the other relevant beam-line components are indicated

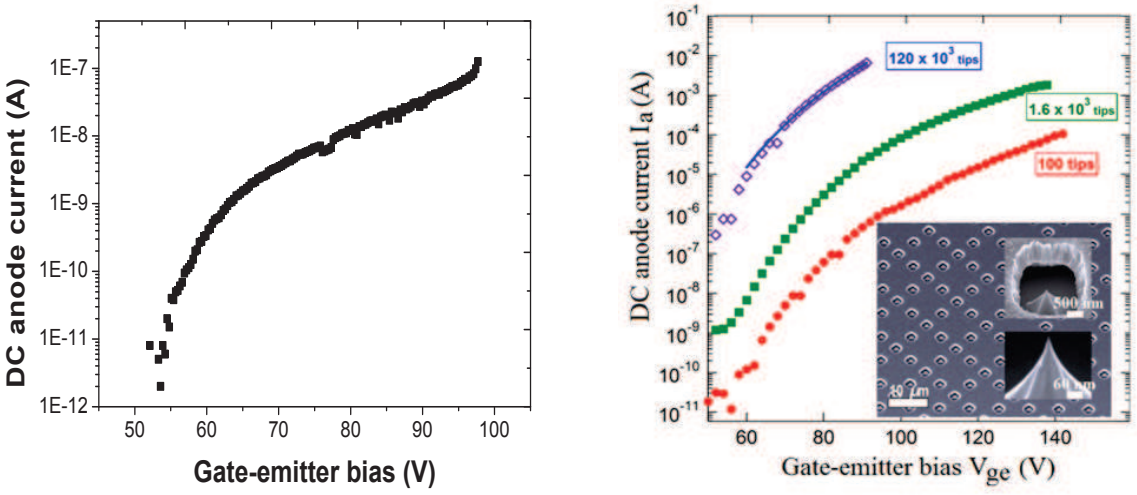

(a) (b)

Figure 4.15.: (a) Measured current-voltage characteristic on single double-gated Mo field emitter and (b) published data for a field emitter array (FEA) chip (Mustonen et. al., APL 99, 2011)

5. Fiber-based electron sources: development and measurements

The first idea of guiding light using transparent mediums dates from the 19th century when Daniel Colladon, a 38-year-old professor at the University of Geneva, demonstrated light guiding in a water jet. J. Babinet performed similar experiments using bent glass rods [93, 94], at about the same time in France, and he even suggested "dental illumination" as a first application. In the following years, the idea found a great success in applications like luminous fountains which were initially used in cities like London and Paris and then extended all over the world. In 1887, giant luminous water fountains were used as exhibition during the event celebrating the 50th birthday of Queen Victoria, which was held in Manchester. However, the most important evolution in the field was encountered in 1950's when the possibility of producing bundles of several thousands of fibers was demonstrated [95], and the idea of using fibers featuring a cladding layer, to improve transmission, was explored. A few years later, the theory of light propagating through fibers was also developed [96], and therefore a new field of physics was born. "One of the most beautiful, and most curious experiments that one can perform in a course on optics", as it was described initially by Colladon [93], constituted the "stem cell" in optics for one of the most important features of our day-to-day life: optical fibers.

The optical fiber manufacturing technology has continuously evolved and a continuous effort and studies on light attenuation in fiber optics [97, 98] pointed out fused silica as being the most promising material for this application. Besides their applications in fields that basically sustain the normal life as we know it today, like global communications, fiber optics represent a key instrument in scientific research as well. Apart from being used just as propagation mediums for laser beams, they also proved to bring important benefits in applications like microscopy. The so called Near Field Scanning Optical Microscopy (NSOM) method [99, 100] is a branch of microscopy that makes use of fiber optic tips. As the concept of near-field optical resolution beating the diffraction limit was first discovered in 1928 [101], the first experimental verification was only done in 1984 [102]. This was only possible due to another breakthrough that lead to the extraordinary resolution capacities of state-of-the-art microscopes. This was the fabrication

of nanometric apertures [103], which was first done in 1983 and which made possible fabrication of sharp fiber tips featuring nanometric open apertures at the tip apex.

This chapter is chiefly dedicated to the development and characterization of a new type of electron sources: the fiber-based electron sources. In this context both, large area photocathode structures (with emission areas of up to $100\,\mu m$) as well as sharp fiber tips (with apex sizes down to 100 nm) have been developed and characterized, and novel features have been explored. First, the capabilities of sharp fiber tips, with apex sizes of 100 nm was investigated in both: field and photo-field triggering conditions, using a continuous wavelength (CW) laser excitation. Next, a pulsed laser excitation was used to trigger single photon photoemission from fiber-based electron sources with emission areas of 50 and $100\,\mu m$ respectively. Besides the field-assisted photoemission experiments, electron beam emittance measurements were also conducted using the aperture scan technique, described in chapter 2. Moreover, an original design was used to push the applicability of the fiber-based electron sources to high electric field environments, as will be shown in section 5.3. This design was tested in an electric field environment of up to 8 MV/m, and electron beam characterization measurements were performed using the aperture and the solenoid scan techniques. These studies represent the first experimental results of this kind and the outcome, which will be discussed henceforth, opens up a new class of electron sources which could bring important advantages in the filed of electron diffraction techniques. At the end of the chapter, the possibility of multi-photon photoemission from flat fiber-based electron sources is discussed.

5.1. Optical fiber tips

In this sub-chapter, the use of fiber tips as electron sources is investigated. While the idea has been presented before [104–106] for an etched fiber tip [107–109] featuring a semiconductor coating, no consistent experimental verification was registered up to date, especially with respect to field-assisted photoemission. The approach here consists of coating the open aperture of a 100 nm apex size NSOM tip [99, 100] with a thin metallic layer, which is then back-illuminated by a laser beam propagating through the fiber. To reduce the work function of the coating material, an extraction electric field is also applied at the tip apex. The two main new aspects considered here are the use of a pulled fiber tip [110] instead of an etched one and the use of a metal, instead of a semiconductor material as electron source. Also, this represents the first attempt to back illuminate the tip, using the laser beam propagating through the fiber, all other attempts being based on external illumination [104–106].

The optical fiber tips used for this experiment were purchased from Nanonics Imag-

ing Ltd. [110], and are compatible with laser wavelengths ranging from 200 to 1200 nm. At one end, they feature a few mm long tapered region which reduces the fiber core diameter down to 100 nm. Using a pulled fiber tip, instead of an etched one, assures better transmission of the light to the apex due to the fact that the fiber cladding was not removed in the etching process. There are two kinds of tips that have been investigated here: Cr/Au coated tips and bare tips, which feature no coating. For the coated tips, the Cr/Au coating extends only on the tapered region and the fiber apex is left as an open sub-wavelength aperture, as represented in the figure 5.1. This extra metallic layer is meant to reduce the optical losses and guide the laser beam to the apex, where light can escape into a propagating beam.

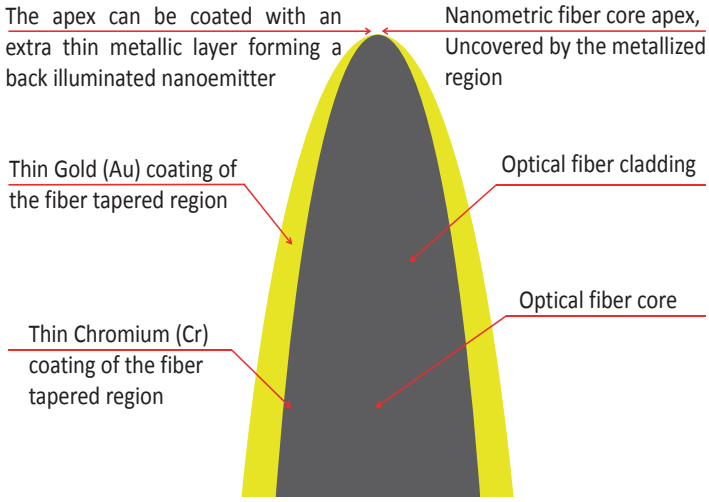

Figure 5.1.: Sketch of a Cr/Au pre-coated pulled NSOM optical fiber tip

In order to turn this device into a free electron source, an additional metallic layer was coated on the open aperture. The extra coating layer on the apex constitutes the electron source. Such a device represents a 100 nm back illuminated sharp electron source, where the work function of the emitter material could be considerably reduced in the presence of an extraction electric field. Another very important benefit of this concept is that the light travels through the fiber all the way to the apex thus, the difficulties of laser beam alignment being absent. The coatings were performed using the electron-beam deposition machine described in section 3.5. The fiber tips were mounted on a 360 degree rotary stage with the axis of rotation parallel to the metal vapor beam. Alignment of the fiber tips at a nominal angle to the rotational axis (45 degrees in the present experiments) ensured an uniform all-around metal coating on the tip and the mantle of the fibers.

To characterize these devices, two types of experiments were performed: cold field emission experiments and photo-field emission experiments. Both experiments were performed in the experimental chamber presented in section 3.1, and each of the two will be discussed separately in the following.

5.1.1. Field emission measurements

The coated optical fibers were attached to a standard Scanning Electron Microscope (SEM) plug using silver (Ag) paint which, besides holding the fiber, it also assured good electrical contact. The assembly was then mounted inside the vacuum chamber, where a base pressure of $5 \cdot 10^{-9}$mbar was achieved. The emitted beam was imaged using a phosphor behind the micro-channel plate imaging detector (MCP), while the corresponding emission current at the tip was measured using a highly sensitive ammeter[1]. The tip was kept grounded at approximately 10 mm away from the MCP and an extraction voltage between 1 and 3 KV was applied on the front MCP plate for both experiments. Figure 5.2 represents the experimental configuration described above.

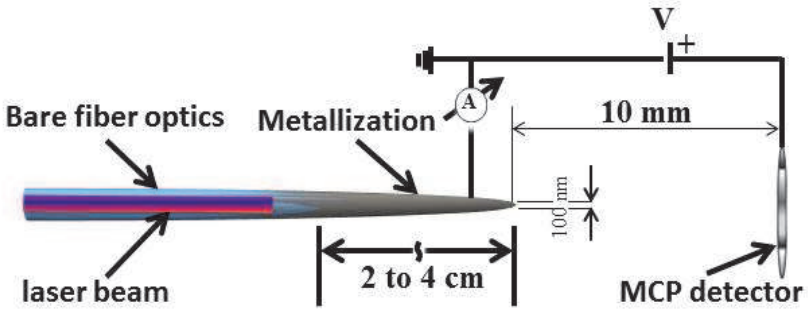

Figure 5.2.: Description of the experimental setup and the electrical circuit

A variety of metallic coatings, like Tungsten (W), Chromium (Cr), Platinum (Pt) and Gold (Au), with thicknesses varying between 10 and 40 nm were investigated on Cr/Au pre-coated fiber tips, similar to the one shown in figure 5.1. Cold field emission was found for all these layers, at extraction voltages ranging from 1 to 3 KV. Figure 5.3 shows the (I-V) characteristic for a Cr coated and a Pt coated tip, both having the same thickness of 40 nm. The maximum current achieved increased with time and the I-V characteristics was found to become smoother after a few days of consecutive current-voltage measurements. An interesting fact to mention here is that while the two tips show a similar emission current, they require different extraction voltages. For Cr, the voltage threshold for field electron emission was about 1150 V, as opposed to Pt and Au which started emitting at about 2000 V. For W, the electron emission threshold was found at a similar voltage to what it was observed for Cr, but the W layer was much thinner, only 10 nm.

Another key feature to mention here is that there was a clear difference on the life time of different metals and therefore not all of the mentioned coatings could last long enough until they could show stable field emission. For example, gold coated tips were unstable, and stopped emitting before an I-V curve could be recorded in contrast with

[1] Agilent B2902A

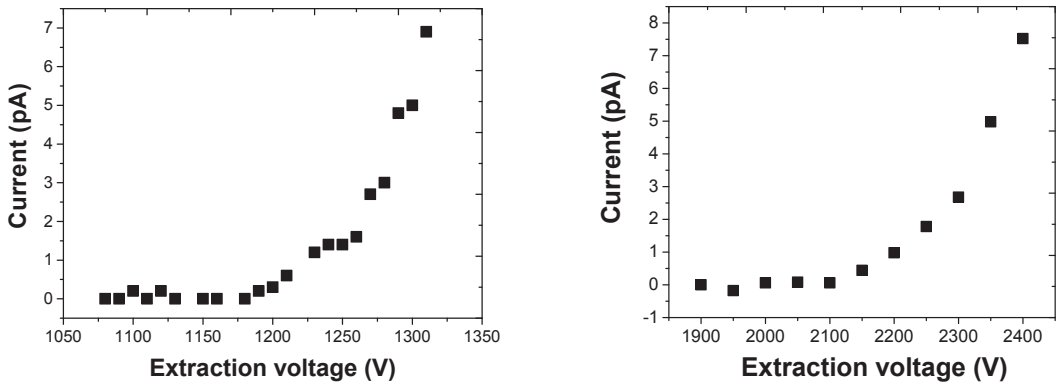

(a) (b)

Figure 5.3.: Experimental data: (a) current-voltage (I-V) emission curve for a 40 nm Cr coated tip and (b) for a 40 nm Pt coated tip

W coated tips which could run for a few months and proved to be most robust. Figure 5.4 shows the I-V characteristics for a 10 nm W coated tip, after a few days of conditioning. The higher emission current observed here, compared to the previous measurements, could be due to the longer conditioning time. Also, the thinner layer (10 nm instead of 40 nm), would lead to a lower scattering probability of the excited electrons on their way to the metal surface, as it was discussed in section 2.3. These considerations drove the author to the conclusion that the 10 nm coated W tip is the most suitable for the photo-field electron emission measurements, mainly due to its robustness. Moreover, recent studies [111] have reported for W a very good photoemission QE, on the order of 10^{-4}, which is even larger than the QE of commonly used photocathode metals, like Cu and Au [48, 72].

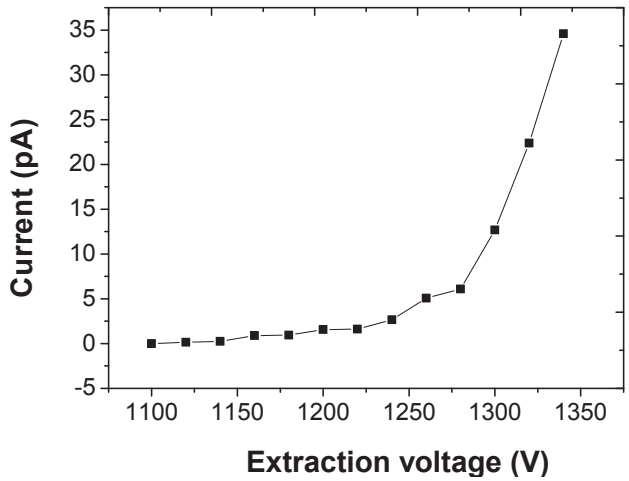

Figure 5.4.: Current-voltage curve for a 10 nm W coated tip

5.1.2. Photo-field emission measurements

Before proceeding to the photo-triggered measurements on the 10 nm coated W tip, a number of additional parameters were discussed with the scope of finding what are the experimental conditions required for a successful field-assisted photoemission measurement.

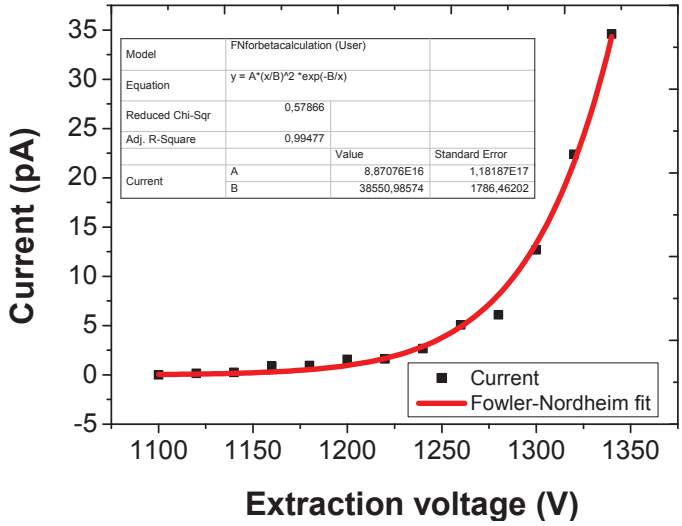

Figure 5.5.: Current-voltage curve (squares) and the corresponding Fowler-Nordheim fit (solid line)

First of all, a decision had to be made regarding the laser wavelength that is required for the experiment. The wavelength of the laser beam to be used has to correspond to a photon energy larger than the metal work function. As described in the chapter 2.1.2, in the presence of high electric fields, sharp emitters could experience a significant reduction of their work function. Using the methodology proposed by Fowler and Nordheim [24], and described in section 2.1.3, the enhanced electric field at the apex for the 10 nm W coated fiber tip could be estimated. For this, the measured IV curve represented in figure 5.4 was fit by the Fowler-Nordheim equation 2.5, and the fit result is shown in the inset of figure 5.5. Using the value $B \simeq 38.551$ obtained from the fit, an enhanced electric field at tip apex of $F_a = 2.3\,\mathrm{GV/m}$ was predicted, at an extraction voltage of $V = 1300\,\mathrm{V}$. To infer the potential barrier ϕ_{eff} that the excited electrons have to overcome to escape into vacuum, a work function of $\phi = 4.6\,\mathrm{eV}$ was assumed for the W layer [69]. In these conditions, the Schottky-reduced tunneling barrier ϕ_{eff} [112] is expected to be only 2.79 eV. This energy corresponds to the photon energy of a 445 nm wavelength laser beam. Any laser beam with a wavelength below this value should be sufficient to trigger direct single-photon photoemission. In this case, and because no other laser was available for the experiment, a 405 nm CW laser diode was bought for the photo-field emission measurements. Accordingly to the discussion made so far in this section, this wavelength should

be sufficient to overcome the reduced work function (ϕ_{eff} = 2.79 eV) of the 10 nm coated W tip.

The thickness of the metallic film is another parameter that plays a very important role on the success of the photoemission measurement, as it was also discussed in section 4.1 of the current thesis. While the electron current is basically a function of the laser flunce, this is not the only parameter that limits the achievable number of the emitted electrons. The thickness of the emitter layer has to also be within a given range. First, the photocathode layer has to be thick enough to absorb a sufficient fraction of the incoming photons, needed to trigger a detectable electron current. To understand better what percentage would be sufficient, a comparison with commonly used photocathodes was made. For example, one of the mostly used back illuminated photocathode structure that has already proved good performances [8, 67] consists of 20 nm Au coated on top of 2-3 nm of Cr, which acts as an adhesive layer between the gold and the glass substrate. A good estimation of the amount of light absorbed by the Au layer (the emitter) could be achieved if information about the absorption coefficient α of the composing metals are available. Luckily there are databases with these values [70]. Basically, the percentage of the initial light intensity that penetrates a distance z through a metal is given by $Tr = \exp(-\alpha \cdot z)$ where Tr is the light transmission. For the given situation, the light traveling through the back of the photocathode will first pass through the transparent glass substrate and through the Cr layer before reaching the Au, which is the electron source. At the 266 nm wavelength, which is normally used for these Cr/Au photocathodes, absorption into the glass substrate is basically negligible [113]. Still, around 5 to 10% of the incoming light will be lost here due to the relatively large thickness of these substrates (2-3 nm). Then, another up to 30% of the remaining photons will be absorbed by the thin Cr film, the Au layer being only reached by a fraction of just above 50% of the total number of the incident photons. Since only the Au layer contributes to the photoemission, it is only the absorption inside this layer that contributes the electron emission. Given that for Au $\alpha = 9.25 \cdot 10^5 \frac{1}{cm}$ at 266 nm, 84% of the light intensity reaching the Au film will be absorbed within this 20 nm thick layer. Only these very photons, which represent in the end less than 50% of the initial number of the incident photons, will contribute to the electron excitation, and this percentage has yet been proved to be sufficient when average laser powers of a few tens to a few hundreds of μW are used. Now, for the 10 nm thick W layer, a similar deduction can be made. Of course, in this situation where the emitter is sharp, the calculation will probably not be that accurate anymore, but should give a good idea of what is to be expected. Knowing that for W $\alpha = 1.25 \cdot 10^6 \frac{1}{cm}$ at 266 nm, it is straightforward to conclude that above 73% of the laser power reaching the fiber, after traveling through it, will be absorbed by the 10 nm thin film. This is a good value as discussed above, being even 20% larger than in the case of the Cr/Au photocathodes. Of course, this deduction was made for a 266 nm laser wavelength, but at the 405 nm wave-

length which will be used here, the 10 nm thick W layer will still absorb about 55% of the incident number of photons. This value is still above what was deducted for the working Cr/Au structure. Moreover, because the emitter is a sharp tip, the field enhancement present at the apex will reduce the work function of the W layer which will increase its QE.

On the other hand, the photocathode would have to be thin enough so that the excited electrons will travel only a short distance to the surface, so they could escape into vacuum before losing energy due to scattering events. The excess energy of the excited electrons, i.e. the difference between the incident photon energy (3.06 eV for the 405 nm laser wavelength) and the reduced metal work function (ϕ_{eff} = 2.79 eV as discussed above), will be lower than the effective work function of the W fiber tip. In this context, scattering events could strongly reduce the amount of electrons that will be emitted into vacuum. This aspect was discussed in detail in the theory chapter of this thesis (2.3) and does not need to be explained again here. Nevertheless, in case of W, the optical skin depth λ_{opt}, calculated using equation 2.22, will be about 9 nm at a 405 nm laser wavelength. This is comparable to the layer thickness which suggests that the undesired scattering events have a low probability to take place. In conclusion, the 10 nm coated W fiber tip should be compatible with photoemission at the given 405 nm laser wavelength.

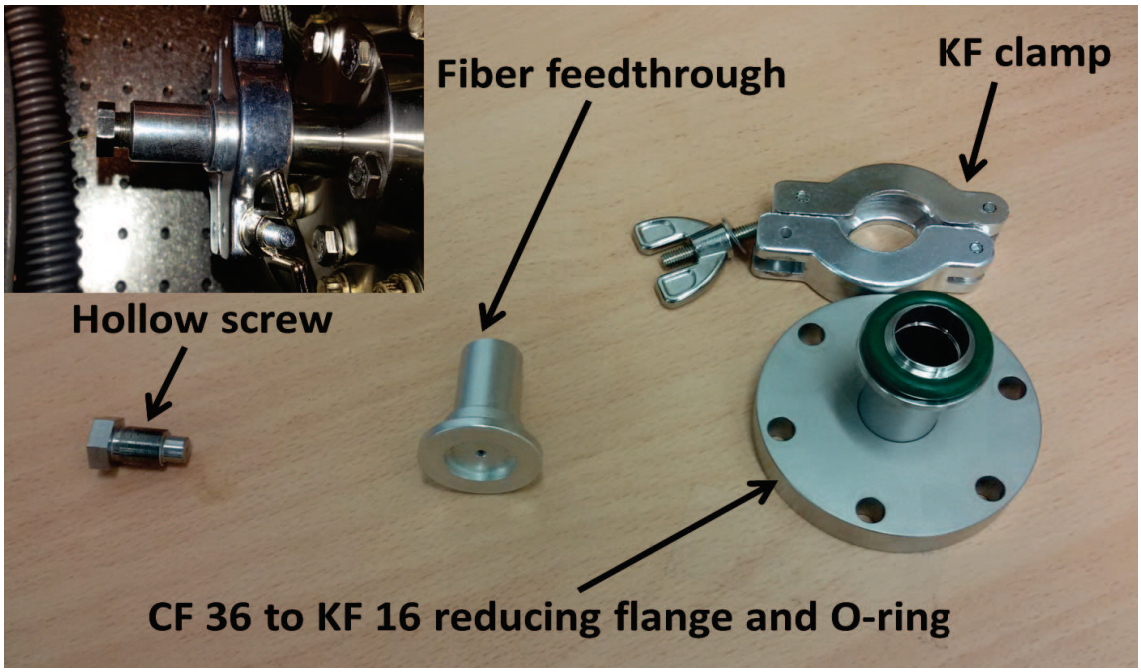

Figure 5.6.: Component parts of the optical fiber feedthrough purchased from Nanonics Inc.

For the photo-field emission measurements, laser coupling to the fiber was achieved outside the chamber and a special fiber feedthrough purchased from Nanonics Inc. was used for the air-vacuum interface, as shown in figure 5.6. The fiber feedthrough was com-

posed of two threaded parts through which the fiber can be fed. One part was a hollow screw while the other (the fiber feedthrough) contains in the center a cylindrical elastic material that surrounds the fiber and has a bore diameter close to the outer diameter of the fiber. First, the CF36 to KF16 reducing flange was attached to the vacuum chamber and then the fiber feedthrough was fixed on the flange using an O-ring and a KF clamp. After the fiber was fed through the assembly, a small amount of vacuum grease was applied on the portion that will be situated inside the feedthrough in the final step. Finally, the hollow screw was attached and this puts pressure on the elastic part inside the vacuum feedthrough which will bend and fix the fiber. To achieve laser fiber coupling, a standard FC/APC[2] fiber connector was attached to the air end of the fiber and was polished manually as explained in section 3.6.

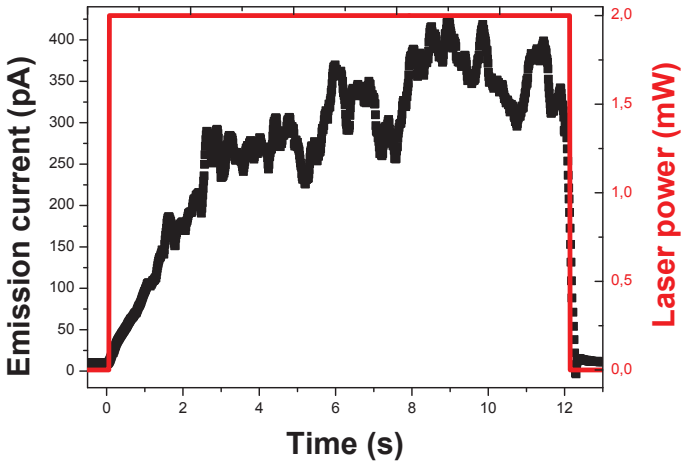

Figure 5.7.: Response of electron emission to application of laser for an unconditioned tip, and in the presence of no field-emission current (black squares); the applied 405 nm CW laser power (red solid line)

The measurements clearly revealed an enhanced emission current in the presence of the CW light trigger, as shown in Figures 5.7 and 5.8. For these measurements, 2 mW of average power was used. Figure 5.7 shows the initial electron emission current triggered by the CW laser beam, before any conditioning of the tip. No cold field emission was present when the laser was applied. Nevertheless, the extraction voltage between the front MCP plate and the tip apex was around 1200 V assuring the work function reduction as discussed above. The complete recovery of the emitted current to the initial value (before the laser trigger was applied) strongly suggests that no changes on the tip structure occurred during these measurements. Therefore, the structure of this fiber tip approximates the sketch represented in Figure 5.1.

Despite the obvious emission enhancement, the dynamics of the current increase

[2]Thorlabs part no. 30128A3

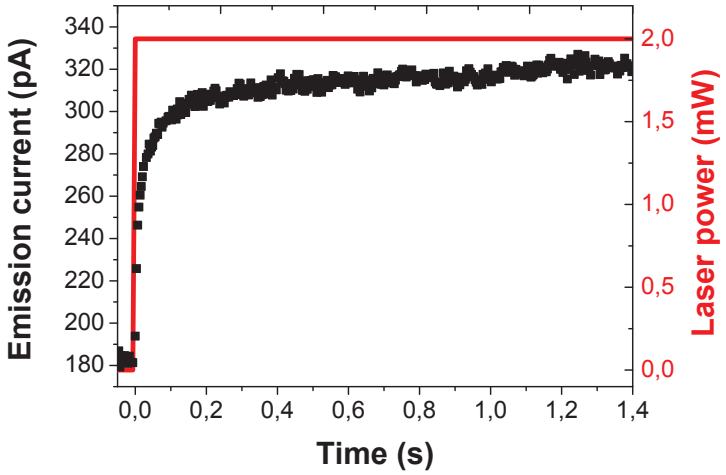

Figure 5.8.: Response of electron emission to application of laser for the conditioned tip, and in the presence of a field-emission current of about 180 pA (black squares); the applied 405 nm CWlaser power (red solid line)

was found to be very slow. In order to characterize this better, the temporal behavior of the emission current was measured. For this, the two channels of the source-measure unit[3] were used to simultaneously power the laser diode and to measure the emission current from the fiber tip. Therefore, the temporal behavior of the emission current with respect to the time when the laser trigger was applied to the fiber was obtained, as shown in Figures 5.7 and 5.8.

The switch-on emission time proved to be very sensitive to a number of factors. For similar tips, different electron emission transients were measured, depending on the time that the tip was conditioned and on the base field-emission current at which the laser trigger was applied. Figure 5.8 represents the switch-on time for an identically W coated tip, after two weeks of 1-1.5 hours of measurements per day. In this case, the CW light was applied when the tip was already field-emitting a current of about 180 pA. For these conditions, an electron emission transient with a half rise time of only approximately 10 ms was measured, which is much shorter than a few seconds which was observed on an unconditioned tip (figure 5.7). The change of the electron emission transient could be due to structural modifications of the tip during conditioning. This explanation is strongly supported by our SEM images of the tips before and post conditioning. Figure 5.9 represents the same fiber tip before the experiment (a) and after the experiment (b) after the tip became very unstable, and was not emitting anymore. The image clearly shows that ablation of the metallization has occurred at the fiber tip, likely as a result of the application of the extraction field or the 405 nm light, or a combination of both. This could lead to changes in the heat capacity and heat conduction properties of the emission region, which

[3] Agilent B2902A

will influence the local thermal dynamics and the concomitant emission current transient. Still, regardless on the conditioning process, the emission rise-time was never found to be faster than milliseconds which excludes photo-field emission as the predominant emission process, which should have followed the rise time of the laser diode (on the order of microseconds). These facts lead to the assumption that a thermal enhancement of the field emission current is present, where the fiber nanotip is heated by the incident laser. The emission current increase is based on changes induced in the population of electron states inside the W layer. At a higher temperature, states above the Fermi level become more populated, enhancing tunneling through the barrier which is lowered by Schottky-type image charge potential in the presence of the high electric field. As discussed in various theory publications [17, 25, 26, 29] and also shown experimentally in [27], this can lead to significant current increase even far away from the thermionic (Richardson) regime, where electron states with energies above the barrier become populated thermally.

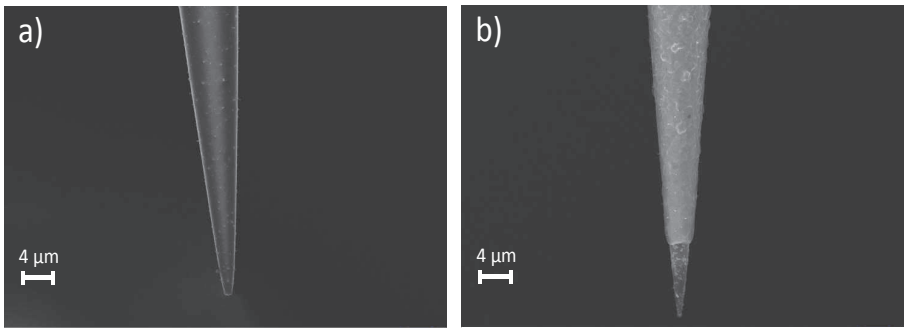

Figure 5.9.: SEM image of a fiber tip (a) before the experiment and (b) after measurements and conditioning (b)

In order to validate the hypothesis of thermally enhanced field emission, the in-air temporal thermal transient that is triggered by the incident light was measured. For this purpose, a nanometric thermocouple probe based on a standard Pt/Au junction was fabricated by the author. The probe was made from a metal electrode purchased from Nanonics imaging Ltd which consisted of Platinum (Pt) wire inside of a glass tube, which was pulled at one end to form a $1\,\mu m$ diameter tip. The author coated this structure with a Gold (Au) layer on the outside as shown in Figure 5.10 (a). The Seebeck coefficient of the device was inferred to be about $7\,\frac{\mu V}{K}$ from the calibration curve presented in Figure 5.10 (b). This value is consistent with values reported in literature for a Pt/Au junction. The measurement of the thermal response of the NSOM tip was achieved by touching the two tips using a precision three-axis translation stage (Figure 5.11 (a)) and measuring the voltage across the junction. In Figure 5.11 (b), the result of the in-air temperature switch-on time measurement is shown, and a corresponding temperature increase at the tip of about 18 K can be inferred. The thermal half-rise time $t_{\frac{1}{2}} = 21\,\text{ms}$ turned out to be similar to the

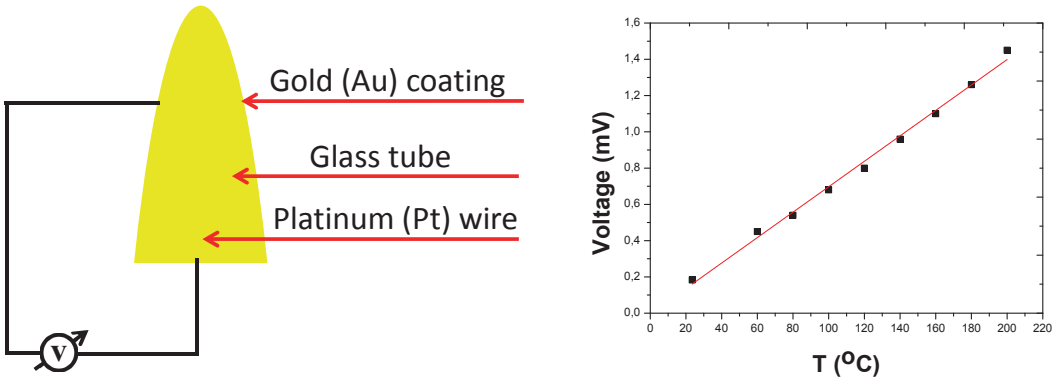

(a) (b)

Figure 5.10.: (a) Thermocouple sketch and the basic circuit and (b) the thermocouple voltage calibration

corresponding value of the emission current switch-on time observed for the same tip, as represented in figure 5.11 (b). This match of the thermal transients and the electron emission transient after conditioning is considered as proof corroborating the photo-thermal emission hypothesis. It has to be mentioned here that the measured temperature increase with the micrometric thermocouple is not sufficient to fully explain the enhanced current. This is the temperature rise at the contact point which is relatively far away from the very apex where the temperature could be much higher and is not directly measureable. Still, the thermal dynamics measured here should be in good agreement with the real case.

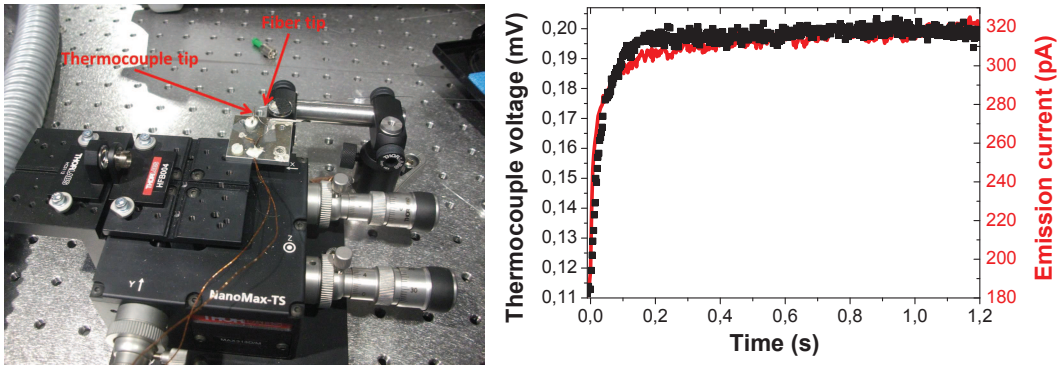

(a) (b)

Figure 5.11.: (a) Description of the setup used to measure the thermal transient triggered by the application of the 405 nm CW optical excitation; (b) In-air temperature switch-on curve after triggering the fiber tip with the 405 nm CW laser (black squares) and the fast optically enhanced electron emission switch-on curve from figure 5.8

In order to gain even more insight on the problem, another very important aspect was raised for discussion: Is the average laser power that reaches the fiber tip apex suf-

ficient to produce a photo-emitted current on the order of 10 pA or larger, so that it can be detected by the available source-measure unit[4]? This is a good question to ask here, given the sub-wavelength size of the fiber open aperture. Likely, the amount of the laser power that reaches the fiber tip apex can be directly measured using an uncoated 100 nm open aperture tip. At the given 405 nm wavelength, the optical transmission efficiency was measured using a low-noise CCD camera. After taking and analyzing images from various polar angles with respect to the optical axis, the angular emission pattern could be measured. To infer the absolute value of the transmitted power, a previously obtained calibration of the camera signal and the known aperture area of the CCD camera lens were used. This measurement revealed that only a fraction between 10^{-7} and 10^{-5} of the laser power that enters the fiber will reach the apex and escape into a propagating beam. Therefore, while single-photon photo-field emission should be allowed at the applied wavelength, due to the Schottky lowering of the work function discussed above, the low transmission of the sub-wavelength fiber tip might make such a process extremely weak. Using the QE equation derived below (equations 5.1 and 5.2), and assuming an average input laser power of 2 mW at the fiber, it was found that the QE of the 10 nm W film would have to be on the order of $1.5 \cdot 10^{-1}$ to emit an average electron current of 10 pA, which could be detected using the available source measure unit[5]. This value is much larger compared to 10^{-4} which is the QE normally expected for W [111].

$$\left.\begin{array}{l} QE = \frac{n_{electrons}}{n_{photons}} \\ I = \frac{Q}{t} \\ Q = n_{electrons} \cdot e^{-} \end{array}\right| \Longrightarrow \; n_{electrons} = \frac{I \cdot t}{e^{-}} \; \left| \Longrightarrow \; QE = \frac{I \cdot t}{n_{photons} \cdot e^{-}} \right. \tag{5.1}$$

where $n_{electrons}$ is the number of emitted electrons, $n_{photons}$ is the number of incident photons, I is the emitted current, Q is the charge and t the time.

$$\left.\begin{array}{l} n_{photons} = \frac{W}{E_{photon}} \\ E_{photon} = \frac{h \cdot c}{\lambda} \\ W = P \cdot t \end{array}\right| \Longrightarrow \begin{array}{c} n_{photons} = \frac{P \cdot t \cdot \lambda}{h \cdot c} \\ eq.\ (5.1) \end{array} \; \left| \Longrightarrow \; QE = \frac{I \cdot h \cdot c}{P \cdot \lambda \cdot e^{-}} \right. \tag{5.2}$$

These results are to conclude that the optical transmission of the 100 nm apex size fiber tip, at the 405 nm wavelength, is too low to trigger a photoemitted electron current that can be measured, and thermally assisted field emission is the predominant process observed here. This is not to say that the thermal effects will not be significantly reduced

[4] Agilent B2902A
[5] Agilent B2902A

when using a pulsed laser and/or higher photon energies. Shorter wavelengths in the ultraviolet, and shorter pulse durations down to femtoseconds, should reduce the thermal effects and give larger photon transmission efficiencies to the tip and a higher QE of the emitter metal, facilitating direct, potentially ultrafast photoemission.

5.2. Flat fiber-based electron sources

The optical transmission efficiency of the fiber tips can be systematically increased up to more than 90% of the input power by changing the size of the open aperture. Therefore, the emission mechanisms in these devices can be potentially varied between thermionic emission, photoemission (single-photon emission), multi-photon over the barrier emission and photo-field enhanced emission or a combination of any of these processes [114]. For the optical fibers used above in section 5.1.2, the open aperture diameter can be varied from the size of the 100 nm apex up to the size of the initial optical fiber core of $50\,\mu m$ for the multi-mode NSOM fibers. Increasing the electron emission area will of course lead to an increase of the beam emittance but even the largest aperture size that can be achieved here, i.e. $50\,\mu m$, could be considered a good value when compared to what is usually used inside common electron guns. Another consequence of increasing the emission area is that the work function reduction due to Schottky effects will not be significant anymore (not using sharp tips). Thus, a shorter laser wavelength will have to be used to overcome the work function of the emitter material which is typically between 4.1 and 4.6 eV [69, 76].

For these experiments, a laser wavelength of 265 nm (4th harmonic of our PHAROS system with the spectrum shown in 5.13 (b)) was available, with a pulse duration of 170 fs, at 1KHz repetition rate. Unfortunately, at this wavelength, the well known problem of color center formation or solarization of the fiber [115–118] is significant and has to also be included into the discussion. Recently, great success in reducing these effects has been achieved [119, 120] and large-mode-area solid-core photonic crystal fibers proved much better optical transmission in the deep UV domain, even for relatively high input powers (10 mW) [121]. Unfortunately, these types of fiber were not available for the current experiment. Instead, the optical transmission over time, for a solarization resistant multi-mode optical fiber[6], and for a NSOM fiber were investigated. For these measurements, both of the fibers were cut-off at both sides and standard ceramic polishing plugs were attached, as described in section 3.6 and shown in figure 3.7 (a). Thus, no fiber tips were used here, and the light escapes into a propagating beam from an area equal to the size of the fiber core. As it is shown in figures 5.12 (a) and (b), a large amount of the

[6] Thorlabs UM22-100 Solarization Resistant multi-mode optical fiber with Polyimide Coating, for 180 - 1150nm wavelength

light is absorbed by the fiber and there seems to be a relaxation time of a few hours. Still, a stable region is reached in both cases, but at a lower transmission power in the NSOM fiber case.

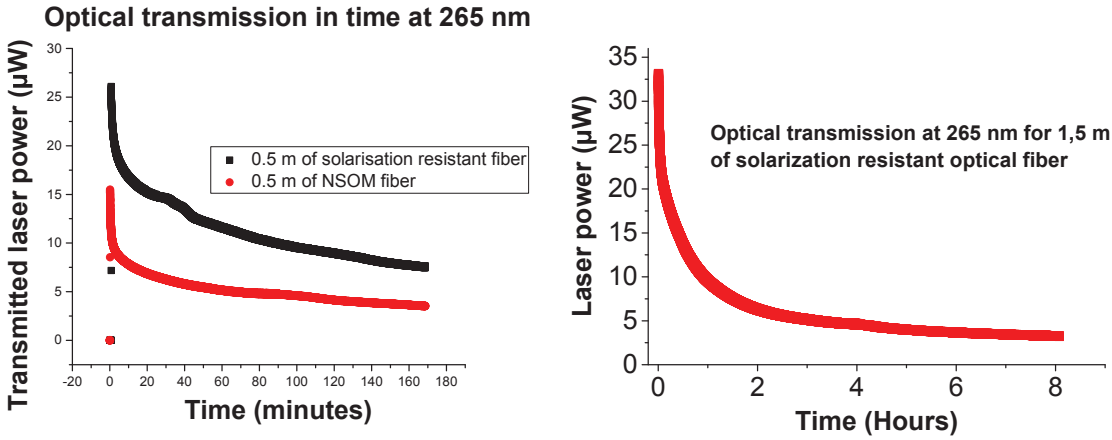

(a) (b)

Figure 5.12.: (a) Optical transmission over time for two types of fibers: fiber cut from the NSOM fiber tip (red) and fiber cut from the solarisation rezistant fiber from Thorlabs (black); (b) Optical transmission as a function of time for the solarisation rezistant fiber from Thorlabs (longer time period and longer fiber extension (a))

For the photoemission measurements, a cut from the NSOM fiber was employed first. As these fibers feature a tip ending with a 100 nm open aperture, the initial approach was to use a fiber polishing machine, as described in section 3.6, to systematically cut-off portions from the initial tip. The scope of this was to find the size of the open aperture, at which the thermal effects are not significant anymore. In this polishing method, the final size of the polished fiber is given by the size of the ferrule used, which also plays the role of a holder (section 3.6). Basically, during the polishing the fiber material is removed, until the polishing sheet gets as close as possible to the ferrule holder tip. Unfortunately, due to the very short tapered length of the NSOM fibers, of a few hundreds of micrometers, it was very difficult to access the tip, more investigation and work being required until a satisfactory method for controlling the size of the open aperture will be found. This could be achieved by fabricating custom ferrules, featuring the required bore size, or by self-fabricating and/or pulling the fibers. All of these aspects will be addressed in the near future.

Still, as mentioned above, the 50 μm core size of the NSOM fibers is a fairly good value, which should provide a good emittance of the electron beam. Also, the main target here is to advance the method from the previous step, where thermal effects were predominant, to the point where electron emission with photoemission as predominant

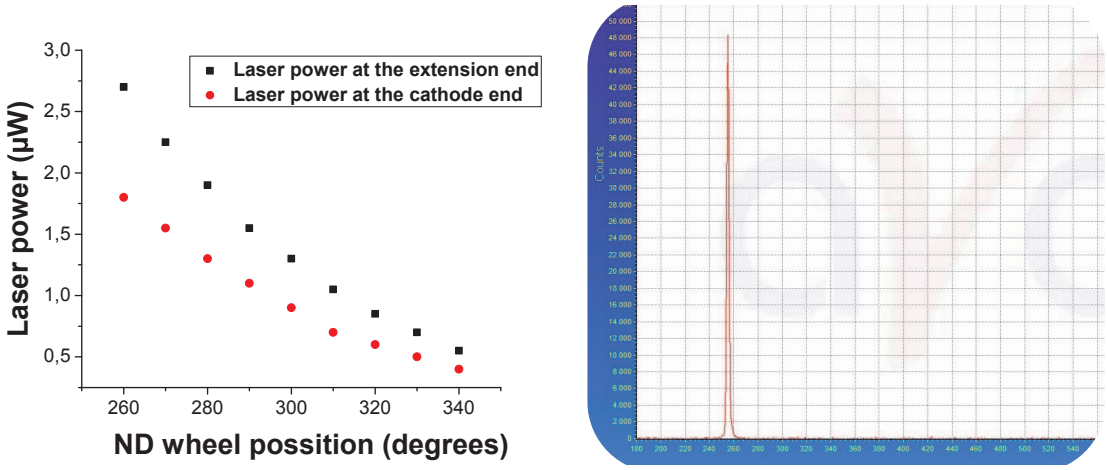

(a) (b)

Figure 5.13.: (a) Calibration of the laser power as a function of the position of the ND filter at two positions: at the end of the extension fiber cut (black) and at the photocathode position (red); (b) Spectrum of the used pulsed laser beam

mechanism is demonstrated. In this context, the fiber was simply cut-off at one end, manually polished and metalized. This time, in order to avoid as many problems as possible, a well known emitter metal structure was used: 30 nm Au deposited on 3 nm Cr [81]. As it was already measured before, and is shown in figure 5.12, in the cut-off case, where the size of the open aperture equals the initial core size of the optical fiber, despite the high losses into the fiber, there is still significantly more output laser power than in the 100 nm tip case. The measured value of about $3\,\mu W$ should be sufficient to trigger an average electron current on the order of a few pA, at the given repetition rate, which should be easy to detect using the available source-measure unit[7].

In order to be able to measure or to gain a good estimate of the amount of laser power reaching the photocathode, after it was inserted into the vacuum, two portions of fiber were used. From now one these will be referred too as the *extension* fiber and the *cathode* fiber. The *extension* fiber has both ends outside the vacuum, and was used at one end to couple the free space laser beam into the fiber, and at the other end it was attached to the *cathode* fiber using a double sided fiber connector[8] depicted in Figure 5.14 (a). The *cathode* fiber guides the light from the *extension* fiber, on the air side, to the photocathode inside vacuum. The air-vacuum interface is assured using the same fiber feedthrough as presented earlier in figure 5.6. Now, this approach allows to directly measure the amount of the laser power reaching the cathode, due to the very low losses on the fiber-fiber coupler. Standard ceramic connectors, identical to those used for laser coupling into the fiber (figure 3.7), were initially attached at all of the four ends of the two fiber cuts, and were manually polished down to $0.3\,\mu m$ roughness, following the procedure described in

[7] Agilent B2902A
[8] Thorlabs part number ADAFC3

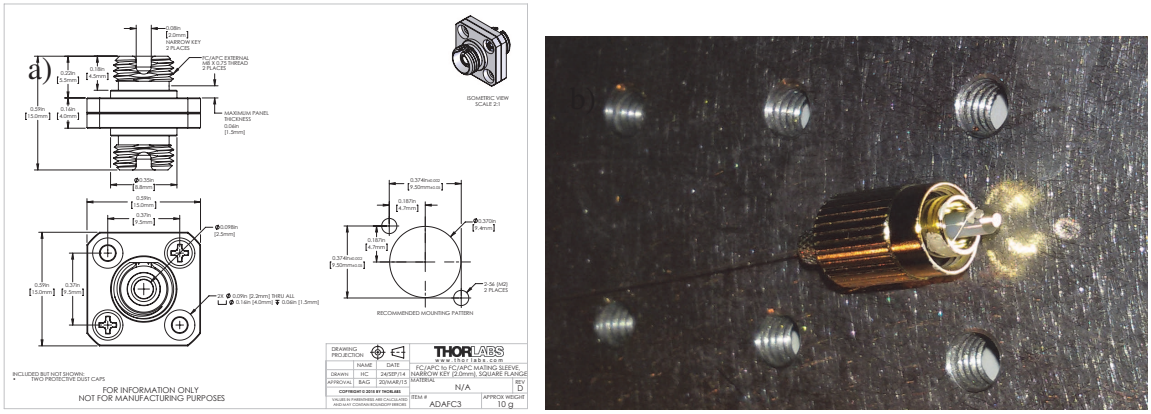

Figure 5.14.: (a) Thorlabs drawing of the two-sided fiber connector used between the extension and the cathode fiber cuts and (b) picture with the Cr/Au coated fiber plug and the electrical contact between the emitter layer and the plug metallic section

section 3.6). After the two fibers were conditioned (laser beam was propagated through them for a few hours until the optical transmission efficiency stabilized), the transmission efficiency through both fibers, separately, and connected together was measured. A calibration of the power coming out of the plug that will be subsequently metalized, was performed as a function of the input power into the *extension* fiber. This will represent the fraction of laser power that will reach the emission material, and will be considered for QE calculations. The input laser power that was coupled into the extension fiber was varied by using a neutral density (ND) filter wheel. The result, shown in figure 5.13, proves that the second portion of the fiber (the *cathode* fiber) only absorbs about 30% of the input power (the output power from the *extension* fiber), which is low compared to more than 95% that is lost in the extension portion after the long-time conditioning process shown in the figure 5.12 above. Also, the *cathode* fiber does not reveal the same conditioning time, its transmission being more or less constant in time from the beginning. This could be explained by the fact that there is a much lower laser intensity at the *cathode* fiber input, and on the other hand, the spatial profile of the input laser beam is much better here, being shaped by the first fiber (the *extension* fiber).

After the laser power calibration was successfully conducted (figure 5.13 (a)), the *cathode* fiber was mounted inside the deposition machine and Cr/Au coated (30 nm Au on top of 3 nm). The fiber had a loose end to allow mounting during metalization and subsequently into the vacuum chamber, using the special fiber feedthrough (figure 5.6). Before closing the vacuum chamber, electrical conduction was verified between the emitter layer and the multi-PIN feedthrough, where the source-measure unit was later connected. A short piece of metallic wire was attached between the ceramic and the metallic part of the plug using Ag paint, as represented in figure 5.14 (b). A base pressure on the order of 10×10^{-9} mbar was achieved after pumping down for a few days. The distance between

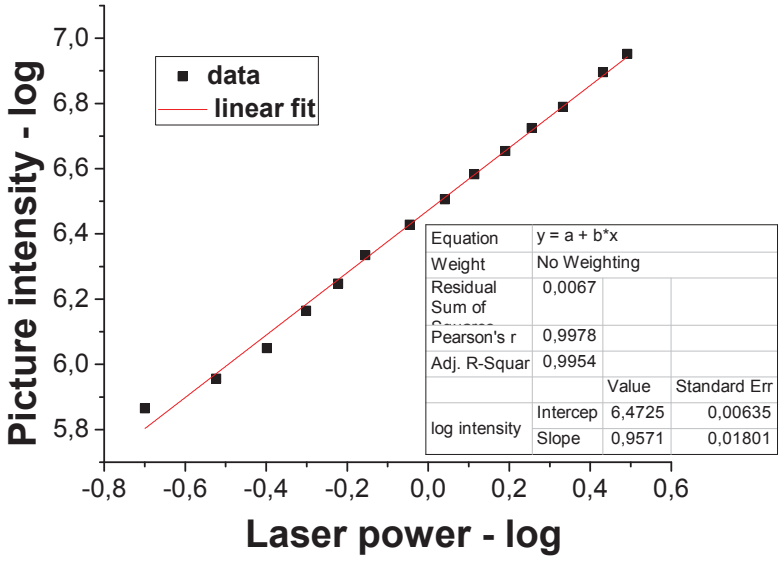

Figure 5.15.: Electron emission current as a function of the laser power (black squares) and a linear fit (red line)

the photocathode surface and the MCP detector screen was set to about 10 cm.

This very fiber-based photocathode (figure 5.6) was the first to successfully prove electron emission via the photoelectric effect, as shown in figure 5.15. Unfortunately, the total electric current emitted from the metallic layer could not be measured here due to the large noise induced by the electrical cables, which were not properly shielded at that time. Alternatively, the electron beam could be detected on the MCP screen and beam images were recorded for each position of the ND filter wheel. Using the laser power calibration obtained previously, a linear dependency was found between the electron beam intensity on the screen (sum of the pixel counts) and the laser power reaching the Au layer, as it is shown in the figure 5.15. This, and also the fact that the electron beam instantaneously followed the laser excitation, no emission rise-time that could be measured was present, are proof that electron emission is due to single-photon excitation of electrons, via the photoelectric effect.

Emittance measurements

Now that photoemission from a fiber-based electron source was achieved, the next step was to characterize the emitted electron beam. For this purpose, the aperture scan technique described in section 2.4.2 was used. The experimental setup was updated by adding a two axes translation system, as shown in figure 5.16. Two linear stages, with a travel range of 21 mm[9] and 20 mm[10] respectively, purchased from SmarAct, were

[9] SmarAct SLC-1730-D-S-UHVT
[10] SmarAct SLC-1730-O20-D-S-UHVT

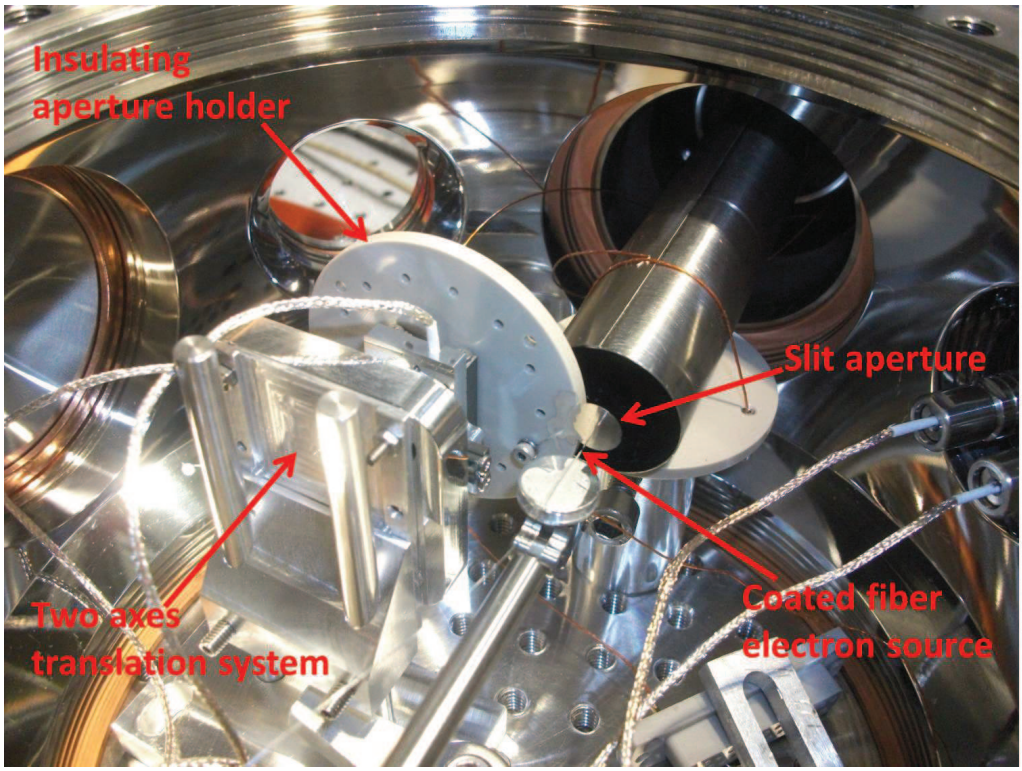

Figure 5.16.: Picture with the experimental configuration where the relevant parts are indicated

mounted together to create a *XY* translation system. This has been used to scan through the electron beam with a slit aperture. The aperture used here was $1\,\mu m$ wide and 1 mm long, and was mounted on the translation stages using an insulating PEEK holder, as shown in figure 5.16. The travel range of the translation system allows to completely move the aperture in and out of the electron beam path, so that the full beam can also be visualized on the MCP. The slit aperture, of which total size including its holder is 1 cm in diameter, could also be used to measure the electron beam current. In this case, the aperture acts as an anode plate which blocks the beam and can be connected to the source-measure unit, and biased to collect the electron beam.

For the scan, the fiber-based photocathode was biased at $-200\,V$ and the aperture was grounded and placed 1 mm downstream. The MCP front plate, situated 10 cm away from the fiber, was biased at about 80 V, as shown in figure 5.17 (c). Before starting the scan, four background images were saved and then, for each position of the aperture, four signal images were recorded. The aperture was translated over a range of $170\,\mu m$, with a step size of $10\,\mu m$. By knowing the distance between the aperture and the MCP detector, and by measuring the RMS size of the electron beam on the screen, after passing through the slit aperture, the local (uncorrelated) angular spread σ_θ of the electron beam could be inferred. Moreover, the beam profile at the aperture position was inferred from the scan by plotting the intensity of the electron beam as a function of the aperture position. The RMS beam size $\sigma_{x,rms}$ was then obtained from the beam profile, and the geometric

emittance of the beam was calculated using equation 5.3.

$$\varepsilon_{rms} = \sigma_\theta \cdot \sigma_{x,rms} \tag{5.3}$$

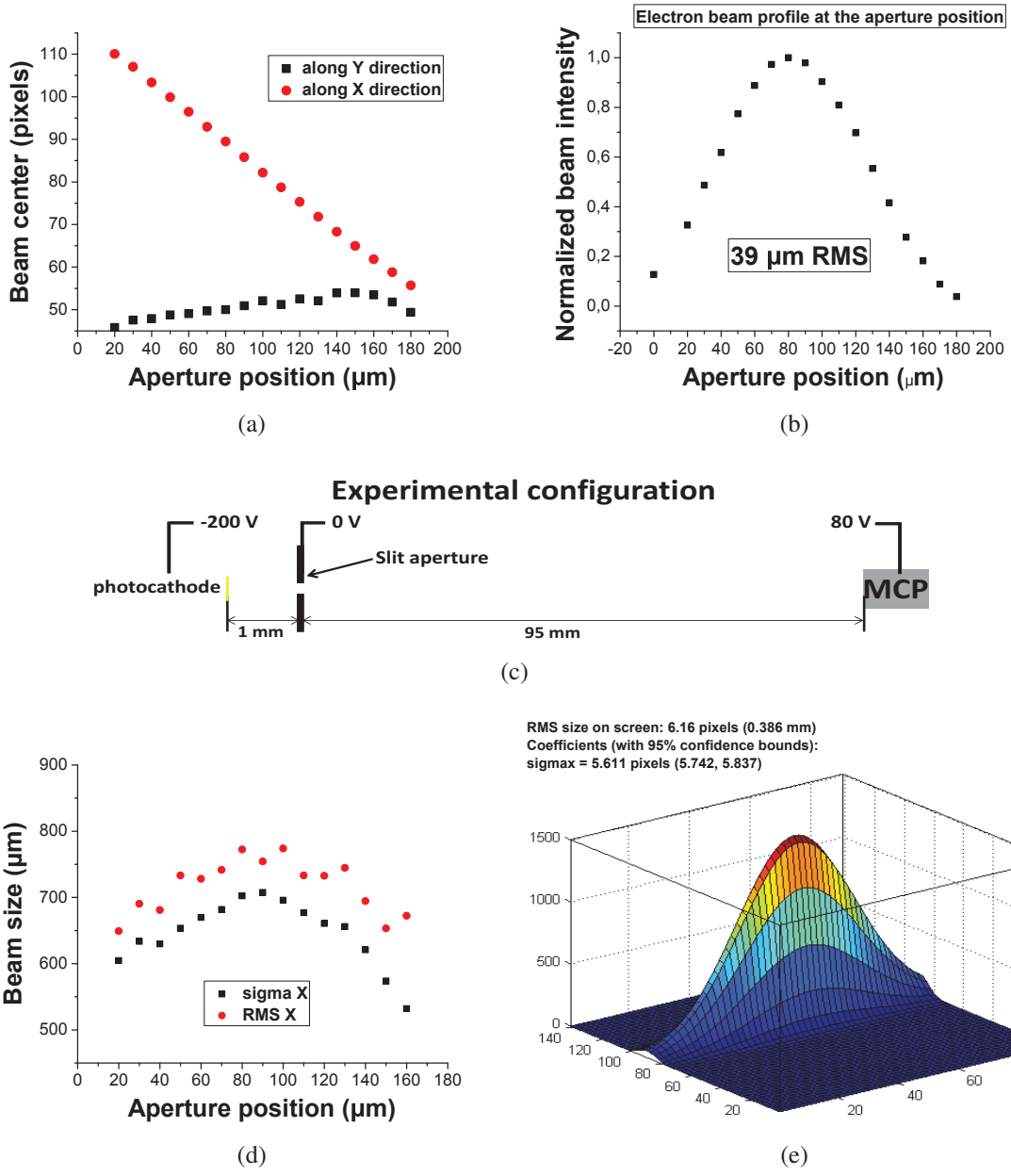

Figure 5.17.: Measurement results for a 50 μm core size NSOM optical fiber. (a) Center of the transmitted electron beam (through the aperture slit), at the screen position, as a function of the aperture position; (b) Electron beam profile at the aperture position; (c) Experimental configuration; (d) Size of the transmitted electron beam (through the aperture slit), at the screen position, derived from the 2D Gaussian fit (black squares) and from RMS calculation (red squares); (e) 2D Gaussian fit of the transmitted electron beam where the axes are in pixels and, in the inset, image with the actual transmitted electron beam on the screen

In equation 5.3, it is assumed that zero correlated angular spread was present, which is the case for a vanishingly small aperture. The uncorrelated (local) angular spread σ_θ is inferred using the RMS width at the screen, of the electron beam passing through the slit. It is therefore critical in this context that the recorded images are properly analyzed, and an accurate RMS beam width is estimated. A detailed description of how was the RMS beam size at the screen position calculated, was described before in section 4.2.

The aperture scan result is displayed in figure 5.17 (a) to (e). Due to the fact that the translation is only done along one coordinate, the position of the electron slit on the screen will also appear to move across only one direction (figure 5.17 (c)). Therefore, the center of the distribution on the MCP screen will only change across the *X* direction while it stays constant along the *Y* direction. For each aperture position, the sum of all pixel intensities was calculated, and the beam profile was obtained. As it is shown in the figure 5.17 (b), the beam has a Gaussian profile with an *RMS* value $\sigma_{x,rms}$ of $39\,\mu m$. This is the RMS value of the entire electron beam at the aperture position, which is situated 1 mm away from the photocathode surface, as shown in the experimental configuration (figure 5.17 (b)). The local angular spread of the beam (σ_θ), was calculated for the case when the aperture was in the center of the electron beam, i.e. $80\,\mu m$ away from the initial position, as shown in figure 5.17 (b). Using the value of the acceleration voltage (200 V), the normalized emittance obtained for the $50\,\mu m$ fiber core size was found to be $\varepsilon_{n_x,rms} = 8.9\,\pi$ nm, using equation 2.14. This value is very good when compared to other results [47, 67, 81] or to the theoretical prediction made by the three-step model for photoemission using equation 4.12 (described in section 2.3). The transverse coherence length was found to be $L_x = 1.7$ nm from equation 2.19 (section 2.2.4).

For comparison, another aperture scan experiment was performed for a solarization resistant fiber purchased from Thorlabs, which should give a better optical transmission as it was shown in the figure 5.12 (a) and (b). For this measurement, the vacuum chamber was opened and modifications have been made as shown in figure 5.18 (c). These were required to allow for a larger acceleration voltage (up to 1500 V) and for a free drift region after the slit aperture. The new experimental configuration, as well as the aperture scan results are shown in figure 5.18. This time, the electron beam had an RMS value of $52\,\mu m$. Using the RMS size of the electron distribution shown in figure 5.18 (e), the local angular spread was found to be $\sigma_\theta = 3.42$ mrad, which gives a RMS emittance of ε_{rms}=$178\,\pi$ nm, corresponding to a normalized emittance of $\varepsilon_{n_x,rms} = 14\,\pi$ nm in this case. This larger value was in fact expected given the size of the new fiber core, which was $100\,\mu m$ instead of $50\,\mu m$. Due to the larger emittance value than above, the transverse coherence length will be smaller this time: $L_x = 1.4$ nm.

Due to the larger emission area as well as due to the better optical transmission of the new optical fiber, an absolute emission electron current could be measured this time, as shown in figure 5.19 (a) and (b). The input laser power at the extension fiber was

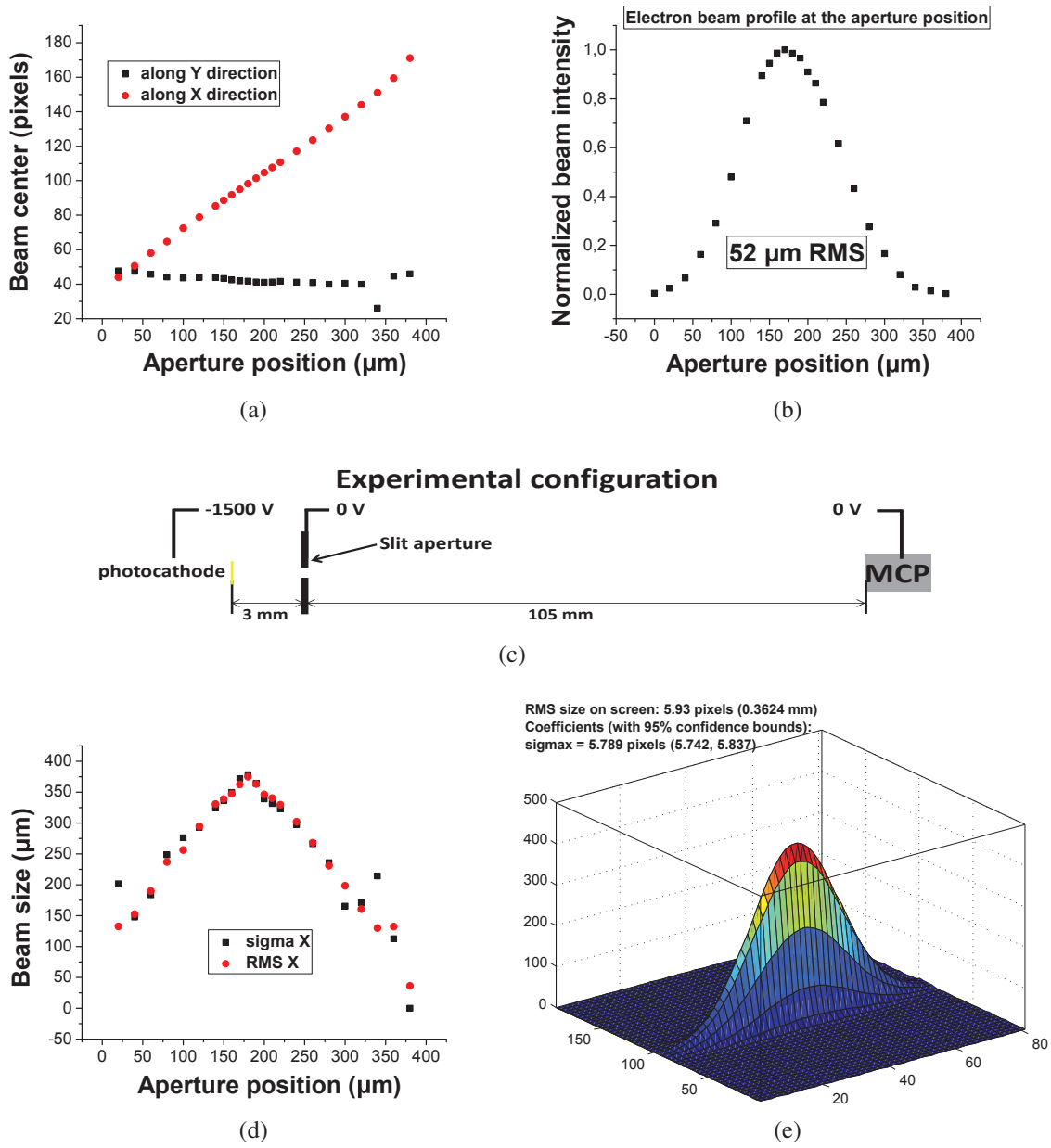

Figure 5.18.: Measurement results for a 100 μm core size solarization resistant optical fiber.(a) Center of the transmitted electron beam (through the aperture slit), at the screen position, as a function of the aperture position; (b) Electron beam profile at the aperture position; (c) Experimental configuration; (d) Size of the transmitted electron beam (through the aperture slit), at the screen position, derived from the 2D Gaussian fit (black squares) and from RMS calculation (red squares); (e) 2D Gaussian fit of the transmitted electron beam where the axes are in pixels and, in the inset, image with the actual transmitted electron beam on the screen

calibrated and then 68% of this was assumed to reach the actual emitter. This percentage was deduced form the optical transmission measurements performed before and shown in figure 5.13 (a). In these conditions, an average emission current between 1 and 8 pA

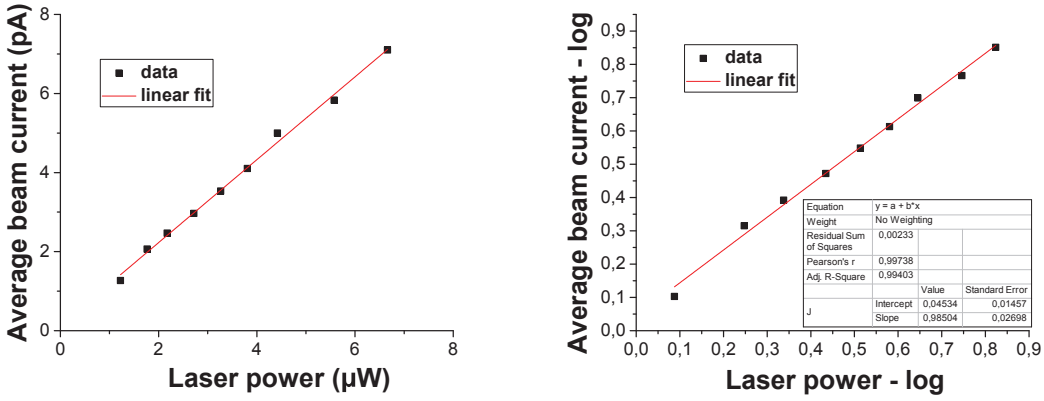

(a) (b)

Figure 5.19.: (a) Measured emission electron current as a function of the laser power (black squares) and linear fit (red); (b) log-log representation of the same data (black squares) and linear fit (red)

was measured, as shown in figure 5.19 (a). Having this new information, the QE of the photocathode, as well as the number of electrons per bunch, were calculated. Using the *QE* formula discussed at the beginning of this chapter (equation 5.2), a QE of $5 \cdot 10^{-6}$ was found. Considering that the emitter layer is Au, this value of *QE* is low. Still, it has to be also taken into account that more than 30% of the optical power reaching the photocathode, will be absorbed by the 3 nm Cr layer. This means that the QE of the *Au* layer alone will actually be higher, on the order of 10^{-5} which is in accordance with the values typically reported in the literature. Regarding the number of electrons per bunch, a value between 8000 and 44000 was calculated considering the 1 kHz repetition rate of the laser.

5.3. Optical fiber-based photocathodes for high electric field applications

As it has been presented in the previous section (5.2), optical fibers can be relatively easily turned into electron sources that could bring important advantages in free electron diffraction setups. Any complications induced by alignment of the optical laser trigger in the center of the photocathode, as well as the control of the laser spot size and shape, are absent when using optical fiber-based photocathodes. They have a predefined and stable emission spot, which can also be adjusted before the experiment within a generous range. Another fact that can be taken advantage of here is the stretching of the laser pulse traveling through the fiber, which is typically significant in the deep UV wavelengths for short laser pulses (on the order of femtoseconds). As normally this could be considered a

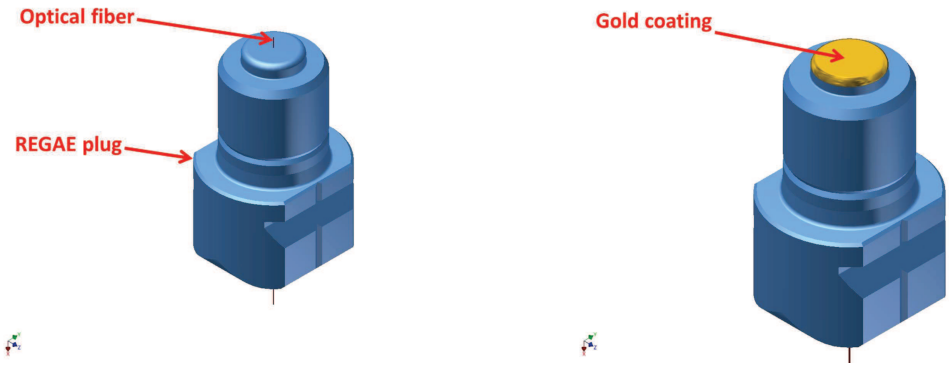

(a) (b)

Figure 5.20.: (a) The standard REGAE plug with the optical fiber fed through its center; (b) The same assembly featuring a Cr/Au coating (after polishing)

drawback, the pulse length of the laser reaching the emission material, can in fact be easily controlled by the length of the fiber. This makes this device ideal for linear accelerators where a RF buncher that can compress the electron pulses is present.

The demand to study thicker samples, has shifted the general interest towards high electric filed linear electron accelerators, where high DC or RF acceleration fields are implied. Inside these setups, the electron beam is accelerated right from the cathode surface, where electric fields of more than $100\,\frac{MV}{m}$ are now possible [10]. Under these conditions, it is critical that the electric filed around the emission region is uniform, fact that is directly dependent on the photocathode shape and the surface quality. In the case of a cut-off metalized optical fiber, sharp edges are present and this will considerably alter the uniformity of the electric field at the cathode surface and could also facilitate the occurrence of electric breakdown, and photocathode damage. Therefore, more advances are required to successfully implement this concept inside RF guns.

Fortunately, this difficulty has also been overcome as a result of the present Ph.D. work. The main idea used is relatively simple, and consists of embedding the fiber-based electron source inside a bulk cathode structure, identical to what is used within conventional RF guns. As the ultimate goal here is to implement this at the Relativistc Electron Gun for Atomic Exploration (REGAE), which has been presented in section 3.4, figure 5.20 presents the concept as applied to a standard REGAE plug. In the first step, a bore is drilled through the large area bulk metallic holder, which in the example of figure 5.20 (a) is the standard REGAE plug. In the second step, the fiber will be fed through the bore, which will have to be just slightly larger than the fiber outer diameter, until it protrudes above the holder surface. In order to mechanically fasten the fiber, a small amount of special vacuum epoxy could be used, or a fiber glue. As this is a totally new approach, different solutions for gluing the fiber have been tried out, and the results are presented below in the body of this section. In the next step, the plug surface will be polished to-

gether with the fiber, until a high quality uniform flat surface is achieved, in the center of which the optical fiber core is situated (figure 5.20 (b)). In the last step, the entire polished surface will be coated with the photocathode metal. While the entire surface of the photocathode will be covered by the emitter metallic layer, photoemission will only be possible from the coating above the fiber core, which will basically act as a back illuminated thin layer photocathode. As stated above, ideally this concept will be implemented at REGAE, where the control of the triggering laser spot size is subject of setup constrains. Unfortunately the process of developing and testing this new device requires beam time, and would involve important technical transformations of the REGAE gun section. The main reason for this is that the current REGAE gun works in a front illumination configuration, as opposed to the fiber-based photocathode. Implementing these modifications would of course cost REGAE important beam time.

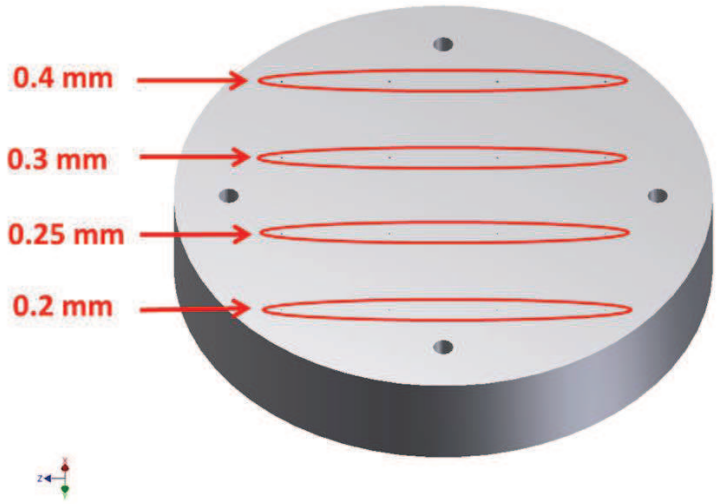

Figure 5.21.: Test holder for the optical fiber-based electron source for high electric field applications

To avoid these complications, a few intermediate steps have been followed to gradually understand and define the design and fabrication procedure of this new concept. First of all, an Aluminum (Al) holder was design with the simple purpose of finding out what is the ideal bore size to be drilled through the center of the standard REGAE plug, so that the fiber can be mechanically attached but also there will not be a large gap around it. Together with this, different types of adhesives were tested. The Al holder features four rows with different bore sizes. On the first row, four bores with a 0.2 mm diameter are placed, this being the smallest bore size that could be drilled at that time. The other three rows feature four bores each, with diameters of 0.25, 0.3 and 0.4 mm respectively, as shown in Figure 5.21. In order to facilitate the mounting and to increase robustness, a special threaded part is fixing the fibers from behind the holder surface (figure 5.22 (b)). First,

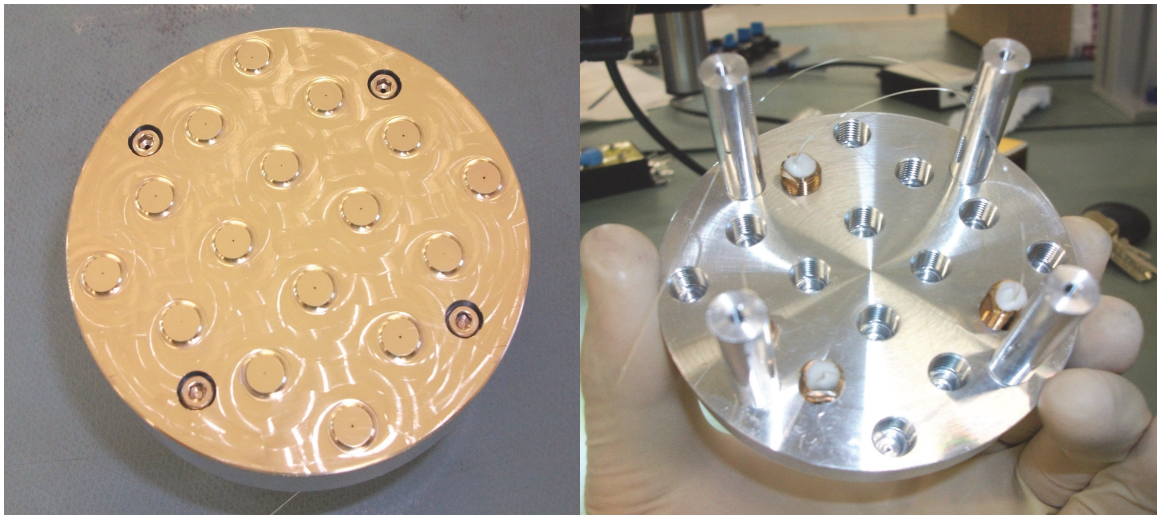

(a) (b)

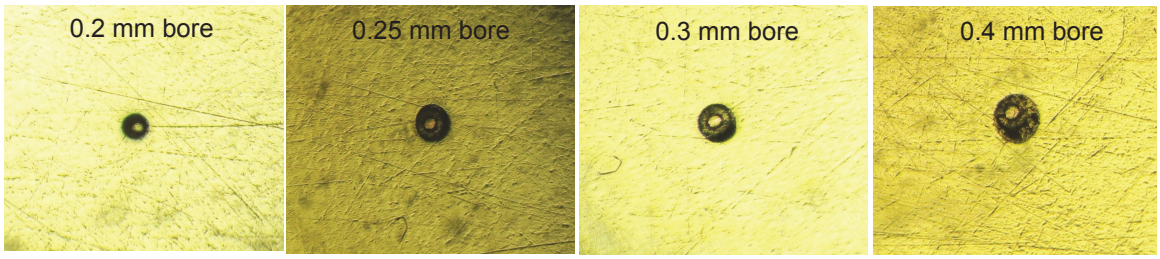

(c)

Figure 5.22.: Fiber holder for high electric field applications (a) view from above and (b) view from below; (c) Optical microscope pictures with each of the four bore sizes (0.2, 0.25, 0.3 and 0.4 mm) after the optical fiber was attached and the surface was polished and Cr/Au coated

the fiber was attached to the threaded part using vacuum epoxy and a sufficient length was left protruding out. Then, a small droplet of Ag paint was applied on the protruding end and then fed through the bore on the main holder, by screwing the two parts together. In the end, the fiber will be sticking above the cathode surface but it will be bounded on both of the two parts, which makes it very robust. The area around it, that is exposed at the holder surface, was then filled with Ag paint, which is also conductive. Four cuts from the same fiber were used for the first test, one for each bore size. After this step was completed, the entire surface was mechanically polished and then Cr/Au coated as shown in figure 5.22 (a). Finally, the resultant structure was inspected under the optical microscope before performing a high voltage test. Figure 5.22 (c) shows the result for each bore size. First conclusion that could be made is that, in case of the largest diameter, the Ag paint does not cover the void around the fiber uniformly. On the other hand, for the smallest diameter, the fiber which was stripped in order to fit inside the 0.2 mm bore, was not centered. The other two sizes seem to work fairly well, the 0.25 mm seeming to be the best size as can provide a slightly better alignment than the 0.3 mm one.

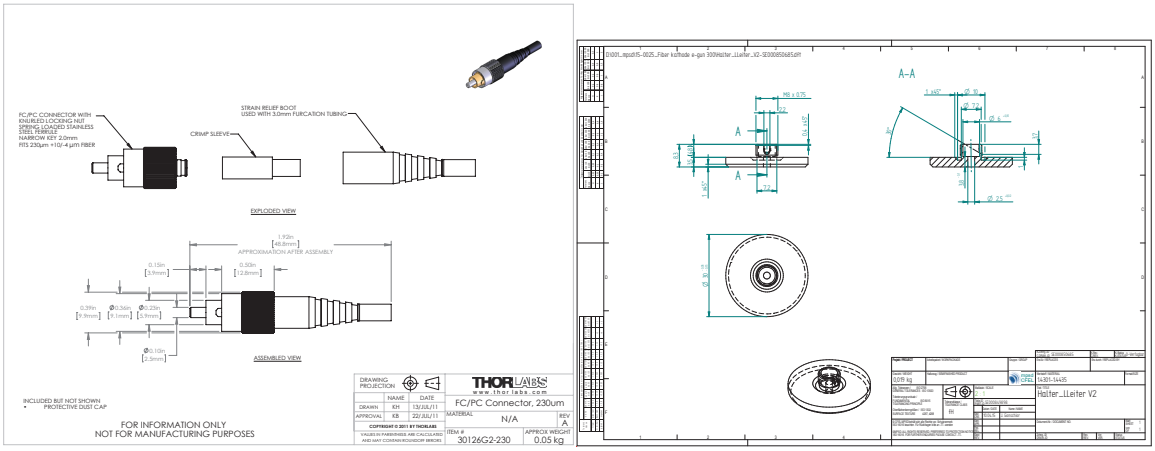

(a) (b)

Figure 5.23.: (a) Thorlabs drawing of the metallic fiber optic connector; (b) Custom designed large area flat photocathode holder, on which the Thorlabs metallic fiber connector can be attached

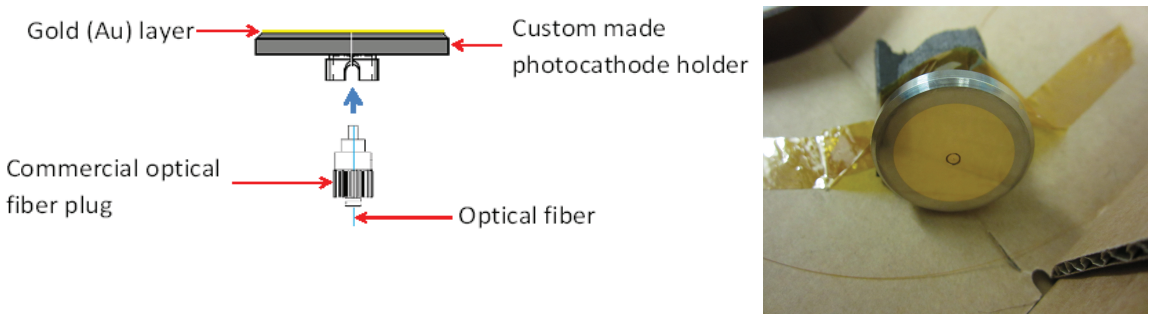

(a) (b)

Figure 5.24.: (a) Sketch of the fiber-based photocathode assembly used for the high electric field photoemission test and (b) a picture with the actual assembly featuring a 25 nm Au layer on top of a 3 nm Cr coating

Before proceeding with the fabrication of the final holder, accordingly to the indications obtained from the previous test, another more inventive and reliable solution was thought off. Basically, instead of using the custom threaded part as before, a standard fiber plug would be more convenient to use as this was specially designed for optical fibers. As represented in figure 5.23 (a), the new idea is based on the use of a commercial metallic fiber plug, purchased from ThorLabs, and a special fiber glue that can be polished by hand, using the same procedure as described in section 3.6. After connectorizing the fiber, the plug on which the fiber is attached, is screwed on a relatively simple custom made part (figure 5.23 b), and the entire structure shown in figure 5.24 is then polished and metalized. Relevant tests that prove the functionality of this new concept will be shown below.

5.3.1. Test using the E-Gun 300

Like it was mentioned before, testing this new concept directly at REGAE was not possible, therefore the *E-Gun 300* [59] was used instead. The maximum acceleration electric field achievable here, around 10 MV/m, is in between the capabilities of the other DC guns used within this Ph.D. work, and REGAE. Therefore, these measurements represent a good preliminary step. Furthermore, a very easy solution was found for mounting the new fiber-based cathode structure inside this gun, which only requires one CF36 flange to be replaced with the special HV fiber feedthrough. The outer diameter of the fiber cathode structure, figure 5.24 (b), was designed to fit inside the standard cylindrical cathode holder present at at *E-Gun 300*. As a lucky coincidence, this holder features a cylindrical hollow structure (figure 5.25) which makes it possible for the fiber to extend from the cathode surface, to the vacuum flange where the fiber feedthrough was mounted.

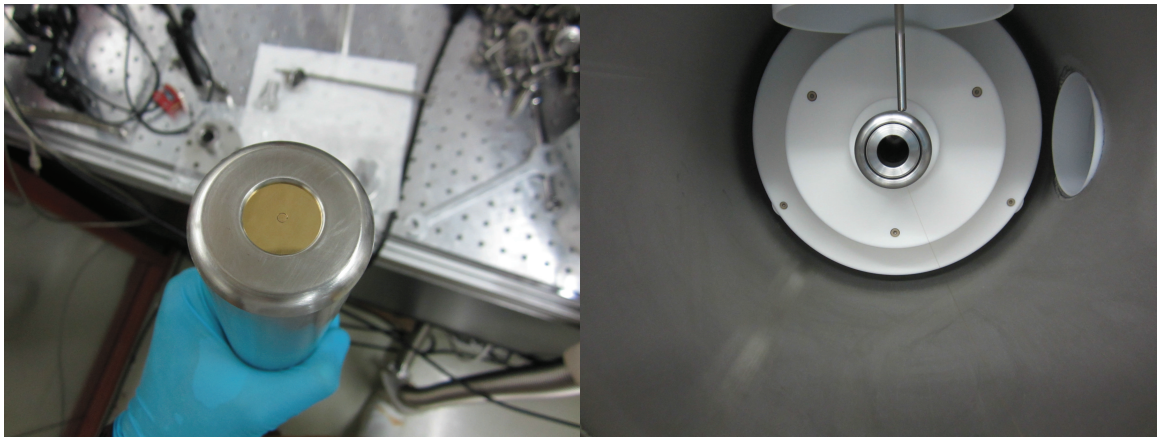

(a) (b)

Figure 5.25.: (a) Picture with the high voltage fiber-based photocathode mounted on the e-gun 300 standard cathode holder; (b) Picture with the gun section of the e-gun 300 setup

Instead of performing a complete test, including vacuum, high voltage and photoemission at the same time, only a simple high voltage test was performed first using an uncoated (but manually polished) high voltage fiber photocathode. The test was successful and a voltage of 80 kV/m, which corresponds to an electric field of 8 MV/m, could be applied after only 2 hours of conditioning.

In the next step, the surface was coated with 2 nm *Cr* and 25 nm *Au* layers, as shown in figure 5.24 (b). Not the whole diameter was covered by the coating because of the holder used in the deposition machine, but the uncoated area will not be exposed to the electric field in the final configuration, as represented in figure 5.25 a). The cathode is fixed from the back using a smaller diameter cylinder which presses around the fiber plug and it is fixed on the other end using a threaded hollow nut. In the next step, the whole

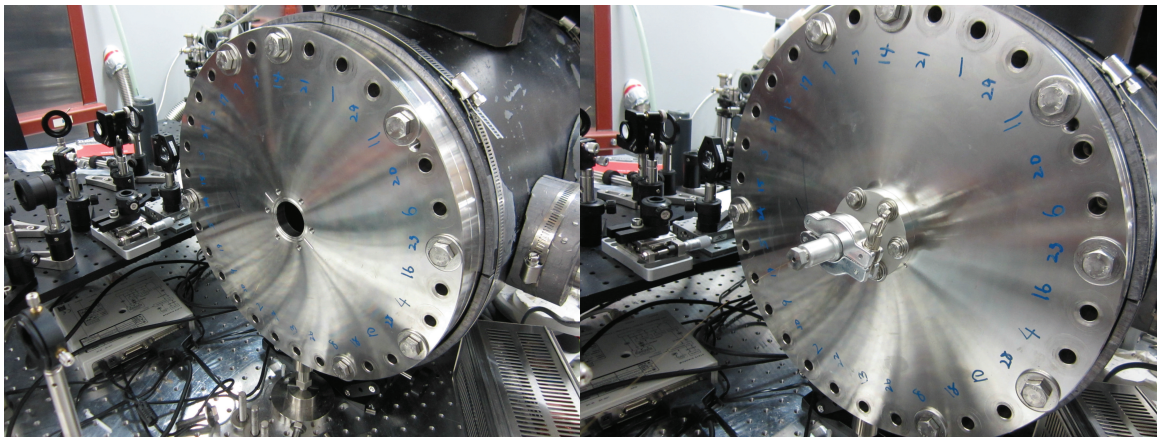

(a) (b)

Figure 5.26.: (a) Picture with the E-gun 300 gun section, after attaching the CF300 vacuum flange, but without the fiber feedhtough and (b) the same as before but with the fiber feedthrough attached. The optical fiber can be also seen coming out of the feedthrough

assembly was inserted inside the gun, made mostly of macor, without any other fixing part to be required. The electrical continuity between the photocathode and the commercial HV feedthrough was assured by a small metallic pipe, situated above the cathode holder cylinder. Figure 5.25 b) depicts the gun after the cathode was inserted, and the fiber can be seen coming out through the back of the cylindrical holder. Then, the CF300 flange that closes the gun section was first fixed to the setup, with the fiber coming out through the uncovered CF36 flange, figure 5.26 a). Next, the fiber feedthrough was connected the last (figure 5.26 b)). After two days of pumping using the 260 l/s turbo pumping system mounted on one of the $CF100$ flanges, a base pressure of 2×10^{-8} mbar was achieved in the gun section. This is good value for this setup, considering the large gun chamber. The voltage test was also successful and again a stable field of about 8 MV/m could be achieved.

For the photoemission test, the same 100 fs pulsed UV (266 nm) laser source, as used for the experiment in section 4.2 was used, and the laser beam path is depicted in the figure 5.27. The maximum input UV laser power used here was $400\,\mu W$, which is larger than in the previous case (section 5.2). The laser beam enters the hutch, which is a radiation shielding led chamber surrounding the *E-gun 300*, through a hole on the left wall, and then it is steered out of the usual path, which would be straight towards the view port, which was now replaced by the fiber feedthrough. Then, it is aligned using two Al mirrors and focused on the fiber plug, mounted on a three axes $nano-maxT5$ positioner, using a 15 cm focal length lens. Similar to the technique used for the low voltage measurements, described in sections 5.1.2 and 5.2, two fiber cuts were used here too. The so called *photocathode fiber* extends from the *extension fiber* (outside the vacuum) to the photocathode which is constituted of its metalized end. The other fiber section, which is named *exten-*

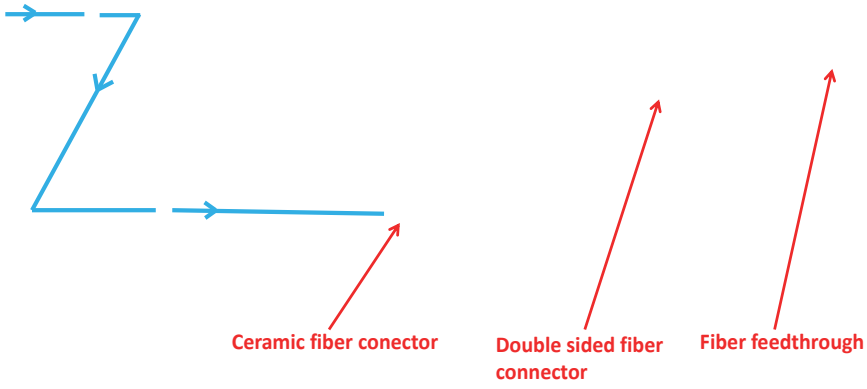

Figure 5.27.: Laser beam path. The UV laser path is controled using two Al coated mirrors before it is coupled into the extension fiber. The connection between the extension and the cathode fiber is achieved using a double-sided fiber coupler

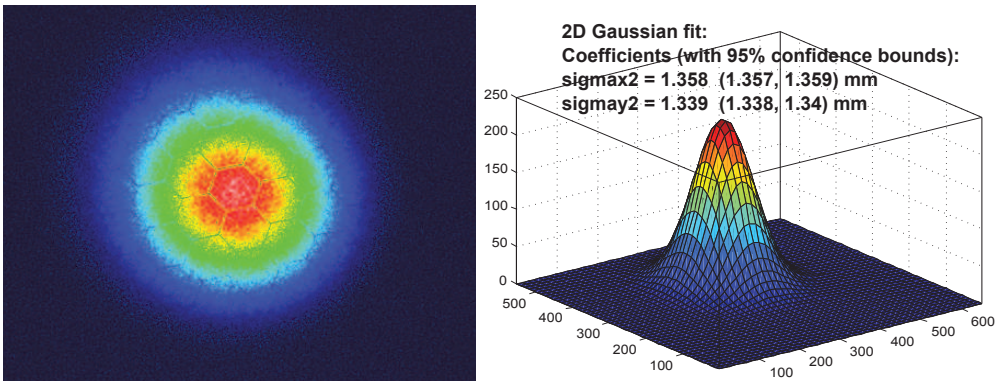

(a) (b)

Figure 5.28.: (a) First electron beam detected at e-gun 300 using a fiber-based photocathode biased to an electric field of 70 kV; (b) 2D Gaussian fit of the electron beam shown in (a)

sion fiber, transports the light from the laser in-coupling on the three axis positioner, to the *photocathode fiber*. Assuming the optical transmission through the *photocathode fiber* to be constant during the measurements (after it was conditioned), which is a fair assumption, the power at the *extension* end can be measured and then the triggering laser power that reaches the emission metal (Au) can be inferred. A CCD camera[11], placed about 60 cm away from the electron source surface was used for detecting the electron beam. Figure 5.28 a) depicts the first electron beam obtained from a *fiber-based photocathode for HV applications* (as shown in figures 5.23 and 5.24), at an acceleration electric field

[11] Princeton Instruments Quad-RO 4320, 24 by 24 μm^2

of 70 kV.

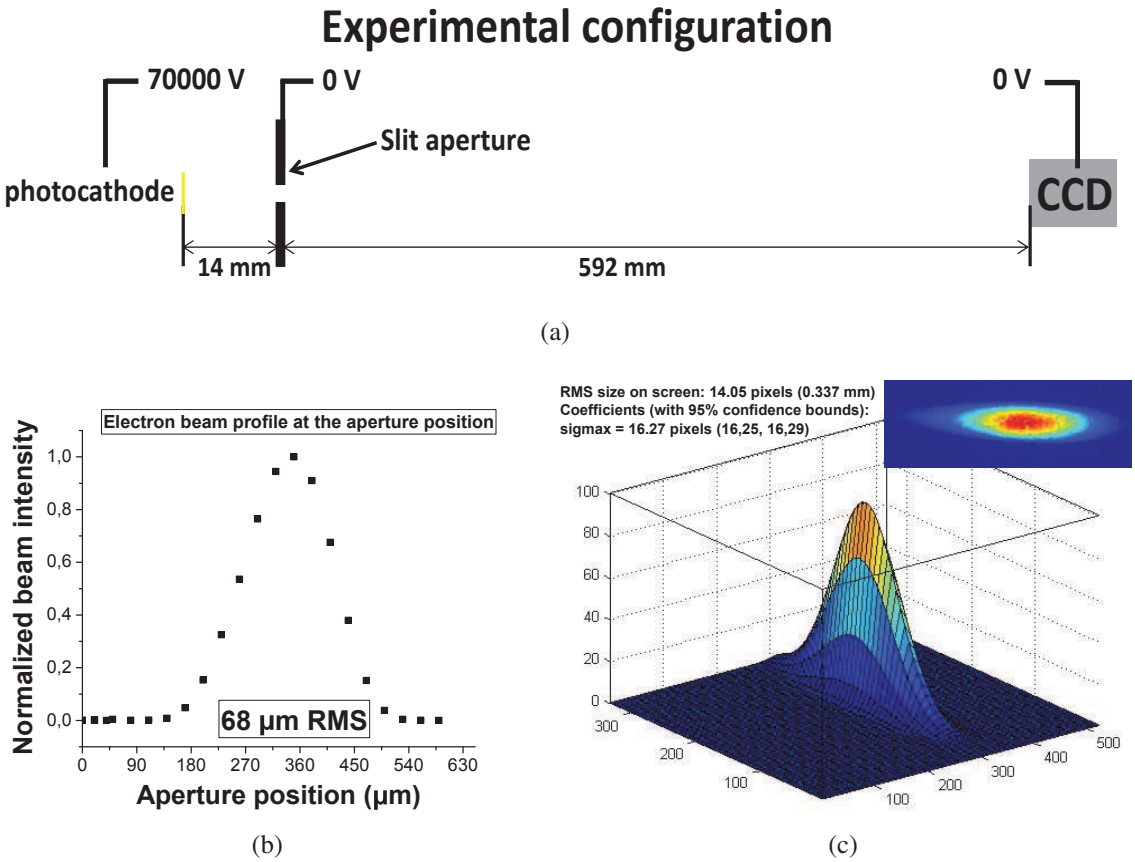

Figure 5.29.: (a) Experimental configuration; (b) Electron beam profile at the aperture position; (c) 2D Gaussian fit of the transmitted electron beam, in the inset, image with the actual transmitted electron beam on the screen

Aperture scan measurements were performed to infer the electron beam emittance of the *fiber-based photocathode for HV applications* as shown in the Figure 5.29. A normalized emittance of $20\,\pi$ nm, and a local angular spread of 0.56 mrad were obtained. This is again corroborating the theoretical expectations. As an emittance of $14\,\pi$ nm was obtained in the low voltage DC gun (up to 3 kV) for the same fiber, a higher value was expected here due to the higher acceleration electric field. This will result in a larger excess energy of the exited electrons, due to the Schottky lowering effect discussed in section 2.1.2, which could induce a change on the normalized emittance of up to 50%, as it was shown for the flat Mo photocathodes in section 4.2.

For comparison, emittance measurements were performed on the same photocathode and on the same setup, using the solenoid scan technique. The methodology was already described theoretically in the chapter 2.4.2 and was applied experimentally in chapter 4.2 on flat Mo photocathodes. In the current case, the normalized emittance at the solenoid was inferred for an acceleration voltage of 70 kV, similar to the case of the

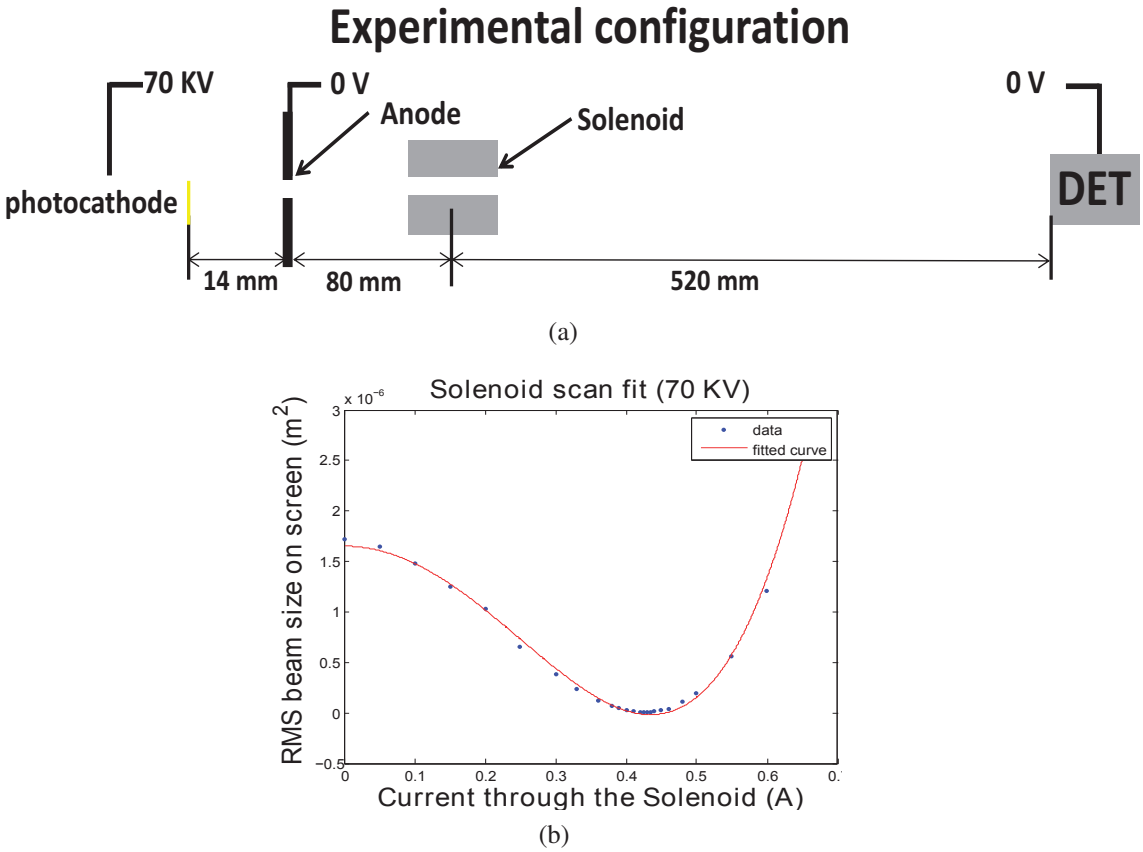

Figure 5.30.: (a) Experimental configuration; (b) The RMS beam size at the screen as a function of the electric current through the solenoid (blue dots) and the fit (red line) with the envelope equation, including only the solenoid and the drift to the screen, at 70kV

aperture scan measurement, which was presented above. For the transfer matrices calculation (section 2.4.2), a free drift region of 520 mm was considered from the solenoid to the screen, as shown in figure 5.30 (a). The solenoid scan fit, plotted in figure 5.30 (b), gave a reasonable value of $26\,\pi$ nm for the normalized emittance $\varepsilon_{n,rms}$. The slight mismatch between the two results, the one obtained with the aperture scan ($20\,\pi$ nm) and the one obtained with the solenoid scan technique ($26\,\pi$ nm), could be due to aberrations induced by the solenoid.

5.4. Two photon photoemission from flat fiber-based electron sources

Single-photon photoemission has been achieved from flat fiber-based electron sources, with emission areas of 50 and 100 μm respectively, as it was presented above in sections 5.2 and 5.3. While a very good emittance, and up to 44000 electrons per bunch were measured, the optical transmission of the multi-mode optical fibers used was very low at the 265 nm laser wavelength, which is a limitation of the maximum achievable emission

current. While the 265 nm laser wavelength was needed to overcome the effective work function of the 30 nm thick Au layer, the use of larger wavelengths could also possibly trigger photoemission via multi-photon excitation processes [71, 80, 81]. This is the case if the triggering laser pulses are short and intense enough, criterias which can be satisfied by the laser source available here. Moreover, besides the fact that the use of wavelengths larger than 300 nm will give a better optical transmission, at these wavelengths single-mode fibers are also available. These fibers have typically core diameters of only a few micrometers, more than one order of magnitude smaller than the multi-mode fibers used above in this chapter. This could considerably reduce the emittance of the emitted electron beam, as discussed in section 2.2.2 and 4.1, and therefore the author considers that the investigation of this aspect is adequate.

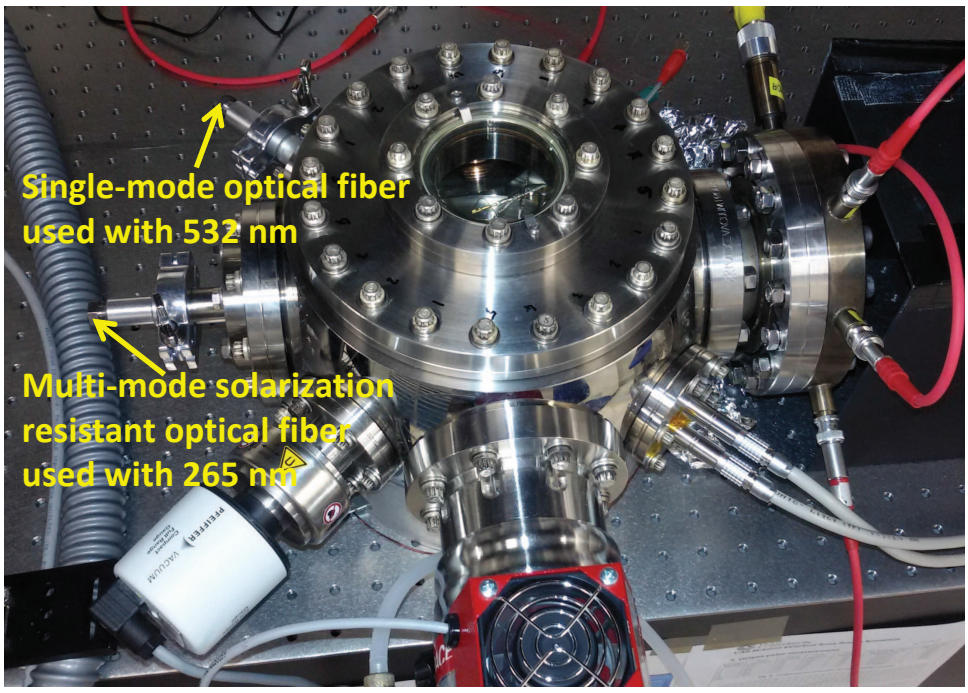

Figure 5.31.: Experimental setup used to test the possibility of two photon photoemission from Cr/Au coated, 3 μm core size single-mode optical fibers. The setup has attached two fiber feedthroughs: one was used for all the measurements presented above in this chapter and a new one which was attached for the use of the single-mode fibers with 532 nm laser wavelength

In the current section, the possibility of two photon photoemission (2PPE) from a 3 μm core diameter single mode optical fiber[12] is discussed. The fiber was prepared in the same way, as described in section 5.2, featuring a 30 nm Au layer on top of a 3 nm Cr layer. The experiment was performed using the same *test* experimental chamber described in sections 3.1, to which an extra fiber feedthrough was attached, as shown in figure 5.31.

[12]Thorlabs product number: SM400

A laser wavelength of 532 nm was used this time (the second harmonic of the available Pharos laser) with 170 fs long pulses, and at a repetition rate of 1 kHz.

Unfortunately, no electron photoemission could be detected up to date for the given configuration. The author considers that this is due to the low laser coupling efficiency into the fiber, combined with the lower emission area (30 time lower than the solarisation resistant fiber) as well as the lower QE for 2PPE processes (single-photon photoemission being not allowed at this large laser wavelength). At this new wavelength (532 nm), an average laser power of more than 500 μW was available at the *extension fiber* input. Still, despite the fact that the optical transmission was constant over time, only 30 μW of the available laser power could be coupled into the single-mode fiber. The low optical coupling efficiency is due to the poor quality of the free propagating laser beam, as well as due to the lack of a suitable fiber collimator, which was not available for the experiment. Considering these aspects, an electron emission current bellow the detection capability of the setup was in fact expected. New optical elements have been ordered to improve the optical coupling efficiency and more measurements will be performed in the near future.

6. Conclusions and outlook

This Ph.D. work represents a contribution to the development and characterization of free electron sources which are at the heart of static and time resolved structural determination techniques. In the course of this work both, setup and electron sources development, as well as measurements have been performed. The author has been intimately involved in experiments performed on setups that were already in the group, the design and development of two new electron guns, and in the fabrication, design and characterization of a number of novel electron sources. The most important achievement of the work presented here, is the development of a new type of electron source which holds a huge potential in the field of electron diffraction techniques: fiber-based electron sources. An enumeration of the main outcomes is given below:

- A low voltage (up to 2.5 kV) electron gun is available for further use in the group. This gun, called the *Test chamber* (section 3.1), was initially designed and used for characterization of single field emitter tips, as was presented in section 4.3. Later on, the setup has been exclusively used for measurements on fiber-based electron sources, which are described in chapter 5;
- The bases of an another new setup have been put together. This electron gun, called the *interferometer* (section 3.2), will be capable of performing electron coherence length measurements by means of interferometry but could also be used for electron diffraction experiments on thin samples. The maximum achievable electron energy is 12 keV;
- A new concept for generating electron beams for diffraction applications has been investigated. This concept is based on the use of a metalized optical fiber and could be used as both, sharp and large area photocathodes as presented in chapter 5. The first implementation of this concept has been achieved as outcome of this current Ph.D. work. While the concept has been proven to not be compatible with CW laser excitation in the case of 100 nm apex size fiber tips, a successful proof-of-principle experiment was performed using femtosecond laser excitation. Single photon photoemission was obtained using 170 fs laser pulses, at 265 nm wavelength and electron beam characterization was

achieved by means of the aperture scan technique. A normalized electron beam emittance of $8.9\,\pi nm$ and $14\,\pi nm$ was measured for a fiber core size of $50\,\mu m$ and $100\,\mu m$ respectively. In addition, an extended design for the use in high electric field environments has been tested for an extraction field of up to 8 MV/m and a normalized electron emittance of $26\,\pi nm$ was measured in this case. As the latter was measured on the same $100\,\mu m$ fiber core size, the larger value of the normalized emittance is expected due to the higher extraction electric field as demonstrated in section 4.2;

- A field emitted current of 125 nA was measured form a single double-gated Mo field-emitter. The measurements were performed in the *Test chamber* (section 3.1) and an original sample holder that allows for biasing single individual tips was developed, as presented in section 4.3 and in the appendix C;
- QE and TE measurements were performed on large area flat Mo photocathodes as a function of the electric field present at the photocathode surface. These measurements were performed on the E-gun 300 (section 3.3) and a QE variation of more than 20% and a TE variation of more than 40% was demonstrated for an electric field variation between 2 and 8 MV/m. Moreover, measurements suggest that photoemission is not only due to single-photon excitation processes, multi-photon photoemission being already present for laser intensities below 46 GW/cm^2, as shown in section 4.2;
- Fabrication of patterned electron sources was investigated. This is based on the fabrication of small area (less than $100\,\mu m$ in diameter) emission sources coated on top of a large area high work function material. Due to the work function difference, emission should only be allowed from the low work function area even when laser excitation spot size is larger than this. Measurements proved a QE ratio of 6.6 between a 100 nm thick Pt layer and a 50 nm thick Au layer. Also, a 50 nm in diameter Au dot was successfully fabricated. Electron emission measurements have not been performed so far;
- An important amount of time was invested by the author in running the Relativistic Electron Gun for Atomic Exploration (REGAE), which is described in section 3.4. Besides performing beamline characterization measurements, the author has gained important experience on static diffraction measurements using the REGAE setup and has been intimately contributed to the first experimental results obtained here, which proved the capability of the setup to solve the structure of up to $1\,\mu m$ thick samples [10];
- Measurements on single crystalline metals have been organized and samples have been purchased. The main advantage of these is the low scattering probability of the excited electrons as well as the absence of randomly orientated grains, which should lead to a better quality of the emitted beam. Three single crystalline Au samples have been purchased and a feasibility report has been written for the experiment (presented in appendix A). Unfortunately, no beam time was available to date on a high resolution photoemission spectrometer, where the energy spread of the electrons emitted from these photocathodes could be measured.

Outlook

- A better characterization of the electron beam emitted from the fiber-based photocathodes is intended by measuring the length of the electron bunches via the streak camera technique;
- More advances are relatively easily possible on the fiber-based photocathode concept. On one hand, the possibility of getting photoemission from fiber tips using pulsed laser sources, which has not been yet investigated, is considered as being feasible and future efforts will be invested in this. Moreover, as discussed in chapter 5, the variation of the tip size (emission area) is possible by the means of cutting techniques or in-house fiber fabrication techniques. At the same time, the possibility of two photon photoemission will be further investigated. This is theoretically possible by using larger laser wavelengths, above 300 nm, which give better optical transmission through the fiber and, at the same time, are compatible with single mode fibers which feature much smaller core sizes. This will eventually inherently reduce the electron emission area, leading to a important reduction of the electron beam emittance. Last, but not the least, new emission materials will be investigated. Lower work function materials, like Mg, can be triggered with laser wavelengths at which a higher optical transmission through the fiber is expected;
- First measurements on the *Interferometer* setup will be soon performed. Once the setup will be up and running, all novel electron sources discussed in the content of this thesis, especially the fiber-based photocathodes, can be investigated. Also, diffractions experiments using this setup are planned.
- More studies on the metal work function dependency on the layer thickness will be performed. This should allow for finding an ideal contrast between the substrate and the emitter material in the case of patterned electron sources discussed in section 4.1. Once the fabrication technique is sorted, first electron beam characterization will be performed. Moreover, these measurements are expected to answer the question whether the thickness of thin metallic layers induce changes in the material work function, or these are due to other factors like surface contamination or the nature of the substrate.
- Two more scientific publications are in progress, including the results presented in chapter 4.2 and chapter 5 respectively. Moreover, a patent application describing the fiber-based photocathode for high electric field applications has been submitted and is currently under review.

The output of the current thesis is very promising, and beyond doubt the results obtained here pave the way to a new generation of diffraction experiments, with capabilities exceeding the limitations faced before.

Appendices

A. Forthcoming measurements: Single crystal Au photocathodes

As it was pointed out in the content of the current thesis, there is a demand to enhance the quality of electron sources for Ultrafast Electron Diffraction (UED) techniques to improving their time resolved capabilities [122]. Due to the large scattering cross section of electrons, good diffraction quality is obtained with a relatively low electron number which makes electron-based techniques an ideal tool for studying relatively thin samples (up to $1\,\mu m$) [10], at competitive costs. In order to obtain constructive Bragg diffraction from the sample under observation, the transverse coherence length of the electron beam has to be comparable to the size of the lattice unit cell (a few tens of nm for proteins). Transverse coherence length measurements reduce to the measure of the beam energy spread σ_{E_x}, or momentum spread σ_{p_x}, at the cathode surface as it is shown in equation A.1 and it was described in the second chapter of this thesis:

$$L_x = \frac{\hbar}{\sigma_{p_x}} \text{ and } \sigma_{p_x} = \sqrt{2 \cdot m \cdot \sigma_{E_x}} \tag{A.1}$$

where L_x is the transverse coherence length, σ_{p_x} is the transverse momentum spread, m is the electron mass and σ_{E_x} is the transverse energy spread at the cathode surface.

Up to date, only a few authors have directly measured the energy spread of photoemitted electron beams at the photocathode surface. A transverse energy spread of 80 meV has been demonstrated recently [67] for 25 nm thin gold (Au) layers. Time of Flight (TOF) techniques have been used to directly measure the longitudinal photoemission spectrum of approximately 10 nm thin Au layers [17] and showed an energy spread of 95 m eV. Also, the transverse thermal emittance of Ag and Cs_2Te photocathodes have been measured using the same technique [43, 123]. The previously measured values correspond to a transverse coherence length L_c of less than a nanometer. Therefore, further improvements are expected in order to achieve protein nanocrystallography capabilities.

Numerous theoretical studies [48,73] predict that the electron beam quality is strongly induced by the mismatch between the energy of the triggering photons and the emitter work function (which is very hard to control in thin films) and by the surface roughness. Also, the dependence of the work function on the crystal orientation has been theoretically discussed recently [54] and the importance of performing photoemission measurements on single crystals has been pointed out. Single crystalline photocathodes offer better surface quality and a well-defined work function, with respect to polycrystalline samples,

which makes them better candidates for this application.

Description of the experiment

The purpose of the current project is to explore the capability of photoemitting highly coherent free electron beams from single crystalline Au samples, with a transverse coherence length on the order of a few tens of nanometers up to 100 nm. These electron sources will be suitable for performing UED experiments on large unit lattice materials such as proteins. Since the technique of producing high surface quality single crystalline Au samples has been improved, very good candidate for next generation of electron sources are available. The very stable work function and surface quality combined with a triggering photon energy that only excites electrons from the Fermi level vicinity should reveal a transverse energy spread comparable to the energy spread of the triggering laser.

Three single crystal Au samples with a purity of 99,999 % and with a size of 10 by 10 by 1 mm are available for these measurements. The samples have the following crystal orientations: (100), (110) and (111), have an orientation accuracy of less than 0.1 degrees and are one side polished with a roughness of less than $0.03\,\mu m$. Given the large dimensions and robustness, they can be easily attached to standard sample holders.

The measurements would consist in recording the photoemission spectra from the three different crystal orientations. The value of interest is the initial transverse energy spread at the photocathode surface which will be used to infer the transverse coherence length of the photoemitted electron beam using equation A.1. Also, if the infrastructure allows, the temperature and the laser polarization dependence on the photoemitted spectra could be also investigated. A capability of detecting electrons with energies of less than 1 eV and with a resolution on the *meV* range is required for this experiment. The required pump wavelength is between 230 and 260 nm for single-photon photoemission measurements and between 470 and 510 nm for two-photon photoemission measurements, depending on the effective work function of the sample which is reported to be between 4.9 and 5.2 eV. The work function depends on the crystal orientation and on the surface quality. An ideal tool for these measurements would be the Angle-Resolved Photoemission Spectroscopy (ARPES) technique which allows for directly measuring photoemission spectra gaining information about both: transverse energy and momentum spread of the emitted electron beam. While finding the suitable setup for these measurements was the main challenge so far, collaborations with other groups might soon offer the possibility for performing these very attractive measurements.

B. Maple code for calculating and plotting emittance using the three-step model for photoemission

```
> restart;
> with(plots) :
>
> #First step in Spicer model (absorbtion of the electrons)
>
> F := E -> 1/(1 + exp((E - EF)/(Kb*T))) : #Fermi-Dirac distribution
>
> ab2 := (1 - F(E + Eph))*F(E) :
    #Probabilitatea ca un electron sa fie excitat de la E la E+Eph depinde de numarul de
    electroni cu energia E si de numarul de stari cu energia E+Eph libere
>
>
> #APROXIMARI si calculul emitantei
>
> #Aproximarea functiei fermi dirac cu Heaviside step function
> NumericEventHandler(invalid_operation = `Heaviside/EventHandler`(value_at_zero = 1/2)) :
                #se asigura ca distributia fermi dirac returneaza valoarea 1/2 cand E = EF
>
> ab2 := (1 - Heaviside(EF - E - Eph))*Heaviside(EF - E) :
    #daca Eph >EF si E<=EF intotdeauna F(E) = H(EF - E) = 1 sau (1/2) si F(E + Eph)
    = H(EF - E - Eph) = 0
>
> sigmpatrat := P[x]^2/(m*c)^2; #Se defineste emitanta dupa aproximarile facute in (X.6.1)
    . Integralele se iau in considerare mai tarziu, iar functia F - D, transformata
    in Heaviside mai sus, da unu deci nu se mai ia in calcul
```

$$sigmpatrat := \frac{P_x^2}{m^2\,c^2} \tag{1}$$

```
> # definirea potentialului pe directie perpendiculara (X.6.2)
> P[x] := sqrt(2*m*(E + Eph))*sin(arccos(y))*cos(Phi) :
>
> emittance1 := int(sigmpatrat, y = y[max]..1, Φ = 0..2*Pi) :
    #se effectueaza integralele dupa cos(theta) si dupa Phi din formula emitantei (numarator)
>
> denominator1 := int(1, y = y[max]..1, Φ = 0..2*Pi) :
    #integralele dupa cos(theta) si dupa Phi de la numitor
> # definirea lui cos(theta)[max] din (X.6.2)
> y := cos(theta) :
```

```
> cos(theta)_max := sqrt((EF + Pieff)/(E + Eph)) :
> emittance2 := int(emittance1, E = EF + Pieff - Eph..EF) :
      #integrala dupa energie de la numarotor din formula emitantei
> denominator2 := int(denominator1, E = (EF + Pieff - Eph)..EF) :
      #integrala dupa energie de la numitor din formula emitantei
>
> emittance := sqrt(simplify((emittance2)/(denominator2))); #formula finala a emitantei
```

$$emittance := \frac{1}{3}\sqrt{3}\sqrt{\frac{-Pieff + Eph}{c^2\, m}} \qquad (2)$$

```
>
> #definirea funtiei de lucru efective (Pieff)
> fischottky := evalf(e·sqrt((e·Fa)/(4·Pi·epsilon))) :      #Bariera Schottky data in Jouli
> Pieff := fim - fischottky :
>
> #se dau valori numerice constantelor
> e := 1.6·10^-19 : epsilon := 8.85·10^-12 : c := 3·10^8 : m := 9.1·10^-31 :
>
> #se dau valori parametrilor materialului
>
> #Fa:=1·10^8 :
      #valoarea campului electric exterior aplicat la suprafata metalului (campul de extractie?
      ) in V | m
>
> EF := 7·e : fim := 4.31·e :
>
> #Pieff:=4.31·e;
> #Eph:=4.86·e;
>
> Eph := EpheV·e : #se transforma energia fotonilor in Jouli
>
> evalf(emittance);
```

$$0.5773502693 \qquad (3)$$

$$\sqrt{-0.000008420024420 + 7.410022131\ 10^{-11}\sqrt{Fa} + 0.000001953601954\ EpheV}$$

```
>
>
>
> #reprezentare grafica
>
> grafic := EpheV→emittance :
>
>
```

```
> Fa := 0 :
> g1 := plot(grafic(EpheV), EpheV = 3.5 ..6, view = [3.5 ..6.5, 0.0 ..0.0012], color = green) :
> Fa :='Fa':

> Fa := 5·10^7 :
> g2 := plot(grafic(EpheV), EpheV = 3.5 ..6, view = [3.5 ..6.5, 0.0 ..0.0012], color = red) :
> Fa :='Fa':

> Fa := 1·10^8 :
> g3 := plot(grafic(EpheV), EpheV = 3.5 ..6, view = [3.5 ..6.5, 0.0 ..0.0012], color = blue) :

> display(g1, g2, g3);
```

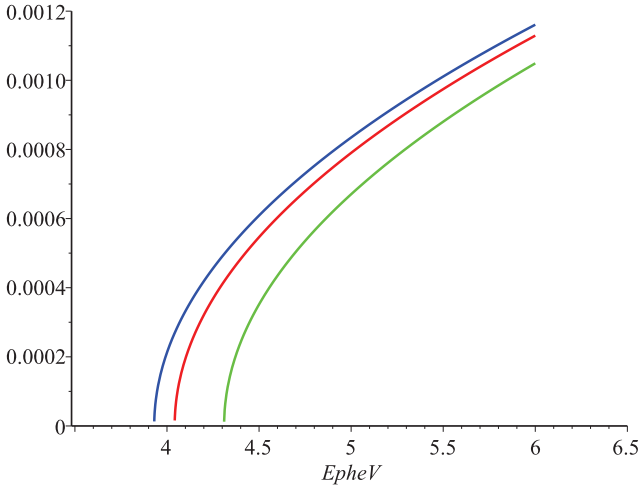

C. FEA sample holder drawings

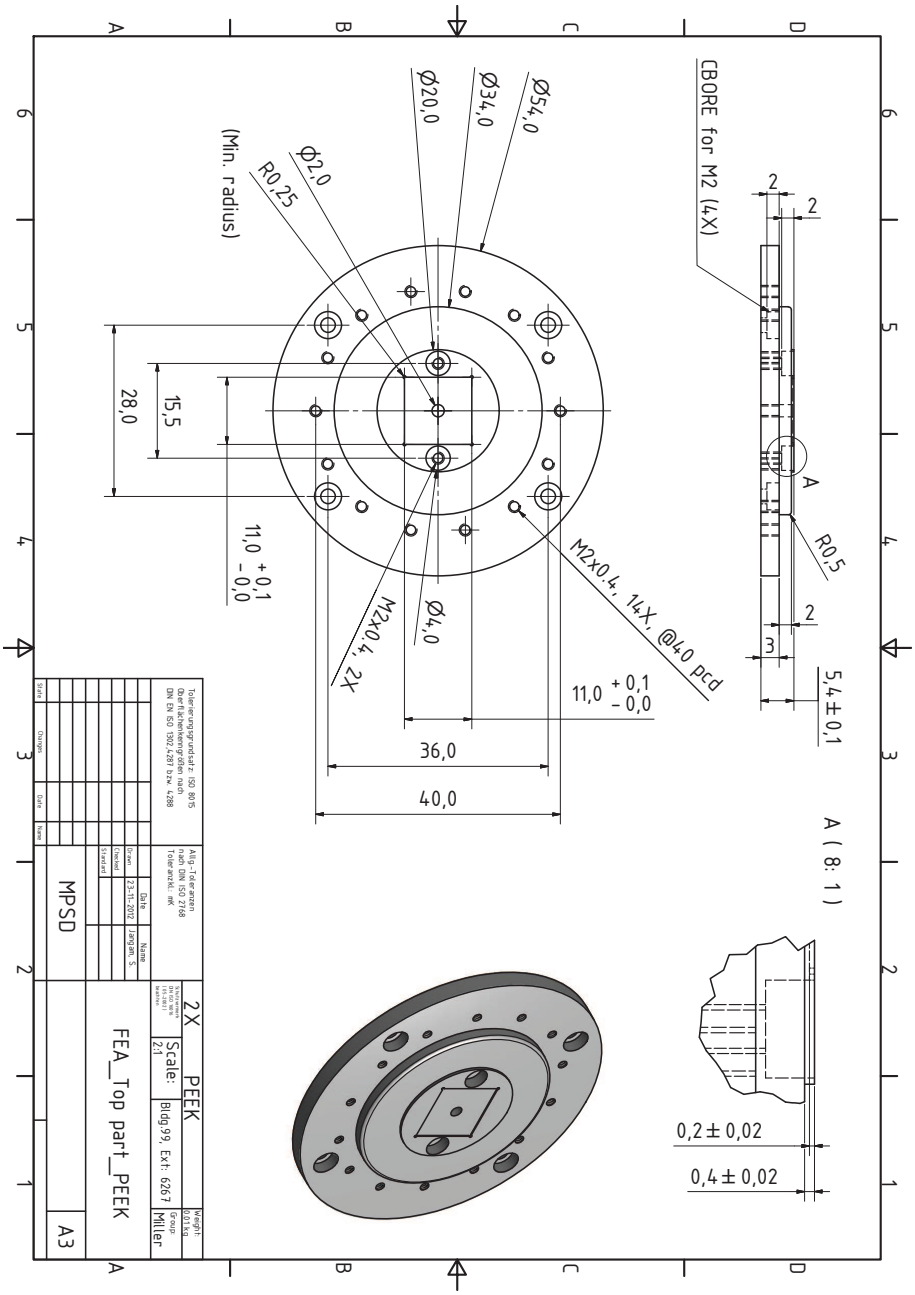

Figure C.1.: Drawings of the FEA sample holder (top part)

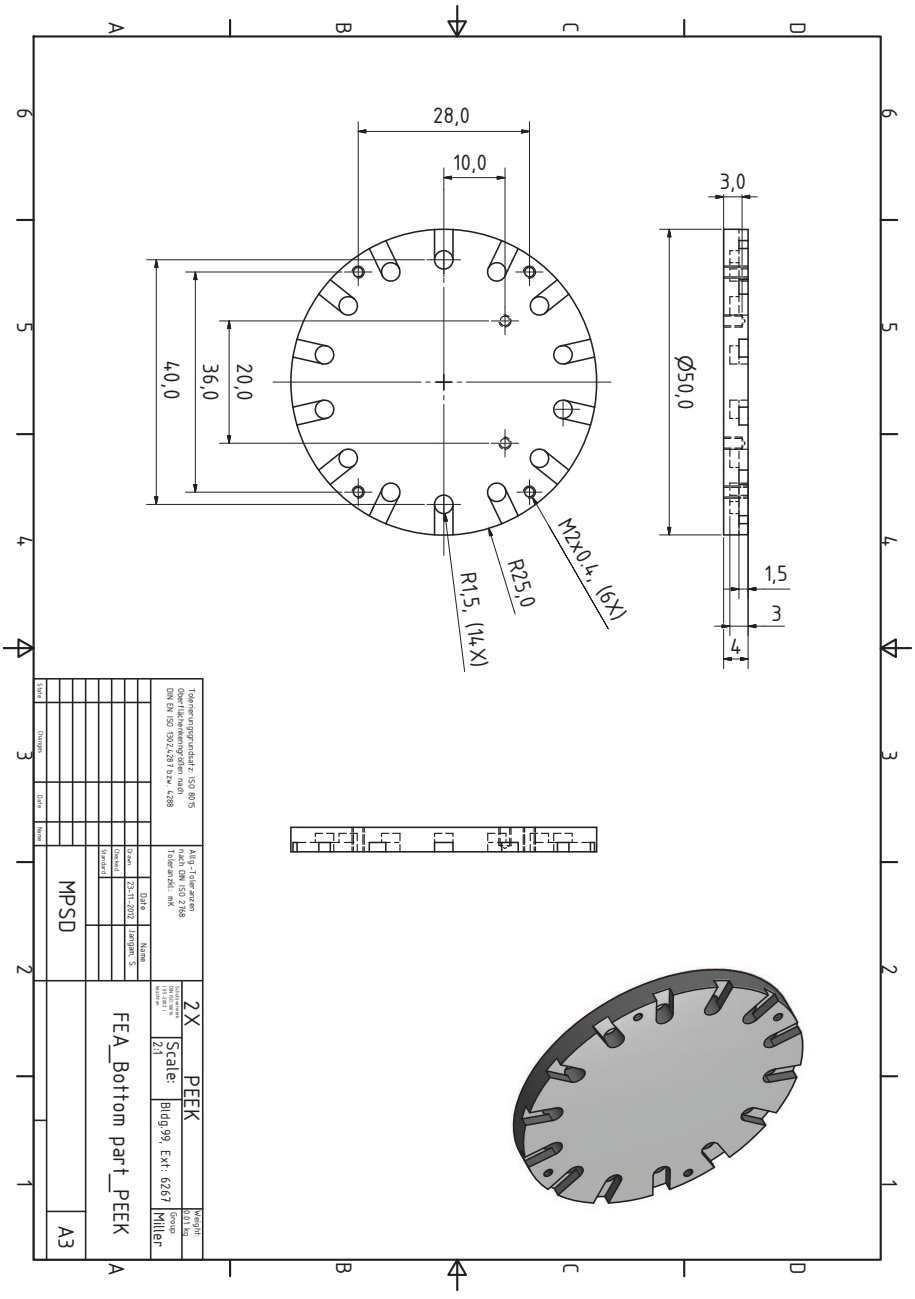

Figure C.2.: Drawings of the FEA sample holder (bottom part)

Contributions of the author

Scientific publications

- *In progress* – Albert Casandruc et al., "*Single photon photoemission results from a fiber-based electron source*";
- *In progress* – Albert Casandruc et al., "*Influence of surface electric field and laser intensity on transverse emittance and quantum efficiency for bulk Mo photocathodes*";
- S. Manz, A. Casandruc, D. Zhang, Y. Zhong, R. a. Loch, A. Marx, T. Hasegawa, L. C. Liu, S. Bayesteh, H. Delsim-Hashemi, M. Hoffmann, M. Felber, M. Hachmann, F. Mayet, J. Hirscht, S. Keskin, M. Hada, S.W. Epp, K. Flöttmann, and R. J. D. Miller, "*Mapping atomic motions with ultrabright electrons: towards fundamental limits in space-time resolution,*" Faraday discussions, Jan. 2015;
- A. Casandruc, G. Kassier, H. Zia, R. Bücker, and R. J. D. Miller, "*Fiber tip-based electron source,*" Journal of Vacuum Science & Technology B, Nanotechnology and Microelectronics: Materials, Processing, Measurement, and Phenomena, vol. 33, p. 03C101, May 2015;
- M. Hada, D. Zhang, A. Casandruc, R. J. D. Miller, Y. Hontani, J. Matsuo, R. E. Marvel, and R. F. Haglund, "*Hot electron injection driven phase transitions,*" Physical Review B, vol. 86, no. 13, p. 134101, 2012;
- Albert Casandruc and Alexandru Stancu, "*Magnetization processes in asymmetric nanometric ferromagnetic disks,*" Journal of Advanced Research in Physics, no. 2, 011109, 2011.

Own poster presentations

- Albert Casandruc, H. Zia, C. Lee, R. Bücker, G. Kassier, R. J. Dwayne Miller, "*Optical fiber-based free electron source,*" presented at the 12th Femtochemistry Conference (FEMTO12), July 2015, Hamburg, Germany;
- Albert Casandruc, Max Hachmann, Günther Kassier, Rolf A. Loch, Dongfang Zhang, Hossein Delsim-Hashemi, Stephanie Manz, Sascha Epp, Klaus Flöttmann and R. J. Dwayne Miller, "*Influence of surface electric field and laser intensity on transverse emittance and quantum efficiency for flat bulk Mo photocathodes,*" presented at the 4th Banff Meeting on Structural Dynamics, February 2015, Banff, Canada;
- Albert Casandruc, Günther Kassier, Haider Zia, Robert Bücker and R. J. Dwayne Miller, "*A novel fiber tip based electron source,*" presented at the 27th International Vacuum Nanoelectronics Conference (IVNC), July 2014, Engelberg, Switzerland;

- Albert Casandruc, Günther Kassier and R. J. Dwayne Miller,"*A state-of-the-art model for calculating the quantum efficiency and the thermal emittance of photoemission in metals,*" presented at the 2nd Banff Meeting on Structural Dynamics, February 2012, Banff, Canada;

Affiliated poster presentations

- Robert Bücker, Albert Casandruc, Chiwon Lee, Philipp Pelz, Haider Zia, Günther Kassier and R. J. Dwayne Miller, "*A testing platform for coherent imaging with ultrabright electron pulses,*" presented at the 12th Femtochemistry Conference (FEMTO12), July 2015, Hamburg, Germany;
- Robert Bücker, Albert Casandruc, Chiwon Lee, Günther Kassier and R. J. Dwayne Miller, "*Interferometric Characterization of High-Brightness Electron Pulse Generation and Propagation,*" presented at the 4th Banff Meeting on Structural Dynamics, February 2015, Banff, Canada;
- Günther Kassier, Albert Casandruc, Robert Bücker, Gustavo Moriena and R. J. Dwayne Miller, "*A 300 kV nanosecond pulsed field emission electron accelerator setup for protein nanocrystallography,*", presented at the 4th Banff Meeting on Structural Dynamics, February 2015, Banff, Canada;
- Robert Bücker, Albert Casandruc, Chiwon Lee, Philipp Pelz, Haider Zia, Gustavo Moriena, Sercan Keskin, Stephanie Manz, Günther Kassier and R. J. Dwayne Miller, "*Imaging, diffraction, and interferometry with ultrabright electron pulses,*" presented at the Deutsche Physikalische Gesellschaft (DPG), March 2014, Dresden, Germany;
- S. Manz, A. Casandruc, D. Zhang, J. Hirscht, S. Bayesteh, S. Keskin, J. Nicholls, T. Gehrke, F. Mayet, M. Hachmann, M. Felber, S. Jangam, H. Delsim-Hashemi, H. Schlarb, M. Hoffmann, M. Hüning, T. Hasegawa, A. Marx, S. Hayes, K. Pichugin, G. Moriena, G. Sciaini, S. Epp, M. Hada, K. Flöttmann and R. J. Dwayne Miller, "*Towards ultrafast electron diffraction and dynamic microscopy with REGAE,*", presented at the 3th Banff Meeting on Structural Dynamics, February 2013, Banff, Canada;
- Kostyantyn Pichugin, Hayes Stuart, Shelley A. Scott, Max G. Lagally, Dongfang Zhang, Julian Hirscht, Albert Casandruc, Masaki Hada, Germán Sciaini, and R. J. Dwayne Miller, "*Structural changes in Si induced via auxiliary layer photoexcitation: A femtosecond electron diffraction study,*" presented at the 3th Banff Meeting on Structural Dynamics, February 2013, Banff, Canada;

Bibliography

[1] R. Thurston, *A History of the Growth of the Steam-Engine*. 1878.

[2] R. Kirby, *Engineering in History*. Courier Dover Publications, 1990.

[3] J. Stewart, *Intermediate Electromagnetic Theory*. World Scientific, 2001.

[4] C. Giacovazzo, D. Viterbo, F. Scordari, G. Gilli, G. Zanotti, and M. Catti, "Fundamentals of Crystallography Edited by," 1992.

[5] J. Miao, P. Charalambous, J. Kirz, and D. Sayre, "Extending the methodology of X-ray crystallography to allow imaging of micrometre-sized non-crystalline specimens," *Nature*, vol. 400, pp. 342–344, 1999.

[6] R. J. D. Miller, R. Ernstorfer, M. Harb, M. Gao, C. T. Hebeisen, H. Jean-Ruel, C. Lu, G. Moriena, and G. Sciaini, "'Making the molecular movie': first frames," *Acta Crystallographica Section A Foundations of Crystallography*, vol. 66, pp. 137–156, feb 2010.

[7] C. Davisson and L. Germer, "Diffraction of electrons by a crystal of Nickel," *Pysical Review*, vol. 30, 1927.

[8] B. J. Siwick, J. R. Dwyer, R. E. Jordan, and R. J. D. Miller, "An Atomic-Level View of Melting Using Femtosecond," *Science*, vol. 43, pp. 3–7, 2003.

[9] G. Sciaini and R. J. D. Miller, "Femtosecond electron diffraction: heralding the era of atomically resolved dynamics," *Reports on Progress in Physics*, vol. 74, p. 096101, sep 2011.

[10] S. Manz, A. Casandruc, D. Zhang, Y. Zhong, R. a. Loch, A. Marx, T. Hasegawa, L. C. Liu, S. Bayesteh, H. Delsim-Hashemi, M. Hoffmann, M. Felber, M. Hachmann, F. Mayet, J. Hirscht, S. Keskin, M. Hada, S. W. Epp, K. Flöttmann, and R. J. D. Miller, "Mapping atomic motions with ultrabright electrons: towards fundamental limits in space-time resolution.," *Faraday discussions*, jan 2015.

[11] W. E. King, G. H. Campbell, A. Frank, B. Reed, J. F. Schmerge, B. J. Siwick, B. C. Stuart, and P. M. Weber, "Ultrafast electron microscopy in materials science, biology, and chemistry," *Journal of Applied Physics*, vol. 97, no. 11, p. 111101, 2005.

[12] G. Campbell, T. LaGrange, W. King, N. Browning, M. Armstrong, J. Kim, B. Reed, A. Frank, B. Stuart, W. DeHope, B. Pyke, R. Shuttlesworth, F. Hartemann, and D. Gibson, "Applying the Dynamic Transmission Electron Microscope to Study Fast Processes in Materials," *Microscopy and Microanalysis*, vol. 12, pp. 1428–1429, jul 2006.

[13] G. Subramanian, S. Basu, H. Liu, J.-M. Zuo, and J. C. H. Spence, "Solving protein nanocrystals by cryo-EM diffraction: multiple scattering artifacts.," *Ultramicroscopy*, vol. 148, pp. 87–93, jan 2015.

[14] H. N. Chapman, A. Barty, M. J. Bogan, S. Boutet, M. Frank, S. P. Hau-Riege, S. Marchesini, B. W. Woods, S. Bajt, W. H. Benner, R. a. London, E. Plönjes, M. Kuhlmann, R. Treusch, S. Düsterer, T. Tschentscher, J. R. Schneider, E. Spiller, T. Möller, C. Bostedt, M. Hoener, D. a. Shapiro, K. O. Hodgson, D. van der Spoel, F. Burmeister, M. Bergh, C. Caleman, G. Huldt, M. M. Seibert, F. R. N. C. Maia, R. W. Lee, A. Szöke, N. Timneanu, and J. Hajdu, "Femtosecond diffractive imaging with a soft-X-ray free-electron laser," *Nature Physics*, vol. 2, pp. 839–843, nov 2006.

[15] Y. Ding, a. Brachmann, F.-J. Decker, D. Dowell, P. Emma, J. Frisch, S. Gilevich, G. Hays, P. Hering, Z. Huang, R. Iverson, H. Loos, a. Miahnahri, H.-D. Nuhn, D. Ratner, J. Turner, J. Welch, W. White, and J. Wu, "Measurements and Simulations of Ultralow Emittance and Ultrashort Electron Beams in the Linac Coherent Light Source," *Physical Review Letters*, vol. 102, p. 254801, jun 2009.

[16] A. H. Zewail, "4D Ultrafast Electron Diffraction, Crystallography, and Microscopy," *Annual Review of Physical Chemistry*, vol. 57, pp. 65–103, may 2006.

[17] A. Janzen, B. Krenzer, O. Heinz, P. Zhou, D. Thien, A. Hanisch, F.-J. Meyer Zu Heringdorf, D. von der Linde, and M. Horn von Hoegen, "A pulsed electron gun for ultrafast electron diffraction at surfaces.," *The Review of scientific instruments*, vol. 78, p. 013906, jan 2007.

[18] S. van der Geer, M. de Loos, J. Botman, O. Luiten, and M. van der Wiel, "Nonlinear electrostatic emittance compensation in kA, fs electron bunches," *Physical Review E*, vol. 65, no. 4, p. 046501, 2002.

[19] T. van Oudheusden, O. Luiten, M. de Loos, and S. van der Geer, "RF Compression of sub-relativistic space-charge- dominated electron bunches for single-shot femtosecond electron diffraction 2011 Particle Accelerator Conference -," pp. 2–3, 2011.

[20] C. Kealhofer, S. M. Foreman, S. Gerlich, and M. a. Kasevich, "Ultrafast laser-triggered emission from hafnium carbide tips," *Physical Review B*, vol. 86, p. 035405, jul 2012.

[21] W. Richardson, *On the negative radiation from hot platinum*. 1901.

[22] H. Welker, "Walter Schottky," *Physics Today*, vol. 29, no. 6, p. 63, 1976.

[23] S. Sze, C. Crowell, and D. Kahng, "Photoelectric Determination of the Image Force Dielectric Constant for Hot electrons in Schottky Barriers," *Journal of Applied Physics*, vol. 35, p. 2534, 1964.

[24] R. Fowler and L. Nordheim, "Electron Emission in Intense Electric Fields," *Proc. R. Soc. London.*, vol. 119, 1928.

[25] E. L. Murphy and R. H. Good, "Thermionic Emission, Field Emission, and the Transition Region," vol. 102, no. 6, 1956.

[26] K. L. Jensen and M. Cahay, "General thermal-field emission equation," *Applied Physics Letters*, vol. 88, no. 15, p. 154105, 2006.

[27] X. He, J. Scharer, J. Booske, and S. Sengele, "One-dimensional combined field and thermionic emission model and comparison with experimental results," *Journal of Vacuum Science & Technology B: Microelectronics and Nanometer Structures*, vol. 26, no. 2, p. 770, 2008.

[28] A. Mustonen, V. Guzenko, C. Spreu, T. Feurer, and S. Tsujino, "High-density metallic nano-emitter arrays and their field emission characteristics," *Nanotechnology*, vol. 25, p. 085203, feb 2014.

[29] K. L. Jensen, "Electron emission theory and its application: Fowler–Nordheim equation and beyond," *Journal of Vacuum Science & Technology B: Microelectronics and Nanometer Structures*, vol. 21, no. 4, p. 1528, 2003.

[30] R. G. Forbes, "Simple good approximations for the special elliptic functions in standard Fowler-Nordheim tunneling theory for a Schottky-Nordheim barrier," *Applied Physics Letters*, vol. 89, no. 11, p. 113122, 2006.

[31] R. G. Forbes and J. H. Deane, "Reformulation of the standard theory of Fowler–Nordheim tunnelling and cold field electron emission," *Proceedings of the Royal Society A: Mathematical, Physical and Engineering Sciences*, vol. 463, pp. 2907–2927, nov 2007.

[32] R. G. Forbes, A. Fischer, and M. S. Mousa, "Improved approach to Fowler–Nordheim plot analysis," *Journal of Vacuum Science & Technology B: Microelectronics and Nanometer Structures*, vol. 31, no. 2, 2013.

[33] J. He, P. H. Cutler, and N. M. Miskovsky, "Generalization of Fowler–Nordheim field emission theory for nonplanar metal emitters," *Applied Physics Letters*, vol. 59, no. 13, p. 1644, 1991.

[34] P. H. Cutler, J. He, M. N. Miskovsky, T. E. Sullivan, and B. Weiss, "Theory of electron emission in high fields from atomically sharp emitters: Validity of the Fowler–Nordheim equation," *Journal of Vacuum Science & Technology B: Microelectronics and Nanometer Structures*, vol. 11, p. 387, mar 1993.

[35] H. Hertz, "Ueber enen Einfluss dess ultravioletten Lichtes auf die electrische Entladung," *Annalen der Physik*, vol. 267, 1887.

[36] J. J. Thomson, "Charge carried by the Cathode Rays," *Philos. Mag.*, vol. 44, p. 293, 1897.

[37] P. Lenard, "Uber die lichtelektrische Wirkung," *Annalen der Physik*, vol. 2, 1900.

[38] J. Maxwell, *A Treatise on Electricity And Magnetism 1873 - Volume 1*. Posner Memorial Collection – Carnegie Mellon University, 1873.

[39] J. Maxwell, *A Treatise on Electricity And Magnetism – Volume 2*. Posner Memorial Collection – Carnegie Mellon University, 1873.

[40] A. Einstein, "Ueber einen die Erzeugung und Verwandlung des Lichtes betreffenden heuristischen Gesichtspunkt," *Annalen der Physik*, vol. 17, pp. 164–181, 1905.

[41] Http://www.nobelprize.org, "The Nobel Prize in Physics 1921," 2015.

[42] S. Humphries, "Charged Particle Beams," 2002.

[43] F. Klaus, "Note on the thermal emittance of electrons emitted by Cessium Telluride photo cathodes," in *TESLA FEL-Report 1997-01*, 1997.

[44] K. Floettmann, "Some basic features of the beam emittance," *Physical Review Special Topics - Accelerators and Beams*, vol. 6, p. 034202, mar 2003.

[45] K. L. Jensen, P. G. O'Shea, D. W. Feldman, and N. a. Moody, "Theoretical model of the intrinsic emittance of a photocathode," *Applied Physics Letters*, vol. 89, no. 22, p. 224103, 2006.

[46] D. H. Dowell, F. K. King, R. E. Kirby, and J. F. Schmerge, "In situ cleaning of metal cathodes using a hydrogen ion beam," *Physical Review Special Topics - Accelerators and Beams*, vol. 9, p. 063502, jun 2006.

[47] K. L. Jensen, W. Dc, D. W. Feldman, E. J. Montgomery, P. G. O. Shea, C. Park, N. A. Moody, L. Alamos, J. Petillo, S. Applications, and I. Corporation, "A THEORETICAL PHOTOCATHODE EMITTANCE MODEL INCLUDING TEMPERATURE AND FIELD EFFECTS *," *Proceedings of PAC07, New Mexico*, pp. 1377–1379, 2007.

[48] D. H. Dowell and J. F. Schmerge, "Quantum efficiency and thermal emittance of metal photocathodes," *Physical Review Special Topics - Accelerators and Beams*, vol. 12, p. 074201, jul 2009.

[49] K. L. Jensen, E. J. Montgomery, D. W. Feldman, P. G. O'Shea, J. R. Harris, J. W. Lewellen, and N. Moody, "Multiple scattering effects on quantum efficiency and response time for cesiated metal photocathodes," *Journal of Applied Physics*, vol. 110, no. 3, p. 034504, 2011.

[50] T. Vecchione, I. Ben-Zvi, D. H. Dowell, J. Feng, T. Rao, J. Smedley, W. Wan, and H. a. Padmore, "A low emittance and high efficiency visible light photocathode for high brightness accelerator-based X-ray light sources," *Applied Physics Letters*, vol. 99, no. 3, p. 034103, 2011.

[51] S. E. Laboratories, "Photoemission Studies of Copper and Silver: Theory," *Physical Review*, vol. 136, no. 4 A, 1964.

[52] W. F. Krolikowski and W.E. Spicer, "Photoemission studies of the Noble Metals. I. Copper*," vol. 185, no. 3, 1969.

[53] J. R. Maldonado, P. Pianetta, D. H. Dowell, J. Corbett, S. Park, J. Schmerge, A. Trautwein, and W. Clay, "Experimental verification of the 3-step model of photoemission for energy spread and emittance measurements of copper and CsBr-coated copper photocathodes suitable for free electron laser applications," *Applied Physics Letters*, vol. 101, no. 23, p. 231103, 2012.

[54] B. Rickman, J. Berger, a. Nicholls, and W. Schroeder, "Intrinsic Electron Beam Emittance from Metal Photocathodes: The Effect of the Electron Effective Mass," *Physical Review Letters*, vol. 111, p. 237401, dec 2013.

[55] M. Hachmann, "Transverse emittance measurement at REGAE via a solenoid scan," Tech. Rep. November, 2012.

[56] I. Bazarov, L. Cultrera, A. Bartnik, B. Dunham, S. Karkare, Y. Li, X. Liu, J. Maxson, and W. Roussel, "Thermal emittance measurements of a cesium potassium antimonide photocathode," *Nuclear Instruments and Methods in Physics Research Section A*, vol. 519, pp. 432–441, may 2004.

[57] M. Reiser, *Theory and Design of Charged Particle Beams*. 2008.

[58] Y. Zou, H. Li, M. Reiser, and P. O'Shea, "Theoretical study of transverse emittance growth in a gridded electron gun," *Nuclear Instruments and Methods in Physics Research Section A: Accelerators, Spectrometers, Detectors and Associated Equipment*, vol. 519, pp. 432–441, feb 2004.

[59] D. Zahng, *Femtosecond Structural Dynamics on the Atomic Length Scale*. PhD thesis, 2013.

[60] S. Bayesteh, *Transverse electron beam diagnostics at REGAE*. PhD thesis, 2014.

[61] A. D. Cronin and B. McMorran, "Electron interferometry with nanogratings," *Physical Review A*, vol. 74, p. 061602, dec 2006.

[62] B. McMorran and A. D. Cronin, "Model for partial coherence and wavefront curvature in grating interferometers," *Physical Review A*, vol. 78, p. 013601, jul 2008.

[63] B. Mcmorran, *Electron Diffraction and Interferometry Using Nanostructures by*. PhD thesis, 2009.

[64] Http://www.princetoninstruments.com, "Quad-Ro 4320 CCD camera," 2015.

[65] Http://www.krelltech.com, "Bare fiber polishing machine," 2015.

[66] F. Pimpec, C. J. Milne, C. P. Hauri, and F. Ardana-Lamas, "Quantum efficiency of technical metal photocathodes under laser irradiation of various wavelengths," *Applied Physics A*, vol. 112, pp. 647–661, feb 2013.

[67] H. Kassier, *Ultrafast Electron Diffraction: Source Development, Diffractometer Design and Pulse Characterisation*. PhD thesis, 2010.

[68] F. O. Kirchner, S. Lahme, K. F, and B. P, "Coherence of femtosecond single electrons exceeds biomolecular dimensions," *New Journal of Physics*, vol. 15, 2013.

[69] D. E. Eastman, "Photoelectric work functions of transition, rare-earth, and noble metals," vol. 2, 1970.

[70] Http://refractiveindex.info, "Refractive Index Info," 2015.

[71] R. Brogle, P. Muggli, P. Davis, G. Hairapetian, and C. Joshi, "Studies of Linear and Nonlinear Photoelectric Emission for Advanced Accellerator Applications," in *Institute of Electrical and Electronics Enfineers*, 1996.

[72] C. P. Hauri, R. Ganter, F. Le Pimpec, a. Trisorio, C. Ruchert, and H. H. Braun, "Intrinsic Emittance Reduction of an Electron Beam from Metal Photocathodes," *Physical Review Letters*, vol. 104, p. 234802, jun 2010.

[73] J. F. Schmerge, J. E. Clendenin, D. H. Dowell, and S. M. Gierman, "RF Gun Photo-Emission Model for Metal Cathodes Including Time Dependent Emission," *International Journal of Modern Physics A*, vol. 22, no. 23, 2007.

[74] R. K. Li, P. Musumeci, H. a. Bender, N. S. Wilcox, and M. Wu, "Imaging single electrons to enable the generation of ultrashort beams for single-shot femtosecond relativistic electron diffraction," *Journal of Applied Physics*, vol. 110, no. 7, p. 074512, 2011.

[75] L. Faillace, "Recent Advancements of RF Guns," in *Physics and Applications of High Brightness Beams – Towards a Fifth Generation light source, San Juan, Puerto Rico*, 2013.

[76] H. B. Michaelson, "The work function of the elements and its periodicity," *Journal of Applied Physics*, vol. 48, p. 4729, 1977.

[77] J. F. Schmerge, J. M. Castro, J. E. Clendenin, D. H. Dowell, S. M. Gierman, R. O. Hettel, and M. Park, "Emittance and Quantum Efficiency Measurements from a 1.6 Cll S-Band Photocathode RF Gun With Mg Cthode," in *Proceedings of the 2004 FEL Conference*, pp. 205–208, 2004.

[78] D. Dowell, P. Bolton, J. Clendenin, P. Emma, S. Gierman, W. Graves, C. Limborg, B. Murphy, and J. Schmerge, "Slice emittance measurements at the SLAC gun test facility," *Nuclear Instruments and Methods in Physics Research Section A: Accelerators, Spectrometers, Detectors and Associated Equipment*, vol. 507, pp. 327–330, jul 2003.

[79] A. Tron and T. Gorlov, "Photocathode Roughness Impact On Photogun Beam Characteristics," in *Proceedings of EPAC 2006, Edinburgh, Scotland*, pp. 121–123, 2006.

[80] A. Kaiser and C. Garrett, "Two-Photon Excitation in CaF2:EU2+," *Physical Review Letters*, vol. 7, no. 6, pp. 229–232, 1961.

[81] S. D. Moustaizis, M. Tatarakis, C. Kalpouzos, and C. Fotakis, "High current and directional electron beams produced from gold photocathodes by ultrashort excimer laser pulses," *Applied Physics Letters*, vol. 60, no. 16, p. 1939, 1992.

[82] P. Liu, Y. Wei, K. Liu, L. Liu, K. Jiang, and S. Fan, "New-type planar field emission display with superaligned carbon nanotube yarn emitter.," *Nano letters*, vol. 12, pp. 2391–6, may 2012.

[83] T. F. Teepen, a. H. V. van Veen, H. van't Spijker, S. W. H. K. Steenbrink, a. van Zuuk, C. T. H. Heerkens, M. J. Wieland, N. J. van Druten, and P. Kruit, "Fabrication and characterization of p-type silicon field-emitter arrays for lithography," *Journal of Vacuum Science & Technology B: Microelectronics and Nanometer Structures*, vol. 23, no. 2, p. 359, 2005.

[84] Y. Tanaka, H. Miyashita, M. Esashi, and T. Ono, "An optically switchable emitter array with carbon nanotubes grown on a Si tip for multielectron beam lithography.," *Nanotechnology*, vol. 24, p. 015203, jan 2013.

[85] M. Nagao, T. Yoshida, S. Kanemaru, Y. Neo, and H. Mimura, "Fabrication of a Field Emitter Array with a Built-in Einzel Lens," *Japanese Journal of Applied Physics*, vol. 48, p. 06FK02, jun 2009.

[86] P. Helfenstein, K. Jefimovs, E. Kirk, C. Escher, H.-W. Fink, and S. Tsujino, "Fabrication of metallic double-gate field emitter arrays and their electron beam collimation characteristics," *Journal of Applied Physics*, vol. 112, no. 9, p. 093307, 2012.

[87] P. Helfenstein, A. Mustonen, T. Feurer, and S. Tsujino, "Collimated Field Emission Beams from Metal Double-Gate Nanotip Arrays Optically Excited via Surface Plasmon Resonance," *Applied Physics Express*, vol. 6, p. 114301, 2013.

[88] S. Tsujino, S. Member, P. Helfenstein, E. Kirk, T. Vogel, C. Escher, and H.-w. Fink, "Field-Emission Characteristics of Molded Molybdenum Nanotip Arrays With Stacked Collimation Gate Electrodes," *Electron Device Letters, IEEE*, vol. 31, no. 9, pp. 1059–1061, 2010.

[89] P. Helfenstein, E. Kirk, K. Jefimovs, T. Vogel, C. Escher, H.-W. Fink, and S. Tsujino, "Highly collimated electron beams from double-gate field emitter arrays with large collimation gate apertures," *Applied Physics Letters*, vol. 98, no. 6, p. 061502, 2011.

[90] A. Mustonen, P. Beaud, E. Kirk, T. Feurer, and S. Tsujino, "Five picocoulomb electron bunch generation by ultrafast laser-induced field emission from metallic nano-tip arrays," *Applied Physics Letters*, vol. 99, no. 10, p. 103504, 2011.

[91] W. S. Graves, F. X. Kärtner, D. E. Moncton, and P. Piot, "Intense Superradiant X Rays from a Compact Source Using a Nanocathode Array and Emittance Exchange," *Physical Review Letters*, vol. 108, p. 263904, jun 2012.

[92] P. D. Kanungo, P. Helfenstein, V. A. Guzenko, C. Lee, and S. T. S. Member, "Pulsed field emission imaging of double-gate metal nano-tip arrays : impact of emission current and noble gas conditioning," in *27th IVNC Conference*, vol. 3, pp. 1–2, 2014.

[93] J. Hecht, *City of Light : The story of fiber optics*. Oxford university press, 1999.

[94] The Class for Physics of the Royal Swedish Academy of Sciences, "Scientific Background on the Nobel Prize in Physics 2009: Two revolutionary optical technologies," 2009.

[95] "A flexible fibrescope, using Static Scanning," *Nature*, vol. 173, no. 39 - 41, 1954.

[96] E. Snitzer, "Cylindrical dielectric waveguide modes," *Journal of the Optical Society of America*, vol. 51, no. 5, 1961.

[97] K. C. Kao and T. W. Davies, "Spectrophotometric studies of ultra low loss optical glasses I : single beam method," *Journal of Scientific Instruments*, vol. 1, no. 2, 1968.

[98] H. Bennett and R. Forman, "Absorption coefficients in highly transparent solids: barothermal theory for cylindrical configurations.," *Applied optics*, vol. 14, pp. 3031–7, dec 1975.

[99] B. Hecht, B. Sick, U. P. Wild, V. Deckert, R. Zenobi, O. J. F. Martin, and D. W. Pohl, "Scanning near-field optical microscopy with aperture probes: Fundamentals and applications," *The Journal of Chemical Physics*, vol. 112, no. 18, p. 7761, 2000.

[100] L. Lereu, A. Passian, and P. Dumas, "Near field optical microscopy: A brief review," *International Journal of Nanotechnology*, vol. 9, no. 3/4/5/6/7, p. 488, 2012.

[101] E. Synge, "A suggested method for extending microscopic resolution into the ultramicroscopic region," *The London, Edinburgh, and Dublin Philosophical Magazine and Journal of Science*, vol. 6, pp. 356–362, apr 1928.

[102] A. Lewis, M. Isaacson, A. Harootunian, and A. Muray, "Development of 500 angstrom spatial resolution light microscope," *Ultramicroscopy*, vol. 13, pp. 227–232, 1984.

[103] A. Muray, M. Isaacson, I. Adesida, and B. Whitehead, "Fabrication of apertures, slots, and grooves at the 8–80 nm scale in silicon and metal films," *Journal of Vacuum Science & Technology B: Microelectronics and Nanometer Structures*, vol. 1, no. 4, p. 1091, 1983.

[104] M. Schmitt, *Feldunterstutzte Photoelektronenemission*. PhD thesis, Univerity of Darmstadt, 1998.

[105] T. Vecchione, U. Weierstall, C. Edgcombe, and J. Spence, "Monchromatic Photo-Field Electron Emission Sources," *Microsc. Microanal*, vol. 12, p. 146, 2006.

[106] J. Spence, T. Vecchione, and U. Weierstall, "A coherent photofield electron source for fast diffractive and point-projection imaging," *Philosophical Magazine*, vol. 90, pp. 4691–4702, dec 2010.

[107] D. R. Turner, "United States Patent Number: 4469554," 1984.

[108] R. Kazinczi, E. Szocs, E. Kalman, and P. Nagy, "Novel methods for preparing EC STM tips," *Applied Physics A*, vol. 66, pp. 535–538, 1998.

[109] P. Uebel, S. T. Bauerschmidt, M. A. Schmidt, and P. St. J. Russell, "A gold-nanotip optical fiber for plasmon-enhanced near-field detection," *Applied Physics Letters*, vol. 103, p. 021101, 2013.

[110] Http://www.nanonics.co.il, "A comparison of existing NSOM/SNOM technologies," 2015.

[111] S. Gierman, P. Bolton, J. Corbett, G. Hays, F. King, R. Kirby, J. Schmerge, and J. Sebek, "Operating A Tungsten Dispenser Cathode In Photo-Emission Mode*," in *Proceedings of PAC09, Vancouver, BC, Vanada*, pp. 575–576, 2010.

[112] R. Fowler and L. Nordheim, "Electron Emission in Intense Electric Fields," *Proceedings of the Royal Society of London, Series A*, vol. 119, no. 781, pp. 173–181, 1928.

[113] R. Kitamura, L. Pilon, and M. Jonasz, "Optical constants of silica glass from extreme ultraviolet to far infrared at near room temperature," *Applied Optics*, vol. 46, p. 8118, nov 2007.

[114] K. L. Jensen, "General formulation of thermal, field, and photoinduced electron emission," *Journal of Applied Physics*, vol. 102, no. 2, p. 024911, 2007.

[115] P. Karlitschek, G. Hillrichs, and K. Klein, "Influence of hydrogen on the colour center formation in optical fibers induced by pulsed UV-laser radiation . Part 1 :

all silica fibers with high-OH undoped core," *Optics Communications*, vol. 155, pp. 376–385, 1998.

[116] P. Karlitschek, G. Hillrichs, and K. Klein, "Influence of hydrogen on the colour center formation in optical fibers induced by pulsed UV-laser radiation . Part 2 : All-silica fibers with low-OH undoped core," *Optics Communications*, vol. 155, pp. 386–397, 1998.

[117] L. Skuja, H. Hosoflo, M. Hiranob, and S. Si, "Laser-induced color centers in silica Nd 2nd," in *Proceedings of SPIE*, vol. 4347, pp. 155–168, 2001.

[118] K.-F. Klein, C. P. Gonschior, D. Beer, H.-S. Eckhardt, M. Belz, J. Shannon, V. Khalilov, M. Klein, and C. Jakob, "Silica-based UV-fibers for DUV applications: current status," in *Proceedings of SPIE* (K. Kalli, J. Kanka, and A. Mendez, eds.), vol. 8775, p. 87750B, may 2013.

[119] T. a. Birks, J. C. Knight, and P. S. Russell, "Endlessly single-mode photonic crystal fiber," *Optics Letters*, vol. 22, p. 961, jul 1997.

[120] N. Yamamoto, L. Tao, and a. P. Yalin, "Single-mode delivery of 250 nm light using a large mode area photonic crystal fiber.," *Optics express*, vol. 17, pp. 16933–40, sep 2009.

[121] Y. Colombe, D. H. Slichter, A. C. Wilson, D. Leibfried, and D. J. Wineland, "Single-mode optical fiber for high-power, low-loss UV transmission," *arXiv*, vol. 1579, p. 11, may 2014.

[122] D. H. Dowell, I. Bazarov, B. Dunham, and K. Harkay, "Cathode R & D for Future Light Sources," in *Workshop on Accelerator R & D for Future Light Sources*, pp. 1–26, 2010.

[123] D. Sertore, D. Favia, P. Michelato, L. Monaco, and P. Pierini, "Cesium Telluride and Metals Photoelectron Thermal Emittance Measurements Using A Time-Of-Flight Spectrometer," in *Proceedings of EPAC 2004, Lucerne, Switzerland*, vol. 2, pp. 408–410, 2004.

Acknowledgements

Nothing of these would have been possible without my parents who have initially guided me towards an academic career and made unmeasurable efforts to financially support me in the early stage. Incommensurable thanks to them and my younger brother, whom I could only visit very seldom during this Ph.D period, but who have always given me the freedom I needed and put so much trust in me. Special thanks to my wife who, despite the fact that we broke up more than a year ago, during our time together she always helped me to improve by indirectly challenging me with everything she was doing better.

I would like to gratefully acknowledged professor R. J. Dwayne Miller for giving me the opportunity to work in an extremely valuable environment and granted me the access to state-of-the-art scientific instruments who were compulsory for the success of this work. My deepest appreciation to G*ü*nther Kassier for guiding me from the beginning of this Ph.D. work and for also being a best friend during all these years. Sincere thanks to Robert B*ü*cker for being always right and for the precious and meticulous guidance in scientific writing and to Zia Haider for introducing me to the filed of optical fibers. Thank you all for your friendship, guidance and support.

Also, the help of the following people is highly acknowledged:

The REGAE team members Stephanie Manz, Sascha Epp, Klaus Floettmann, Sercan Keskin, Rolf Loch, Julian Hirscht, Alexander Marx, Dongfang Zahng, Yingpeng Zhong, Hossein Delsim-hashemi, Shima Bayesteh, Masaki Hada, Matthias Hoffmann, Matthias Felber, Frank Mayet, Max Hachmann, Michael Seebach and Sven Lederer who have been working with me at REGAE and have giving me unconditional support.

Miriam Barthelmess and Professor Henry Chapman for granting the access to their e-beam deposition machine, Professor Franz Kärtner for grantig the access to his bare fiber polishing, Djordje Gitaric, Josef Gonschior, Carsten Meklenburg and Santosh Jangam for their precious help with technical drawing, Carsten Thönnißen and Hans-Peter Oepen fom the University of Hamburg for recording SEM images of the fiber tips, Bardenheuer Nadja, Hartin Tania and Krieger Ulrike for their administrative support.

Thanks to the colleagues Maria Katsiaflaka, for also being a great friend, Clemens Weninger, Alessandra Picchiotti, Nele Müller, Peter Krötz, Ling Ren, Yinfei Lu, Gourab Chatterjee, Cornelius Pieterse, Khalid Siddiqui, Badali Daniel, Stuart Hayes, Kostyantyn Pichugin, Prokhorenko Valentyn and German Sciaini. Thank you all for making the last four years so pleasant.